2014

In–vivo endorectal dosimetry of prostate high dose rate brachytherapy and TomoTherapy ® using MOSkinTM detectors

Sarah Alnaghy
University of Wollongong

In–Vivo Endorectal Dosimetry of Prostate High Dose Rate Brachytherapy and TomoTherapy® Using MO*Skin*™ Detectors

A thesis submitted in fulfilment of the
requirements for the award of the degree

Master of Science - Research

from

UNIVERSITY OF WOLLONGONG

by

Sarah Alnaghy
BAppSc (MRS) RadTher, University of Sydney, 2008
GDipSc (Physics), University of Wollongong, 2011

SCHOOL OF PHYSICS
2014

Abstract

Hypofractionated radiotherapy treatments of the prostate deliver very high doses to the target volume, whilst attempting to spare healthy surrounding tissue. This leads to an extremely high dose gradient at the anterior rectal wall. Small geometrical deviations in target localisation may lead to a high dose delivered to the rectal wall. The aim of this phantom based study was the development and testing of a system for measurement of anterior rectal wall doses during hypofractionated high dose radiotherapy treatments of HDR brachytherapy and TomoTherapy®. A Perspex replica transrectal ultrasound probe was utilised within a surrogate rectum, with clinical treatments delivered to the phantom. MO*Skin*™ detectors were attached to the probes to measure dose rates to the rectal wall in real–time. A comparison of a hollow and solid Perspex probe determined if the solid probe increased rectal wall dose by introducing extra backscatter material. For brachytherapy, similar results were produced between probes. Dual MO*Skin*™ detectors, employed to improve the accuracy of measurement over a single detector arrangement, increased agreement between measured and TPS doses, with all dual detector results demonstrating acceptable agreement (within 5%). For TomoTherapy®, the probe was utilised as a Perspex surrogate for the Rectafix®. At the anterior rectal wall using single detectors and accounting for acceptable Distance–to–Agreement measurements, 87.5% of detectors measured dose to within $\pm 5\%$ of the TPS. Dual MO*Skin*™ detectors further improved results, allowing for acceptable agreement of all detector measurements with the TPS. The dual MO*Skin*™ system, if employed clinically, could help to detect errors, such as patient shifts or incorrect set–up, in dose delivery for HDR brachytherapy and Helical TomoTherapy® for the treatment of prostate cancer.

Statement of Originality

This is to certify that the work described in this thesis is entirely my own, except where due reference is made in the text.

No work in this thesis has been submitted for a degree to any other university or institution.

Signed

Sarah Alnaghy
First of March, 2014

Acknowledgments

It would not have been possible to write this thesis without the support and help of certain people, which I would like to mention here. I would firstly like to thank my husband, Saree, for his patience and support whilst I was finishing my thesis. I greatly appreciate his insights and help whenever I needed it. I would like to thank my family too, for not only financially supporting me but for always being encouraging and having confidence in me throughout my education. To my supervisors, Dr. Dean Cutajar and Professor Peter Metcalfe, thank you for accompanying me on countless trips to the hospitals to acquire data for my thesis and for your time spent answering my questions and reading my thesis. Your guidance and supervision is much appreciated. To the staff at SGCCC and Liverpool Hospital, especially Andrew Howie, Shrikant Deshpande, Dr. Aitang Xing, Dr. Lois Holloway and Dr. Phil Vial, thank you for making the time for us to visit your facility and for assisting us with using the equipment. I would also like to thank Professor Anatoly Rozenfeld. His encouragement and support for the students of the Centre for Medical Radiation Physics (CMRP) to carry out projects like this is invaluable.

Contents

List of Figures

List of Tables

List of Abbreviations

3DCRT	Three–Dimensional Conformal Radiation Therapy
AAPM	American Association of Physicists in Medicine
ADT	Androgen Deprivation Therapy
CF	Calibration Factor
CTV	Clinical Target Volume
CMRP	Centre for Medical Radiation Physics
CT	Computed–Tomography
DRE	Digital Rectal Examination
DTA	Distance–to–Agreement
DVH	Dose–Volume Histogram
ERB	Endorectal Balloon
Fe	Iron
HDR	High Dose Rate
IMRT	Intensity–Modulated Radiation Therapy
Ir	Iridium
KV	kilovoltage
LDR	Low Dose Rate
LET	Linear Energy Transfer
LQ	Linear–Quadratic
MBDCA	Model–Based Dose Calculation Algorithms
MLC	Multileaf Collimator
MOSFET	Metal Oxide Semiconductor Field–Effect Transistor
MU	Monitor Unit

MV	Megavoltage
OAR	Organ at Risk
Os	Osmium
PDD	Percentage Depth Dose
PSA	Prostate Specific Antigen
Pt	Platinum
PTV	Planning Target Volume
RTOG	Radiation Therapy Oncology Group
SBRT	Stereotactic Body Radiation Therapy
Si	Silicon
SiO_2	Silicon Dioxide
SSD	Source–to–Surface Distance
TG-43	Task Group 43
TLD	Thermoluminescent Dosimeter
TPS	Treatment Planning System
TRUS	Transrectal Ultrasound
VMAT	Volumetric Modulated Arc Therapy
WED	Water Equivalent Depth

Conference Proceedings

Handel S, Deshpande S, Cutajar D, Metcalfe P, Rosenfeld A, *In–vivo* measurements of the rectal wall during helical TomoTherapy® using MO*Skin*™ detectors, Accepted abstract, Engineering and Physical Scientists in Medicine Conference, Perth, 2013

Alnaghy S, Deshpande S, Cutajar D, Metcalfe P, Rosenfeld A, Real time rectal wall dosimetry during helical TomoTherapy® using MO*Skin*™ detectors, Submitted abstract, Combined Scientific Meeting, Melbourne, 2014

Chapter 1

Introduction

Prostate cancer is the most common cancer type in Australian men, with one in nine men developing the disease at some stage in his lifetime [1]. More than 95% of prostate cancers arise from the epithelial cells of the prostate gland in the form of prostate adenocarcinoma [2]. The risk of prostate cancer increases with age and family history of the disease. Other risk factors include race and ethnicity, socio–economic factors, environmental exposure and diet [2].

Treatment for prostate cancer includes surgery, chemotherapy, hormone therapy, radiation therapy, or a combination of these. Radiation therapy includes options such as high or low dose rate (HDR or LDR) brachytherapy, or external beam options such 3D conformal radiation therapy (3DCRT), intensity modulated radiation therapy (IMRT), volumetric modulated arc therapy (VMAT) and Helical TomoTherapy® techniques. The types of radiation therapy to be discussed here are HDR brachytherapy and Helical TomoTherapy®. Brachytherapy involves the use of a radiation source implanted close to the treatment site in the patient, whereas TomoTherapy® is delivered helically from an external beam.

Radiation dose delivered in the form of brachytherapy has a steep dose gradient outside the target volume as the organs at risk (OARs) in the vicinity of the prostate are quite close to the treatment field, meaning errors in the set up of a patient for

treatment could be detrimental in terms of patient side effects. Various studies have aimed to improve the accuracy of brachytherapy treatments through, for example, positioning methods or dosimetric measurement [3–6]. This study aims to incorporate both these aspects into a method of brachytherapy treatment. The MO*Skin*™, a MOSFET based dosimeter, is a silicon detector with a very small sensitive volume and designed to measure doses at air/skin interfaces [3]. These detectors will be attached to a replica ultrasound probe to test whether this method is suitable for *in–vivo* dosimetry in prostate cancer treatment. This method has been tested with another type of detector, a PTW diode array type 9112, in a previous study [5].

This study then investigates the probes' potential for TomoTherapy®. The Rectafix® [7] system has previously been developed to improve positioning and immobilisation in the treatment of prostate radiation therapy, for proton boosts and hypofractionated photon treatments [8–10]. This study looks at building upon this technology. By utilising the probe as a surrogate for the Rectafix®, coupled with MO*Skin*™ detectors; the probe can not only assist in immobilisation, but can ensure the geometric conditions are the same for improved accuracy in plan delivery and dosimetric measurement in a high dose gradient region. Further accuracy was investigated by the addition of fiducial markers to the probe in one case.

1.1 Objectives and Overview of this Thesis

Using the same geometry for treatment as for the volume study with the transrectal ultrasound (TRUS) probe; and also measuring the dose in real time; this study aimed to improve the correspondence between planning and treatment doses. A replica ultrasound transducer has been developed at the Centre for Medical Radiation Physics (CMRP), University of Wollongong for use in both prostate brachytherapy and TomoTherapy®. It is capable of *in–vivo* measurements of absorbed dose to the anterior rectal wall using MO*Skin*™ detectors positioned along the anterior edge of the probe. Two probes were designed and compared: a solid Perspex probe con-

taining four detectors and a hollow Perspex probe containing four detectors. This Thesis has two dose verification studies: the HDR brachytherapy study completed at St. George Cancer Care Centre (SGCCC), St. George Hospital, Kogarah, and the TomoTherapy® study completed at Liverpool Hospital, Liverpool.

The fundamental objectives of this Thesis are as follows:

1. Design and development of replica ultrasound probes that have the ability to house MO*Skin*™ detectors.

2. Completion of preliminary measurements for both HDR brachytherapy and TomoTherapy® studies, such as detector calibration and backscatter comparison, using a CIRS Plastic Water® LR solid water phantom and CIRS IMRT Head and Torso Freepoint Phantom for brachytherapy and TomoTherapy® respectively.

3. Determine whether MO*Skin*™ detectors could measure dose to the rectum within $\pm 5\%$ of the dose calculated by the treatment planning system for HDR brachytherapy and TomoTherapy®.

4. Comparison of replica probes for HDR brachytherapy and TomoTherapy® using a gelatine phantom and IMRT Head and Torso Freepoint Phantom respectively. Comparison of a solid Perspex probe and a hollow Perspex probe to determine whether the solid probe increased dose to the rectal wall due to the added backscatter material.

Chapter 2

Literature Review

2.1 Prostate Cancer and Treatment Options

The prostate is an organ made up of glandular, fibrous, and muscular elements. It encapsulates the beginning of the urethra, and is situated inferiorly to the base of the bladder. Attached to the posterosuperior portion of the prostate gland are the seminal vesicles and vas deferens. The prostate gland consists of four zones: the central, transition, fibromuscular, and the largest; the peripheral zone [2, 11].

75% of prostate carcinomas develop in this peripheral zone, although benign prostatic hyperplasia (BPH) usually originates in the transition zone. Prostate cancer can extend not only into the other zones, but also into the seminal vesicles, rectum, and bladder neck. Metastases to the lymph nodes and other regions of the body are dependent on the size and degree of differentiation of the primary tumour [2, 11].

Tests such as the Prostate Specific Antigen (PSA) test are carried out to assist in diagnosing and staging the cancer [2, 12]. PSA is a type of protein and its presence in the bloodstream may indicate that a tumour (whether benign or malignant) has affected the membrane of the prostate gland, allowing PSA to pass into the bloodstream [13]. A PSA of >0.4 μg/L is considered a risk factor, however it may be higher due to other factors such as surgery or androgen deprivation therapy

(ADT) [2].

The staging and Gleason score are established, which determine the treatment options and outcome for the patient. Clinical staging is based on PSA, digital rectal examination (DRE) findings, and imaging, whereas pathologic staging is based on the biopsy results and the American Joint Committee on Cancer Guidelines 2007. These guidelines grade the tumour with the letters: TNM. T is the tumour extent and can range from T1–T4. N represents the lymph node involvement and can be NX (no sample available), N0 (no positive nodes) or N1 (nodal involvement). M indicates whether there is metastatic disease present by either M0 (no metastases) or M1 (metastases) [2]. The Gleason score is a numbered grading system based on the histopathology of the prostate cancer and is used as an indicator of patient outcome [14]. Gleason scores can range between 2 and 10; the higher the score, the more aggressive and metastatic the cancer [11,13].

Treatment options are decided based on the stage of the disease, although there is still no consensus on the best option to treat prostate cancer according to Simmons, Berglund and Jones (2011) [13]. For small, slow–growing tumours (i.e. T1a), observation is sometimes preferred over treatment. It is also an option for elderly patients (if life expectancy is less than 10 years) [11, 13] for whom treatment may decrease quality of life rather than improve upon it. Observation generally includes DRE and PSA testing every 6–12 months [13]. If the tumour is beyond the observation stage, treatment options include surgery, chemotherapy, hormone therapy and radiation therapy, or a combination of various treatment options. Other treatments for prostate cancer that are not yet commonly employed, or are still in the development stage, are cryotherapy, high–intensity focused ultrasound, orchiectomy, and focal ablation [13].

Radical prostatectomy is usually the treatment option used for lower stage, localised tumours, such as T1 or T2. A minimum life expectancy of 10 years is a requirement for surgery [11]. This type of surgery aims to remove the prostate

gland and seminal vesicles, as well as sometimes including the pelvic lymph nodes for intermediate– to high–risk cases [13, 15]. Side effects of radical prostatectomy include incontinence and sexual dysfunction, however, the aim is obviously to reduce or avoid these effects [15]. After radical prostatectomy, recurrence rates at 5 years are very minimal for low–risk patients, at only about 6%. Patients with positive surgical margins generally undergo external beam radiation therapy (EBRT) within 3–6 months of their surgery to kill residual tumour cells [13].

Chemotherapy is the administration of cytotoxic drugs to a patient for the systemic treatment of cancer. It can be delivered via injection (intravenous, intraarterial or intrathecal), orally or for some types of cancer, by cavity insertion. The drugs are aimed at destroying tumour cells by affecting them at a certain stage of the cell cycle [11]. Hormone therapy, or ADT, involves the treatment of prostate cancer with hormones such as leutinizing hormone–releasing hormone agonist or antagonist to reduce the production of testosterone [11, 13]. It is not used as a monotherapy for prostate cancer due to its ineffectiveness on its own, but rather as an adjuvant therapy to radical prostatectomy or radiation therapy for high–risk patients [13, 16].

Radiation therapy can be either external beam or brachytherapy; both of which are described in the following sections.

2.2 Brachytherapy

Brachytherapy to the prostate is an invasive procedure involving sources of radiation being inserted into the patient to treat the affected tissue. This type of treatment effectively spares normal tissue whilst treating the tumour due to the steep dose gradient. Prostate brachytherapy is an interstitial form of therapy. HDR brachytherapy is in the form of removable implants, which involve multiple catheters being inserted into the patient and an afterloading technique being used to send the source down each catheter. These catheters are inserted for only a

couple of, or a few days, whilst treatment is being carried out, and then they are removed [17], although most HDR insertions are for a few hours from time of implantation to the time of treatment [18]. The source travels down the catheter in 'steps', staying at each step for a predetermined dwell time [19]. This differs from LDR where the radiation sources are permanent, with a continuous treatment over the lifetime of the source. The dose rate for HDR can be up to 5 Gy/minute in tissue at a distance of 5 mm from the source [17]. LDR brachytherapy uses permanent implants (radioactive seeds) which are inserted into the tumour volume to deliver the dose over a few months. The dose rate on average is 10 cGy/hour [17, 19].

HDR uses a medium energy source but with a high activity as the dose needs to be delivered over a shorter amount of time than in LDR. LDR uses a low energy, low activity source as it is delivered over a few months. The purpose of using a low energy is to keep the dose to surrounding organs low and in the case of LDR; to keep the dose to the general public low. The patient emits a small amount of radiation until the source decays in LDR but in HDR the patient is not radioactive after the source has been removed [17]. HDR commonly utilises Iridium–192 (^{192}I), which has a half–life of 73.83 days. It decays to an excited state of Platinum (^{192}Pt) by β^-, and to an excited state of Osmium (^{192}Os) by electron capture. De–excitation occurs by the emission of gamma rays with an average energy of approximately 370 keV [20].

The α/β ratio is a parameter of the linear–quadradic (LQ) formalism when determining the survival curve of early– and late–responding tissues, and hence determining the sensitivity of these different tissue types to fractionation. Tissues that are late–responding have a low α/β ratio and have been shown to be spared more by fractionation, whilst fractionation has been shown to have a higher cell kill in early–responding tissues, such as tumours. However, prostate cancer is believed to have a low α/β ratio (between 1.5 and 3), and cell kill has been shown to increase when using larger fraction sizes for low α/β ratios [21]. The radiobiological effect is

different between LDR and HDR [21]. LDR reduces the effect on late–responding tissues and gives the normal tissue time to repair whilst damaging cells with a higher α/β ratio, which are early–responding. HDR has a greater biological effect than LDR on tissues with a lower α/β ratio [19]. The trend is toward HDR treatments as these treatments are hypofractionated and each fraction size is larger than normal fractionation regimens, which would be more beneficial for prostate cancers if they do have a low α/β ratio. However, it is still not known exactly what the α/β ratio for prostate cancer is [19, 21].

The aim of treatment planning in HDR brachytherapy, as reported by Simmons, Berglund and Jones (2011), is to cover at least 90% of the prostate with 100% of the radiation dose [13]. The dose fractionation regimen at St. George Cancer Care Centre (SGCCC), St. George Hospital in Kogarah, New South Wales, where this project took place, is as follows: HDR brachytherapy delivers 18 Gy in 2 fractions (1 fraction per day) where the patient stays at the hospital as an in–patient overnight. 4–6 fractions are also commonly used at other centres [17]. For LDR, once the seeds have been inserted (and after recovery from the procedure) the patient is free to go home. LDR is used as a monotherapy whereas HDR is used as a boost for external beam treatment, which is an added 46 Gy in 23 fractions to the overall treatment.

When treating any area of the body with radiation therapy, the OARs must be taken into account when planning a treatment to minimise each organ dose as much as possible. Dose optimisation on the computer planning program allows these organs to be avoided as much as possible [19]. However, regardless of how much the dose to these organs is minimised, there is still a chance of side effects. Side effects of prostate brachytherapy include urinary incontinence, urgency and frequency, dysuria, rectal bleeding, diarrhoea, proctitis and erectile dysfunction [2]. Late rectal toxicity resulting from irradiating the rectal wall can impact quite negatively on a patient's life [22, 23]. Measuring the dose to the anterior rectal wall allows monitoring of whether the planned dose is actually being delivered to that site.

HDR brachytherapy has been shown to produce good outcomes for the treatment of prostate adenocarcinoma. The results of a study by Brenner and colleagues in 2002 demonstrate strong evidence that α/β values for prostate tumour control are low, meaning these tumours have a high sensitivity to fractionation. This is more typical of late–responding normal tissue, and not so common in tumours [21]. Therefore, large dose fractions are ideal for treating prostate adenocarcinomas, which HDR brachytherapy delivers.

In a recent study [24], data was analysed for the period of 2003–2009, with 197 patients treated with HDR brachytherapy for prostate adenocarcinoma. Only patients with T1 to T3b tumours and a PSA of less than 40 μg/L were included in the study. 30 patients were treated with 34 Gy in 3 fractions, 25 with 36 Gy in 3 fractions, 109 patients with 31.5 Gy in 3 fractions and 33 patients were given 26 Gy in 2 fractions. No significant difference in extent and severity of either early or late rectal or urinary radiation effects were observed for the variations in dose fractionation. For the high–risk patients, 91% were free of biochemical relapse after 3 years, and 99% were free for the intermediate–risk group. At 4 years, 87% were free from relapse in the high-risk group and 95% for the intermediate–risk. HDR brachytherapy has been shown to have a lower rate of incontinence as a side effect, and is also a less expensive treatment option than radical prostatectomy [13].

At SGCCC, the eligibility criteria to receive HDR brachytherapy to the prostate includes intermediate– to high–risk prostate cancer patients with no evidence of nodal or distant metastases. High risk patients must have only one of either a PSA of $\geq$20 μg/L or a Gleason score of $\geq$8 or be stage T3a. Patients must have had no trans–urethral resection of the prostate (TURP) and have a life expectancy of 5 years or more [25]. A Nucletron HDR unit is utilised to treat patients, with planning completed on an Oncentra® Brachy Treatment Planning System.

Currently, brachytherapy TPS are based on the AAPM TG–43 formalism, which will be described in Section 2.5. This formalism is based on the superposition of single–source dose distributions in a liquid water phantom. A fixed volume is utilised for radiation scattering. Brachytherapy TPS currently do not account for heterogeneity in tissue and also in applicators, and changed scattering conditions based on organ/body contour. Hence, uncertainties lie in its limitations for patient dose calculation. New model–based dose calculation algorithms (MBDCAs) are being developed, such as those based on Monte Carlo or collapsed cone. Fortunately, for prostate treatment, prostates are surrounded by an adequate depth of tissue and hence, are not as affected by scattering conditions as are some other treatment areas. TG–186 recommended that current TG–43 practices be implemented alongside MBDCAs to assess the impact of utilising these algorithms in clinical practice [26, 27].

2.3 External Beam Radiation Therapy

EBRT is a non–invasive treatment that uses high energy x–rays (usually 6–18 MV) to deliver dose to the patient, mostly commonly with a linear accelerator. Previously, a 'four–field box' technique was used to deliver treatment to the prostate, seminal vesicles and lymph nodes, with generally 45 Gy prescribed to the whole treatment field and the prostate itself boosted to 70 Gy or more. Nowadays, 3DCRT and IMRT are the techniques usually employed. Other techniques employed are VMAT, TomoTherapy® and Stereotactic Body Radiation Therapy (SBRT). 3DCRT uses multileaf collimators (MLCs) to conform the treatment field to the prostate and other affected areas. A simulation CT scan is taken and 3D planning is utilised. IMRT utilises many beam segments to modulate the intensity of the beam within each treatment field. Inverse treatment planning is used to achieve optimisation by the user providing dose objectives and then the planning program calculates a dose distribution from these objectives. IMRT treatments generally deliver doses of 75–85 Gy over 30–36 days [13, 28]. Static and dynamic options for MLCs are

available in IMRT. Static IMRT means the leaves are stationary during dose delivery, and dynamic IMRT means the leaves are moving. Dynamic IMRT has been found to require 15–20% more monitor units (MUs) and 15% more time than static IMRT; increasing the risk of secondary malignancies from radiation exposure [29–31]. However dynamic IMRT, with its continuous MLC motion; allows the intensity that is actually delivered to resemble the optimal fluence of the plan more closely [29].

IMRT has been shown to reduce the dose to critical structures in comparison to 3DCRT, whilst being able to escalate the target dose [32–34]. Advantages of 3DCRT include that this technique requires less MUs than static IMRT, depending on the energy (3.5–4.9% times less), and hence also less than dynamic IMRT [29, 35]. In a comparison between IMRT and 3DCRT to the prostate, mean doses to the prostate were similar at 75.10 Gy and 75.40 Gy respectively, with seminal vesicle mean doses at 75.11 Gy and 75.02 Gy respectively. It was found that 3DCRT delivered significantly higher doses to the rectum, with 66% of the rectum receiving 10.18 Gy more dose, 50% receiving 6.64 Gy more and 33% receiving 3.55 Gy more dose than IMRT. The same percentage volumes of the upper rectum received even higher doses [32]. Michalski et al. (2011) reported the findings of a Phase III RTOG trial investigating the rectal toxicities of 748 patient receiving prostate 3DCRT and IMRT. The median V65, V70, and V75 of the rectum and were found to be reduced for IMRT: 27.4%, 21.7%, and 15.8% respectively for 3DCRT in comparison to 23.0%, 18.2%, and 13.0% respectively for IMRT [36].

TomoTherapy® is another option utilised to deliver EBRT. TomoTherapy® involves the use of a rotating narrow fan beam to deliver dose to the patient. Binary MLCs (i.e. either in an open or closed state operating in the superior/inferior direction of the patient) form a 1D profile that constantly changes; combining the 1D profile with beam rotation, intensity modulation in 2D is produced. The rotation becomes a helical rotation due to the movement of the couch through the bore of the gantry. However, TomoTherapy® can also deliver a treatment field with a

fixed couch position. The helical delivery method is advantageous as it does not allow any overlapping of the fields at the junctions, which can lead to overdosing or underdosing. Parameters that affect dose modulation, resolution and treatment times are collimator width, pitch (i.e. couch movement per rotation) and the modulation factor (i.e. the ratio of the maximum time a certain leaf is open to the mean time that all leaves are open) [17, 37]. TomoTherapy® also has the ability to take CT images of the patient before each treatment to verify positioning [38–41]. Other advantages of TomoTherapy® include its capability of generating very complex, highly intensity modulated dose distributions due to its greater number of degrees of freedom, and that it has the ability to treat large volumes in a single treatment delivery [42].

VMAT, another option for EBRT, is a type of IMRT that utilises modulated fields to deliver a conformal dose in one or more rotations of the gantry. The modulated field is achieved by varying dose rate, MLC aperture and orientation, and gantry speed, with the beam switched on continuously for efficient treatment delivery [43–45].

There are several disadvantages of EBRT, which include the length of treatments (i.e. daily treatments over many weeks) and the long–term side effects. These effects include frequency and urgency of urination, nocturia, hemorrhagic cystitis, rectal bleeding and pain, and of course, risk of a secondary malignancy. EBRT modalities also provide an expensive treatment option [13], due to the 'activity–based' calculation of treatment costs (from clinical assessment to follow–up), with the model primarily based on factors such as equipment/materials, buildings/facilities and staffing [46].

A study by Tsai et al. (2011) compared step–and–shoot IMRT, helical TomoTherapy® and VMAT, in terms of treatment and dosimetry for prostate cancer. Three plans for each treatment delivery method were completed for each

of twelve patients. All three plan types met the aims for target volume dosimetry and the constraints for OARs. The average maximum planning target volume (PTV) doses for all three plan types was similar, and PTV coverage was also similar, however TomoTherapy® had the best PTV conformity. The percentage volume of the rectum receiving 65 Gy and 40 Gy (i.e. the dose volume levels for the rectum [47, 48]) was 9.1% and 24.8% for TomoTherapy®, 12.4% and 30.8% for VMAT, and 14.7% and 35.5% for step-and–shoot IMRT. It can be seen that TomoTherapy® plans had better sparing of the rectum at 65 and 40 Gy [49].

The study found that the mean required MUs were 309.7 for VMAT, 336.1 for step–and–shoot IMRT, and the highest for TomoTherapy® at 3368. The advantage of lower MUs is a lesser scattered dose to the body. The treatment time required was lowest for VMAT at 2.6 minutes, with step–and–shoot IMRT and TomoTherapy® taking 3.8 minutes [49]. Less treatment time is an advantage in terms of potentially reducing intrafractional movement [50] and reducing out–of–field, scattered and leakage doses [51]. TomoTherapy® was shown to be superior in some dosimetric aspects, although it needed more MUs and time to deliver. The authors recognise that their study was limited in that it had a small patient number [49]. Aspects of TomoTherapy® contributing to the longer treatment time are the number of rotations needed and the slice thickness [51].

Helical TomoTherapy® can have treatment times longer than treatment times using a conventional linear accelerator [51]. When compared to RapidArc (Varian's implementation of VMAT), a typical prostate treatment using TomoTherapy® requires a treatment time of 4–7 minutes, whereas RapidArc can take about 1.5 minutes. Although this is for relatively simple cases only [42, 52]. However, despite the longer treatment times, the shielding is maximised in the delivery system of the TomoTherapy® machine to minimise radiation leakage [51].

A study by Ramsey et al. (2006) aimed to measure the out–of–field doses,

in–air scatter and leakage doses using TomoTherapy®. The results showed that peripheral doses were equal to or less than those found previously for IMRT treatments using conventional linear accelerators; with peripheral dose dropping to 0.4% of the prescribed dose at 20 cm. At distances of 60 cm or more from the machine's isocenter, leakage dose made up 94% of the in–air dose. Peripheral doses were lower than expected, and these lower doses were due not only to the increased shielding, but also due to the fact that there is no flattening filter in TomoTherapy® units, unlike in conventional accelerators. As well as this, the beamlets used are narrow, contributing to the reason for these lower doses [51].

The type of EBRT to be used in this study is a TomoTherapy® boost. Hypofractionation such as this may be advantageous in the treatment of prostate cancer due to the estimated low α/β ratio of prostate cancer [53]. TomoTherapy® is a type of SBRT. SBRT can deliver this hypofractionated dose with examples of prescriptions varying from 35 Gy in 7 fractions to boosts of 19 Gy in 2 fractions. SBRT has been shown to produce low rates of acute low urinary and rectal toxicity (Grade II) [53–55]. Jabbari et al. (2011) completed a study with twenty patients treated with prostate SBRT as a monotherapy, with a prescription of 9.5 Gy in 4 fractions. Another eighteen patients were given a boost with SBRT of 9.5 Gy in 2 fractions, after their treatment with EBRT and ADT. They found that 42% had acute Grade II gastrourinary and 11% of patients had acute Grade II gastrointestinal toxicity. There was no Grade III acute toxicity found, however, two patients experienced late Grade III gastrourinary toxicity [54].

In 2010, in a study by Katz et al., seventy–three patients were treated with 45 Gy EBRT along with an SBRT boost. The boost prescription varied between patient groups, and the various presciptions were: 18 Gy in 3 fractions, 19.5 Gy in 3 fractions, and 21 Gy in 3 fractions. It was found that less than 7% of patients experienced Grade II acute urinary and rectal toxicity. Only one patient experienced Grade III late toxicity [53]. Oermann et al. in 2010 published a study using

CyberKnife® to deliver a SBRT boost of 19.5 Gy in 3 fractions along with an IMRT prescription of 50.4 Gy in 28 fractions to twenty–four patients, some also being treated with ADT. 13% of patients experienced Grade II gastrourinary toxicity and 4% of patients experienced Grade II gastrointestinal toxicity, with no Grade III observed [55].

In comparison to this, HDR brachytherapy has been shown to produce acute Grade II gastrourinary toxicity rates in the range of 5.5–22.5%, and acute Grade II gastrointestinal toxicity in the range 3.9–7.0%. Grade III gastrourinary toxicity was found to be experienced by 1.8–3.9% of patients [55–59].

The TomoTherapy® Hi–Art® treatment planning system employed in this study utilises a convolution/superposition algorithm for dose calculation, based on the collapsed–cone method. Algorithms developed to save on calculation time can introduce distortions in dose distributions. This is particularly an issue in low density media for small fields, including IMRT small field superposition [60]. Superposition/convolution algorithms were found by Dogan et al. (2009) to agree with Monte Carlo calculations (the current gold standard in dose calculation algorithms) to within 2% for prostate IMRT [61]. Another study by Francescon et al. (2003) compared a collapsed–cone algorithm with Monte Carlo calculations for step–andshoot prostate IMRT and found a difference of 2.1% between the two algorithms at isocentre. More complex IMRT plans with more heterogeneous tissues, such as the head and neck region, show a larger discrepancy than for IMRT prostate plans. A 2.9% difference was found at isocentre for the head and neck plans. Larger discrepancies were observed on the dose–volume histogram (DVH); with a deviation of $<$6% for doses less than 85% of the prescribed dose, and much larger dose discrepancies for doses above the 85% due to the small segment contribution [62]. Superposition/convolution algorithms have uncertainty in prediction of fluence, as well as photon transmission through the patient and through MLCs [61].

2.4 Quality Assurance and Immobilisation for Prostate Radiation Therapy

Prostatic motion may occur between fractions (interfraction) and during fractions (intrafraction). Intrafraction motion is unpredictable and can include both sudden or slow motion [63–65]. To ensure accurate treatment delivery to the prostate, equipment for the immobiliation of the prostate and patient is utilised, with quality assurance (QA) procedures established. QA reduces errors from the planning process of a patient's treatment to the actual treatment itself, and the data gathered from QA tests enables a comparison of results between radiation oncology departments for clinical trials, to further improve treatments [17].

Problems that arise with prostate brachytherapy are movement of catheter [18], seed and prostate, and also changes in the tissue due to oedema arising from catheter insertion. Human error contributes to this. Whitaker et al. (2011) found the median catheter movement to be 7.5 mm, with the range of movement being between -2.9–23.9 mm [18]. Currently, in both HDR and LDR brachytherapy, TRUS is used for guidance of catheter/seed insertion and and C–arm fluroscopy is used to provide visualisation of the implants [66]. TRUS allows the insertion of implants through the perineum into the prostate, guided by a template according to what was planned in the case of LDR. For HDR, the plan is completed after catheter insertion and after a CT scan is completed [67].

Although TRUS visualises the soft tissue well (but is not good for visualisation of seed positions), and fluroscopy visualises the implants, they are not used real–time during treatment. Another disadvantage of fluroscopy is the extra dose given to the patient and exposure to the operators. It is also difficult to relate source positions to the prostate itself using the conventional methods of treatment planning [66,68]. Another issue is the relatively long source dwell time for acquisition of images to resolve source position, again, increasing patient dose. *In–vivo* dosimetry

with MO*Skin*™ detectors addresses these issues by allowing real–time measurement of dose to the patient without further increasing patient dose.

Endorectal balloons (ERBs) are inflated with air after rectal insertion; displacing the anterior rectal wall anteriorly. ERBs increase the distance between the prostate and the posterior rectal wall [9, 69, 70]. Hardcastle et al. (2010) employed the use of ERBs to immobilise the prostate and also move as much of the rectal volume as possible out of the high dose region [3]. Spacer gels increase the distance between the prostate and rectal wall and hence reduce rectal wall dose as they are injected into the perirectal space (between prostate and anterior rectal wall). Spacer gels are advantageous as they only require one injection to last the entire treatment [9, 71, 72]. Alternatively, an ultrasound probe replica has been trialled to replicate the geometrical conditions between simulation and treatment by Seymour et al. in 2011 [5]. A new device called the Rectafix® [7] has been introduced, as reported by two studies: Isacsson et al. (2010) and Nilsson et al. (2014) [8, 9]. A comparison has been made in Table 2.1 between ERBs, spacer gels and the Rectafix® device in terms of dose–volume reduction and set–up accuracy. It can be seen that due to the rigidity of the Rectafix®, dose–volumes of the rectum were decreased, and in comparison to the ERBs and spacer gels; it has an increased set–up accuracy.

Immobilisation Device	Methods	Results: Dose–Volume Reduction	Results: Set-up Accuracy
Rectafix®	Nilsson et al. (2014) created 10 VMAT plans for patients with and without Rectafix® device. Prescription used was 42.7 Gy in 7 fractions and dose–volume values of $V_{40.1Gy}$, $V_{38.3Gy}$, $V_{36.5Gy}$ and $V_{32.6Gy}$ were evaluated [9]. Isacsson et al. (2010) created treatment plans (both with and without Rectafix®) for 9 patients with a prescription of 20 Gy in 4 fractions for proton boost combined with 50 Gy in 25 fractions of photon beam treatment. V_{70Gy} was compared between the two cases [8].	Nilsson et al. (2014) found that rectal wall volume was reduced to 0 cm^3 for all dose–volumes except for $V_{32.6Gy}$, although this was only 0.2 cm^3 [9]. Isacsson et al. (2010) reported a 67% reduction in V_{70Gy} and an average of 5% reduction in maximum dose to rectal wall with retraction of rectal wall [8].	Mean discrepancy between retractor markers on planning CT scan and treatment images = 0.4 mm [8].

Spacer Gel	Noyes et al. (2012) utilised 20 mL of human collagen as a spacer, with an IMRT treatment plan comparison completed with and without the collagen injected. The prescription was 75.6 Gy in 42 fractions for 11 patients. A mean separation of 12.7 mm was achieved between prostate and anterior rectal wall [71]. Wilder et al. (2010) injected 9 mL of cross–linked hyaluronan gel as a spacer gel in 10 patients for HDR brachytherapy (prescription: 2.2 Gy in 4 fractions) combined with IMRT (prescription: 50.4 Gy in 28 fractions). A separation range of 8–18 mm was achieved [72].	For rectal dose above 35 Gy, Noyes et al. (2012) reported a mean reduction in anterior rectal wall dose of 50%. V_{40Gy} was reduced to 7–15% with collagen present, when compared to 20–25% with no collagen present. V_{60Gy} was reduced to be less than 1% [71]. Wilder et al. (2010) reported a V_{60Gy} of approximately 12% with gel, and 33% without gel. A V_{70Gy} of approximately 4% with gel, and 25% without gel was reported. A mean rectal dose of 73 cGy was measured with gel present, and 106 cGy with no gel present [72].	Noyes et al. (2012) reported that it was difficult to attain the correct consistency (clumping could occur) of human collagen [71]. Hyaluronic acid (naturally–occurring polysaccharide) appears to degrade within a few weeks after exposure to radiation [71, 73]. It may be more viscous and hence may not distribute as evenly as some other synthetic agents, such as polyethylene-glycol (PEG) [71]. Wilder et al. (2010) reported thickness of hyaluronan gel in the anterior–posterior direction to be 13±3 mm at beginning of treatment and 10±4 mm at the end [72].

Endorectal Balloon (ERB)	Patel et al. (2003) completed treatment plans for 5 patients with and without an ERB inserted for both a 6 field 3DCRT and 7 coplanar field IMRT treatment, both with and without inclusion of seminal vesicles. 76 Gy in 38 fractions was prescribed. V_{60Gy}, V_{65Gy} and V_{70Gy} were evaluated. Smeenk et al. (2011) completed a planning study on the use of ERB in post–prostatectomy IMRT and their affect on anorectal doses. 70 Gy in 35 fractions was delivered to 20 patients, and planning scans were completed both with and without ERB. V_{20Gy}, V_{30Gy}, V_{40Gy}, V_{50Gy}, V_{60Gy} and V_{70Gy} were reported [74].	Patel et al. (2003) reported that the average over all the conditions was that the rectal volume receiving 65 Gy or more was reduced by 39%. The IMRT plan with ERB inserted was found spare the rectal volume most effectively at of all possible conditions. Smeenk et al. (2011) found that anal wall volumes with and without ERB were not significantly different. However, rectal wall volumes were reduced by: 4% for V_{20Gy}, 8% for V_{30Gy}, 5% for V_{40Gy}, 2% for V_{50Gy} and 3% for V_{70Gy}. V_{60Gy} remained unchanged [74].	Patel et al. (2003) found mean standard deviations in ERB movement of 2.6 mm, 3.1 mm and 1.0 mm in anterior-posterior, superior-inferior and lateral directions respectively [69]. Miralbell et al. 2004 found that ERB positioning was sub-optimal in approximately one third of patients and hence recommended daily ERB positioning verification [70].

Table 2.1

: Comparison between ERBs, spacer gels and Rectafix® in terms of dose–volume reduction and set–up accuracy.

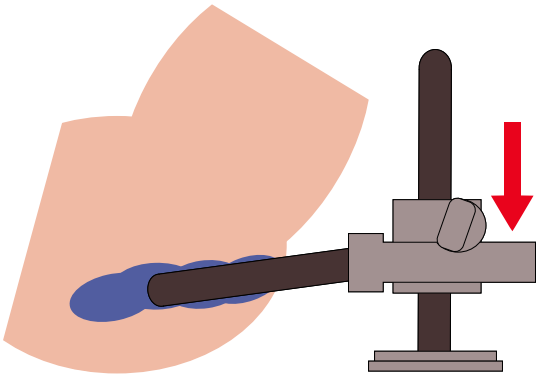

Figure 2.1 Diagram of the Rectafix® inserted into a patient, moving in the posterior direction.

In terms of immobilising a patient specifically for EBRT, equipment such as knee fix and ankle stocks are used, along with tattoos to align the patient to room lasers for reproducibile positioning [11]. Imaging devices such as on–board imaging (OBI) or cone–beam CT (CBRT) are used to produce images that are then aligned to boney anatomy, soft tissue, or fiducial markers such as gold seeds implanted in the prostate, to improve patient positioning.

The Rectafix® system is a new type of positioning equipment to be used in the treatment of prostate radiation therapy. Previously, it has been successfully used in proton therapy boosts and hypofractionated photon regimens to treat prostate cancer [8–10]. The Rectafix® consists of a rod that is inserted into the rectum and then is locked onto a vertical column for immobilisation. This column is attached to a baseplate and a leg support is also attached to this plate for further stabilisation of the patient. The shape of the rod is tilted in the posterior direction and once it is inside the rectum, it is pulled down posteriorly to move the rectum away from the prostate by approximately 20–25 mm. This reduces the dose received by the rectal wall, which reduces side effects that would normally result from rectal wall irradiation [7].

Isacsson et al. (2010) completed a study comparing the dose to the rectum in

radiation therapy treatment plans using either rectal retraction or no retraction with a Perspex rod. Both plans included a proton boost treatment of 20 Gy in 5 Gy fractions that was delivered to the prostate over four consecutive days, and then 50 Gy was delivered in 2 Gy fractions using x–rays over five days per week of the treatment period. A three–field technique was used for the x–ray treatment. The rectal retractor was 1.5 cm in diameter and its position was able to be verified on the both the planning CT scan and x–ray images (used for image guidance during treatment) by three radiopaque markers. The retractor was able to reduce interfractional motion of the rectum as well as move the rectal volume out of the treatment field. The results showed that when rectal retraction was used, dose to the rectum was significantly reduced (average dose reduction of 5%). This was achieved by the volume receiving 70 Gy in 2 Gy fractions being reduced by a range of 5–96% (average of 67%). A mean discrepancy of 0.4 mm was found between the retractor markers on the planning CT scan and images taken during treatment [8]. Nilsson et al. (2014) compared two VMAT plans for each of ten patients being treated for prostate adenocarcinoma, one with the rectum retracted using a Perspex rod and one without rectal retraction. The plans had a prescription of 42.7 Gy in 7 fractions. The results of the study by Nilsson et al. demonstrated that the plan that utilised rectal retraction reduced the dose to various volumes of the rectum, as can be seen in Table 2.1 [9].

The QA of patient positioning and prostate immobilisation has been discussed, however, QA in terms of dose verification is completed via *in–vivo* dosimetry. This will be covered in the following section.

2.5 *In–Vivo* Dosimetry

In–vivo dosimetry is a method of monitoring the actual dose delivered to the patient rather than the planned dose, and can be used as another safety precaution in treatment delivery. A dosimeter is placed on or inside the patient where the dose

measurement is needed [75]. According to the ICRU report 24 (1976), an ultimate check of the actual delivered dose can only be performed through *in–vivo* dosimetry [6,76,77]. The main examples of dosimeters used *in–vivo* are thermoluminescent dosimeters (TLDs), silicon diodes, radiochromic film, MOSFETs and scintillation detectors [75, 78, 79]. *In–vivo* dosimetry for external beam radiation therapy takes into account the various sensitivity factors that affect a dose reading, as well as calibration factors being calculated [80]. Dependence of the detector on energy, angle, temperature, dose rate, field size and SSD are taken into account [3, 75, 81].

To perform *in–vivo* dosimetry measurements in brachytherapy, a number of factors have to be known and taken into account such as air kerma strength or dose rate factors. Task Group 43 (TG–43) of the American Association of Physicists in Medicine (AAPM) put forward a formalism, which allows these factors to be accounted for in dose calculation. The formalism uses measured data of dose distributions to allow dose to be approximately calculated around an interstitial source in two dimensions in a water-equivalent medium [20, 82].

The general formalism for the 2D case is described by:

$$\dot{D}(r,\theta) = S_K \Lambda \frac{G_L(r,\theta)}{G_L(r_0,\theta_0)} g_L(r) F(r,\theta) \tag{2.1}$$

where

- r (cm) is the distance between the source centre and a point–of–interest
- θ ($^\circ$) is the angle between r and the longitudinal axis of the source
- $\dot{D}(r,\theta)$ (cGy/h) is the dose rate calculated at the point–of–interest
- S_K is the air kerma strength and is measured in U (where 1 U = 1 μGym^{2}h^{-1})
- Λ (cGyh^{-1}U^{-1}) is the dose rate constant

- $G_L(r, \theta)$ is the geometry factor
- $g_L(r)$ is the radial dose function
- $F(r, \theta)$ is defined as the anisotropy function
- r_0 and θ_0 refer to the reference point (where r_0 is the reference distance of 1 cm and θ_0 is the polar angle between the line extending to the point–of–interest and the line along the longitudinal axis of the source)
- The subscript, L, implies a line source was used for the geometry function [20, 82].

2.6 Semiconductor Physics

This project utilises a type of semiconductor detector. Silicon (Si) semiconductors can be either n– or p–type. N–type Si semiconductors are doped with impurities of a donor element. The donor contains a free electron as it is a pentavalent element, and hence its majority carriers are electrons and minority carriers are positive charges (or 'holes'). P–type Si semiconductors are instead doped with a trivalent element meaning it accepts an electron. It therefore has the opposite majority and minority carriers to n-type semiconductors [75].

When an n– and p– type semiconductor join, a p–n junction is created. By applying a reverse bias across the junction, a depletion layer with a thickness ranging from approximately 10 μm to 5 mm is formed by the majority carriers diffusing across this junction to the opposite side. A potential is then created, resulting in an electric field [75, 83].

When ionising radiation is introduced, electron–hole pairs are created and these carriers can then diffuse across the depletion layer and the charges can be collected and measured. The charges collected are proportional to the deposited

energy from the ionisations. This is linear energy transfer (LET)–independent for lighter particles such as the electron, which is the particle considered in the energy ranges of concern for this project. Indirect recombination can be used to determine the charges that are actually the result of the ionising radiation, and which charges are from the leakage current from any offset voltage of the electrometer [75, 83].

As reported by Rosenfeld (2005), semiconductor detectors have a much higher sensitivity than ionisation chambers of the same energy used and they have good mechanical rigidity and energy resolution. However, a few problems arise in their use. Long–term irradiation effects include the reducing of the diffusion length of the carriers and hence the sensitivity of the detector is reduced. A change in temperature can affect the recombination of electrons and holes and the diode response [83, 84].

2.7 Types of Radiation Detectors

Types of radiation detectors used in dosimetry are diode, diamond and MOSFET detectors, TLDs, fibre optic dosimeters, ionisation chambers and radiochromic film. Lambert et al. (2007) compared four different detectors for their dependence on depth dose, angle and temperature for use in *in–vivo* dosimetry in HDR brachytherapy [85]. The MOSFET detector, TLD, diamond detector and BrachyFOD detector (fibre optic dosimeter) were compared. Temperature dependence was found to be less than 3% for the MOSFET, diamond detector and BrachyFOD. However, the temperature dependence for the TLD could not be tested as TLDs cannot be read out in real time. The TLD showed potentially large errors in measurement (approximately 4%) and its use is limited in *in–vivo* brachytherapy due to this reason. The sensitivity response of the LiF chips of the TLDs have a depth dose dependence, causing a 33% variation in response over an increasing distance from the source when compared to the dose calculated by the treatment planning system (TPS). The angular response was not reported due to the ability for a spherically symmetric TLD to be made [85]. According to Rosenfeld (2002), the over layer of

a TLD is too thick to be able to obtain measurements at a depth suitable for dose measurement of the rectal wall in prostate brachytherapy [86].

The diamond detector is prevented from being a good method of measurement for *in–vivo* brachytherapy because it is large and rigid, which is unfortunate as it is closer to tissue equivalence than other semiconductor detectors [84,85]. Lambert et al. reported that this detector also varied only 3% from the calculated TPS doses, despite its decrease in sensitivity with increased dose rate. Its angular response varied by only 3% over the range -150° to 90° at a 50 mm source–to–detector distance. They found that the BrachyFOD was the most accurate of all four detectors with the most desirable characteristics for *in–vivo* measurement in brachytherapy. It also only varied by 3% from the predicted TPS doses up to 100 mm, beyond which the TPS data do not match Monte Carlo data so it is not recommended to use TPS data after this point. Its angular dependence was less than 2% [85].

The MOSFET detector was also found to be good for *in–vivo* measurements as it has a small size and real–time measurement capability. Its disadvantages included low sensitivity and angular dependence (varied by 10%). This study found that for distances greater than 50 mm from the source, readings of the MOSFET were affected by statistical uncertainty of 30–40% larger than the theoretical values. At distances of more than 100 mm from the source, MOSFETs were found not to be sensitive enough to provide any reading [85]. However for measurements of absorbed dose to the rectum in prostate brachytherapy, the distances important for measurement are within 50 mm so this disadvantage should not be an issue in this case.

Diode detectors allow for real–time readout, are mechanically rugged, and have small sensitive volumes, high sensitivity and high spatial resolution [75, 87]. A disadvantage is their energy dependence at low energies, which was investigated by Saini and Zhu (2007) for several commercially available diode detectors, and found

to be dependent on the type and geometry of the buildup material of the diode [87].

A similar study to that being carried out here was done by Seymour et al. in 2011, using a PTW diode array type 9112 inside a geometric replica ultrasound probe. This study aimed to provide a method of reproducing the position of the detector between simulation and actual treatment to reduce uncertainty arising from differences in detector position. Four out of the five diodes showed variations in measurement with increased distance from the source with the average discrepancy between measured and TPS calculated doses being $-0.14\% \pm 3.2\%$. However, trends were unclear. Radial dose dependence varied by an average of $\pm 3\%$ but varied in the longitudinal direction by -3% to +11%. Angular dependence was thought to be due in part to the slight rotation (both radial and longitudinal) of the diodes compared to each other. The variation of response with temperature was 0.2% over the range 23–35° [5].

For the patient measurements in the Seymour et al. study, the deviation between the measured dose and that predicted by the TPS were compared. Deviations were found to range from -42% to $+35\%$ and 71.1% of measurements had less than a 10% deviation from the TPS. The diode that was placed in a plane almost perpendicular to the central region of the prostate showed the highest agreement (86.8%) to within 10% of the TPS data, and also received the highest signal out of all five diodes. 95.8% of measurements agreed within 20% of the TPS doses. Part of the difference was attributed to positional uncertainty, which for ± 0.5 mm is 10% at 10 mm from the source. This uncertainty decreases with distance due to the inverse square law. If the probe is to be used by departments on a regular basis, this study identified that adequate pain relief for probe insertion needs to be administered, which they found was not always available [5].

Radiochromic film is used as a radiation detector by changing colour after exposure to ionising radiation. This occurs when the photo monomer molecules

in the film, which are colourless, undergo a chemical change due to the energy transfer from the incoming photons/particles. This colour change is what is measured to determine optical density, which is ultimately proportional to the dose deposited [78]. EBT film was utilised *in–vivo* by Hardcastle et al. (2009) to measure the rectal wall dose and hence verify the uncertainty of various TPSs. The film was wrapped around an ERB in a spiral geometry to be inserted into a phantom rectal cavity [88]. Film is commonly used for surface measurements, for example, for patients receiving radiation therapy to the breast, which is associated with acute and late skin toxicity [89–91].

Whilst ionisation chambers are not good for dosimetry at air/skin interfaces like the rectal wall, they are used for reference measurements. An ionisation chamber consists of two electrodes (the central collecting electrode and the conductive outer wall) separated by a gas–filled cavity. Leakage current is reduced by an insulator between the two electrodes, as well as the presence of a guard electrode, which directs the leakage current to ground so it is not collected by the collecting electrode. Ionisation chambers can be directly read out and do not have much variation in sensitivity over their lifetime [92]. In a previous study by Hardcastle et al. (2010), dual MOSFETs were normalised to ionisation chamber measurements using a 6 MV photon beam and the detectors were placed at the centre of an IMRT phantom. The dual MOSFETs were found to agree within 2.5% of the dose measured by the ionisation chambers over a range of beam angles [3].

2.8 MOSFET Detectors

MOSFET detectors are based on field effect transistors, which are made up of source, gate and drain terminals, that are then connected to the silicon dioxide (SiO_2) layer (gate terminal) and silicon (Si) substrate. For an n–type MOSFET (most available MOSFET detectors), shown in Figure 2.2, the source and drain are of n–type material, with the Si being the opposite (i.e. p–type) [93]. A physical characteristic of the

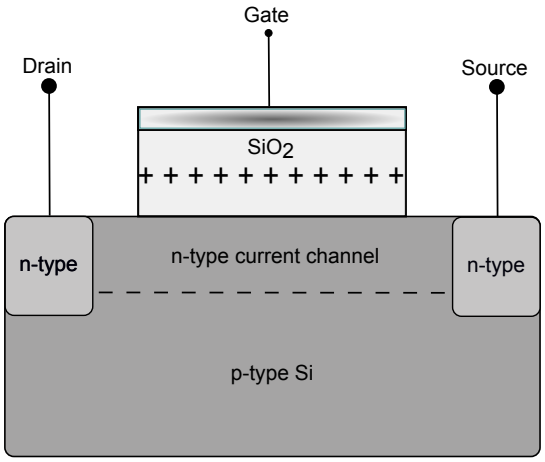

Figure 2.2 n-MOSFET detector schematic

MOSFET detector is the epoxy 'bubble', usually of about 1 mm thickness, which is used to protect the electronics from external effects. Another reason for the use of the epoxy bubble is to provide a water equivalent depth (WED) for the detector: for example, an epoxy thickness of 1 mm would give a WED of around 1.8 mm at an energy of 6 MV [84, 94].

MOSFET detectors are suitable for *in–vivo* dosimetry due to their small size and portability for easy placement. Their ability for instant readout allows the dose delivered to the patient to be monitored, and as well as this, the signal is permanently stored [6, 81].

When ionising radiation strikes the gate oxide of the MOSFET, electron–hole pairs are created and the holes that do not undergo recombination then move towards the interface between the SiO_2 and the p–type Si substrate. A positive build–up charge is created when some of these holes are trapped near the interface (Figure 2.2). At a critical gate bias, known as the threshold voltage, an inversion layer (inversion of conductivity between drain and source) is formed, allowing a fixed current to flow in the n–type channel between the drain and source. This threshold voltage shift is proportional to absorbed dose in the gate oxide [81, 86, 93].

MOSFETs can undergo irradiation in either active or passive mode, which means with or without a positive gate bias voltage respectively. Active mode is employed to increase the sensitivity and linearity of the MOSFET's response by reducing recombination of the electron–hole pairs, hence more holes are trapped, hence a larger difference in threshold voltage [81, 86].

Other desirable characteristics of the MOSFET detector that have been reported are its tissue equivalence at higher energies, negligible attenuation of radiation, low power requirement and the fact that it can be used without attachment to cables if needed [6, 81, 84]. It is also waterproof, which is important in *in–vivo* dosimetry, and does not need to undergo procedures such as annealing, unlike thermoluminscent dosimeters (TLDs) [95]. The MOSFET's good spatial resolution makes it ideal for use in high dose gradient regions [86]. This detector is also relatively inexpensive [84].

Less desirable characteristics of the MOSFET include energy dependence, due to an over–response at low energies caused by the Z number dependence of the photoelectric effect and also recombination of electron–hole pairs [95,96], especially for less than 300 keV photons with the peak value occuring at about 40 keV [96]. However, an under–response may also be observed at lower energies due to absorption by detector casing [95]. The user should be aware that a voltage shift may also be caused by a shift in temperature of up to 4–5 mV/$^{\circ}$C. This can be corrected for by the use of a dual MOSFET, where each MOSFET operates at a different gate voltage and the difference between these voltage shifts between MOSFETs is proportional to absorbed dose. This difference is temperature independent [81].

MOSFETs have previously been used to measure rectal dose in *in–vivo* dosimetry for HDR brachytherapy, and one study by Haughey, Coalter and Mugabe in 2011 aimed to evaluate whether linear array MOSFET detectors were suitable for measurement of rectal dose during HDR brachytherapy treatments. Their study included twenty

two prostate needle implant patients, with two fractions each, and four gynaecology patients with seven fractions altogether. A MOSFET array was inserted into the rectum inside a flatus tube. MOSFETs contain an epoxy 'bubble', with MOSFET arrays having a smaller epoxy bubble per detector than single detectors. The authors also faced the bubble away from source where it was possible to do so [6].

Measurements were compared to a TPS calculation using a 10 Ci source. In particular, the angular dependence had a large effect on the detector response, with results showing differences of up to 30%, especially in the polar plane. The authors discuss the difficulty in taking angular dependence into account in HDR brachytherapy due to the multiple stopping positions of the source. The larger epoxy bubble of the single MOSFET seemed to cause a greater angular dependence on that side. In total, 33% of measured readings for the prostate case agreed to within $\pm$10% of the calculated point dose from the TPS. However, if extending the radius of the TPS dose to within 5 mm of the MOSFET position, there was an agreement of 75%. The gynaecological case had an agreement of 42% to within $\pm$10% between the measured results and calculated point dose from the TPS. A variability of dose measurements of the TPS between observers of 8.5% was seen. The authors conclude that MOSFETs are not suitable for *in–vivo* dosimetry of the rectum in HDR brachytherapy due to their angular dependence and also the fact that their exact position is not known during treatment [6].

The main reason as to why MOSFETs were found to be unsuitable for rectal *in–vivo* dosimetry was the epoxy bubble, which increases the effective depth of measurement. To allow for measurements of radiation dose to the rectal mucosa, the MO*Skin*$^{\text{TM}}$ detector is a more appropriate choice. This detector was designed to measure at a depth relevant for surface dosimetry, hence the build–up layer of the detector has an effective depth of about 70 μm [97], which will be discussed in the next section. The detectors in this study faced the rectal wall, so the very thin build–up layer allowed measurements of only 70 μm out from the rectal wall;

making the MO*Skin*™ an ideal interface detector.

A study by Cheung, Butson and Yu (2009) utilised a type of MOSFET that had been redesigned by the University of Wollongong and included the use of the Clinical Semiconductor Dosimetry System (CSDS) MOSFET dosimetry system. The MOSFET was a dual k type RADFET on an epoxy bubble surrounding (that was more tissue equivalent than the MOSFET chip), and was known as the 'CSDS MOSFET'. This study aimed to investigate the effect of energy dependence of the MOSFET for 50 kVp to 10 MVp x-rays by analysing five detectors that were at different stages of their lifetime. It also looked at the effect of sensitivity dependence of the MOSFET at the energies of 100 kVp, 250 kVp and 6 MVp and at different stages of detector lifetime by measuring the change in threshold voltage [98].

The results showed that the radiation dose history of the MOSFET did not have a significant effect on the energy dependence. They did however show a difference in sensitivity with energy, with the peak sensitivity occurring at 75 kVp (over response of 3.2 times), decreasing on either side of this. This over response is less than that of other semiconductor detectors such as the T&N (Thomson and Nielsen) MOSFET (4.3 at 31 keV) and silicon diodes (6.43 at 49 keV). MOSFETs have been shown to exhibit decreased sensitivity as the dose increases because of a build–up of holes at the Si–SiO_2 interface due to the changes in the effective electric field. From these results, correction factors could be determined and once applied; an approximate linear response for sensitivity was observed for these doses. The authors recommend that sensitivity corrections should be applied to MOSFET readings, especially for readings at lower energies, and corrections should be monitored over the lifetime of the detector to ensure they are still appropriate [98].

Gopiraj, Billimagga and Ramasubramanian (2008) completed a study to observe the performance characteristics of two different MOSFET detectors: the low sensitivity TN502RD and high sensitivity TN1002RD MOSFET, using external

beam radiation therapy. These detectors were evaluated for Co–60, 6 MV and 15 MV photon EBRT in terms of entrance/exit dose measurements in *in–vivo* dosimetry. The characteristics of reproducibility, constancy (short and long term), linearity, angular dependence, energy dependence, source–to–surface distance (SSD) dependence and field size dependence were measured. The results demonstrated very good reproducibility of both detectors and acceptable constancy, both short and long term. Angular dependence was found to vary by approximately 5% for the range 315° to 45° at a source–to–axis distance (SAD) of 100 cm, with MOSFETs placed at the centre of a cylindrical phantom. For an energy of 15 MV, there was a lower energy response than for the lower energies. There was a dependence on SSD over the range 80 to 120 cm and a field size dependence was also shown for field sizes 3 $\times$ 3 cm^2 to 30 $\times$ 30 ^{2} [81].

As mentioned previously, another study that measured the angular response was that by Lambert et al. (2007). The study found that the angular response of the MOSFET detector varied by 10% for angles in the range $-150°$ to 90° at a source–to–detector distance of 50 mm. An ^{192}I source was used in the measurements. They concluded that this may be due not only to the nonuniform epoxy bubble, but also partly due to the positional error of $\pm$0.5 mm in detector placement, which can change the dose rate by 2% [85].

MOSFET detectors have also been used in LDR prostate brachytherapy to monitor the dose in several locations following seed implantation. Cygler et al. (2006) used dual micro–MOSFETs to measure the dose rate immediately after seed implantation. The dose was measured inside the bladder and along the urethra. The angular dependence of the detector was determined using a beam with an energy of 100 kVp beam, due to the effective energy being similar to that of an ^{125}I source [95].

The MOSFETs in the study of Cygler et al. were found to be suitable for *in–vivo* dosimetry in LDR prostate brachytherapy. The angular response was measured

and an almost isotropic response was observed for all detectors, with the largest deviation being approximately 2.5% after normalisation to 0°. Variations of 10% in calibration of the detectors demonstrated that individual calibration factors are needed for each detector. To ensure the signal was high enough for the *in–vivo* measurements; the detector was left at each position for ten minutes. In LDR, it is not possible to reduce the dose to the urethra after the seeds have been implanted, however, *in–vivo* dosimetry allows the possibility of monitoring the patient for increased risk of complications from increased urethral dose. Under–dosing of the base/apex of the prostate can also be monitored with the detectors and rectified by the implantation of more seeds [95].

2.9 MO*Skin*™ Detectors

MOSFETs designed specifically for skin dosimetry, known as MO*Skin*™ detectors, are used in both external beam radiation therapy and brachytherapy for measurement of radiation dose. MO*Skin*™ detectors were originally developed by the Centre for Medical Radiation Physics (CMRP) [99] to measure the dose at air/skin interfaces for EBRT [100]. MO*Skin*™ detectors have a reproducible WED of 70 μm, which allows for measurements at this depth [3], consistent with ICRU recommendations for skin dosimetry [101–103]. This is the depth that corresponds to the basal layer, which is the first radiosensitive layer of the epidermis [97, 104, 105]. To achieve this depth measurement, a thin kapton film overlays the gate, which acts as a build–up layer. The film also protects electronics from damage from, for example, moisture [97]. As mentioned previously, for this study the detectors faced the rectal wall, allowing dose measurements at a point 70 μm from the rectal wall. A schematic of the MO*Skin*™ is illustrated in Figure 2.3.

The MO*Skin*™ detector has many advantages for clinical *in–vivo* dosimetry. It has a very small sensitive volume compared to other detectors, with its gate oxide thickness measuring 0.55 μm [97]. This allows for point dose measurements

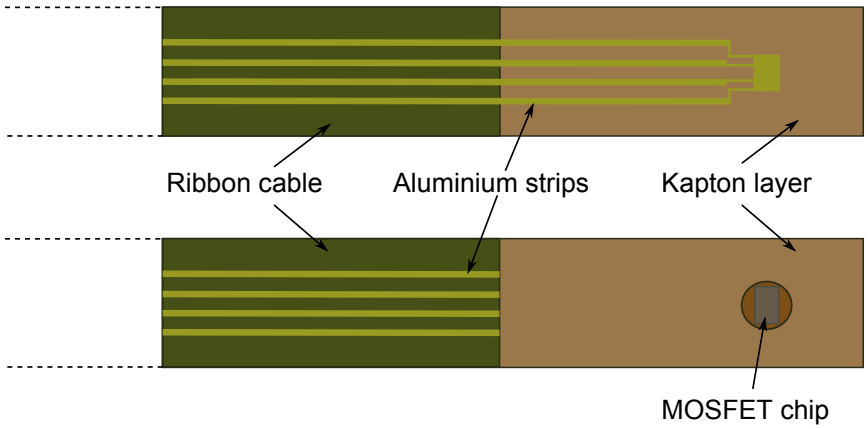

Figure 2.3 MO*Skin*™ schematic: View from above and below

in areas of high dose gradient [3], which is ideal for HDR brachytherapy and TomoTherapy®. The whole MO*Skin*™ detector is 3 mm wide, 0.4 mm thick and, with the cable, 330 mm long [104], making it easier to place for *in–vivo* dosimetry, for example, in cavities. The MO*Skin*™ is dose rate independent and also has a sensitivity that is not affected by changing temperature in the ranges: $-60\,^{\circ}\mathrm{C}$ to $+60\,^{\circ}\mathrm{C}$ for n–MOSFETs and $20\,^{\circ}\mathrm{C}$ to $37\,^{\circ}\mathrm{C}$ for dual p–MOSFETs [86], which is important for detector placement on/inside a patient. This detector can permanently store accumulated dose and be read out without loss of dose information [86]. It is available in either single or dual sensor designs [97].

Damage throughout the rectal wall is the primary cause of late radiation damage. However, measurement of the dose received by the submucosa is not possible, as this would mean implanting a dosimeter within the wall itself. Instead, dose to the anterior rectal wall can be measured, for which the MO*Skin*™ detector is ideal [97]. Another advantage of this detector is that the sensitivity can be altered by setting the reader to apply either a 5 or 15 V bias voltage to the gate. This enables the detector to measure over a larger range of doses [86, 97]. Disadvantages, or characteristics that need to be taken into account are angular dependence, energy dependence, and whether the detector has long term stability. MO*Skin*™ detectors have been shown to have a decreased response with total accumulated dose [104]. Voltage creep-up

should also be taken into account by waiting a short amount of time ($\sim$1 minute) post–irradiation to record the readout [97].

In 2008, Kwan et al. completed a study examining the differences between the PLATO TPS calculated dose and the dose measured in a solid water phantom using the MO*Skin*™ detector and the RadFET, manufactured by REM Oxford, UK. For a 'full' (i.e. water–equivalent) rectum, the results were $-3.1\pm2\%$ discrepancy for MO*Skin*™ and $-9.1\pm2\%$ discrepancy for RadFET from the TPS. For an 'empty' (i.e. air–filled) rectum the discrepancies from the TPS were: $-18.1\pm2\%$ for MO*Skin*™ and $-21.2\pm2\%$ for RadFET [4].

The results for the full rectum should have ideally been the same as the TPS. For the large difference in results between empty rectum and TPS, it was concluded that the TPS most likely overestimated the dose as it assumed the rectum was of infinite size and also water–filled; when patients are effectively treated with an empty rectum. 10–15% less dose was measured in an empty rectum compared to when full. A smaller dose was measured by the RadFET compared with the MO*Skin*™, which may be due to the 1 mm difference in source–to–detector distance due to the epoxy 'bubble' protecting the sensor in the RadFET. It was ruled out that this difference was due to a defective detector by calculating the dose 1 mm further from the source and finding that it was similar to that measured by the RadFET. Hence it was concluded that the RadFET would be unsuitable for dosimetry of the rectal wall in HDR brachytherapy [4].

Kwan et al. (2009) again successfully used the MO*Skin*™ detector to determine the difference in dose to the rectal wall between the conditions that the rectum was either empty or full. However this time, Geant4 Monte Carlo simulations were also carried out and the results compared to the experimental data. Measurements were completed at source–to–detector distances varying from 14–54 mm. The results were compared to those measured by a RadFET. The RadFET's 1 mm thick

epoxy bubble was accounted for during detector placement. By comparing the dose measurements from an empty and full rectum, the effect of backscatter on the rectal wall could be observed [97].

The results of this study were in agreement with values calculated by the TG–43 formalism and the discrepancy demonstrated an increase with larger source–to–detector distance. This was thought to be due to the detectors receiving low dose at this depth and the low response of the detectors to this dose. Other reasons given were the increased uncertainty with depth and incomplete scatter conditions provided by water–equivalent phantom. The Geant4 results showed less than a 2% variation even at 50 mm source–to–detector distance. The results of this study for absorbed dose to the anterior rectal wall in an empty rectal cavity showed a $-14.7\pm0.2\%$ discrepancy for MO*Skin*™ detectors and a $-13.7\pm0.6\%$ discrepancy for RadFET detectors from the dose measured in a homogeneous rectal phantom. Results from Geant4 also showed a similar difference to the experimental results of $13.2\pm0.6\%$ less dose in the empty rectum case compared to the full rectum case [97].

These results introduce the problem that detector measurements cannot be compared straight to TPS calculations due to the large discrepancies. The TPS assumes that the rectum is homogeneous and water–equivalent and hence the dose is overestimated, as in reality there is not as much backscatter from an air–filled rectum [97]. The effect of rectal heterogeneity on measured dose was found to be significant by Kwan et al. This project will reduce the effect of rectal heterogeneity as the ultrasound probe replica will keep the rectum at the same shape and consistency.

MO*Skin*™ detectors can be used in external beam therapy as well. In one particular study by Hardcastle et al. (2010), they were used *in–vivo* inside rectal balloons to measure the real–time dose to the anterior rectal wall in prostate radiation therapy [3]. The measured doses were compared to the theoretical doses of both the 3DCRT and intensity–modulated radiation therapy (IMRT) plans and found to be

lower than these calculated doses [3].

The study by Hardcastle et al. also demonstrates the use of the 'dual MOSFET', otherwise known as the face–to–face arrangement, which allows for angular–independent measurements. For fraction sizes of 2–10 Gy, the detectors demonstrated a reproducible sensitivity to within 1%, explained by the fact that there is not much radiation damage to the detector at these doses. For the 3DCRT plan, the measured dose was found to be 2.6% lower than the TPS dose. The IMRT plan showed a 3.2% discrepancy between measured and planned doses [3]. These differences are much less than the brachytherapy studies by Kwan et al. most likely due to the fact that brachytherapy has a much steeper dose gradient, making positional errors much more of a problem.

One issue with using MO*Skin*™ detectors that was raised by Hardcastle et al. (2010) is the error in positional reproducibility of the actual detectors during each fraction. To get accurate results, the detector should be in the exact same position as in the simulation CT scan so that the dose measurements are of the same area for each fraction. This proved difficult in the Hardcastle et al. study as the rectal balloon that contained the MO*Skin*™ detectors had the ability to move and rotate. The authors also suggest the use of multiple detectors along the superior–inferior axis of the balloon to increase the probability of actually getting a measurement of the highest dose along the anterior wall of the rectum [3]. This project uses multiple MO*Skin*™ detectors along the superior–inferior axis of the probe.

2.10 Discussion

The various treatment options for prostate cancer, such brachytherapy and EBRT, have been discussed in this chapter, as well as the QA component of radiation therapy planning and treatment. *In–vivo* dosimetry using specifically the MOSFET and MO*Skin*™ detectors was discussed, in particular the characteristics that make these

detectors ideal for *in–vivo* dosimetry. From this chapter, it can be concluded that there is still a need for improvement in dose verification in radiation therapy to the prostate for both brachytherapy and EBRT.

Chapter 3

Comparison of HDR Brachytherapy TPS Calculated Dose with MO*Skin*™ Detectors Placed in Phantom on Solid Endorectal Carrier

3.1 Probe Design and Construction

The aim of this project was to determine if MO*Skin*™ detectors could be arranged on a replica ultrasound transducer inserted into the rectum to provide real–time absorbed dose measurements during brachytherapy treatment to the prostate. It was hypothesised that MO*Skin*™ detectors could be utilised to indicate dose to the anterior rectal wall to within $\pm 5\%$ due to the fact that in clinical use, there is normally a large percentage of dose points that fall outside of a 3% tolerance [106]. The effect on backscatter conditions of using a solid Perspex probe versus a hollow probe with multiple MO*Skin*™ detectors attached was investigated. The probes were made with the dimensions of a BK Medical 8848 Ultrasound Transducer, which is the transducer used to guide catheter insertion in a prostate brachytherapy procedure at SGCCC, where this project was carried out.

The experiments were designed to benchmark detector accuracy. The clinical

implementation for HDR brachytherapy would involve a project whereby after the catheters would be inserted into the patient, the ultrasound probe would be removed and the replica probe inserted in its place. The patient would then have a CT scan with the replica probe inserted. Since the treatment plan is completed on this CT dataset, the plan also included the probe. Hence, the replica probes were made to create the same geometric conditions during treatment, as on the plan. The detectors were added to the probe to provide a method of monitoring the dose during treatment.

The MO*Skin*™ detectors were developed by CMRP, as previously mentioned. They were 'immediately' read out after irradiation using a clinical MOSFET semiconductor dosimetry system, which was also developed by CMRP. This device can measure the threshold voltages of up to five detectors simultaneously. A thirty second time interval was invoked between irradiation and read–out to allow the slight voltage increase, or 'voltage creep–up' [97], to plateau. This waiting period allowed the recombination of any charges that were not actually trapped.

Two probes were designed and made for this project, each being a replica of the ultrasound transducer. These probes were a solid Perspex probe and a hollow Perspex probe with inserts to position four MO*Skin*™ detectors. Each probe was 20 mm in diameter and 200 mm in length. The solid probe simulates a full rectum; the hollow probes an empty rectum.

Originally a probe was constructed that held one detector with a channel along the anterior side for the ribbon cable to sit in. This was the first attempt to contruct a probe that could house a MO*Skin*™ detector before trying to accommodate mutliple detectors, as the design would be more difficult. When designing the four–detector probe, it was not possible to create channels for the ribbon cables. The detectors needed to be positioned at an angle (shown in Figure 3.2) so that the cables would not overlap the sensitive volumes. This meant that the cables had to wind around the probe, and there was no equipment available that could make channels at this

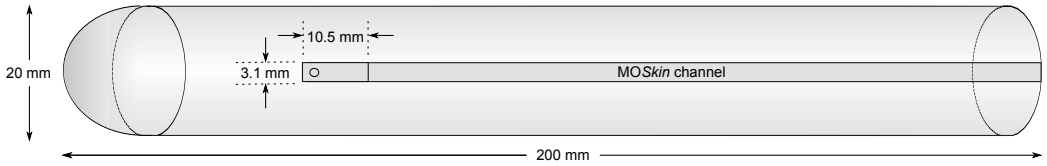

Figure 3.1 Probe 1: Solid Perspex probe with indentation to hold one MO*Skin*™ detector, including cable channel.

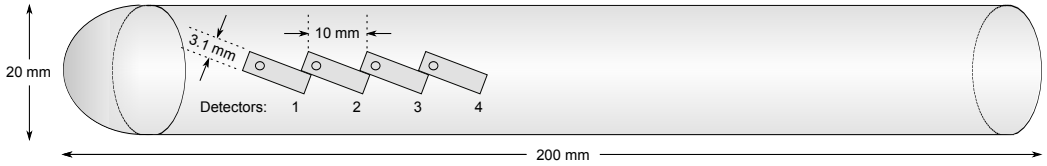

Figure 3.2 Probe 2 and 3: Solid or hollow Perspex probe with indentations to hold four MO*Skin*™ detectors.

angle at the sub–millimeter depth that was required. It was decided that since the probe (and hence the cables) needed to be covered by a condom, it would not matter if the cables could not sit into the probe's surface. Instead, they were taped down to ensure their edges would not cause any abrasion to the patient. The condom was also used to comply with Australian standards for infection control. It can be seen in Figure 3.2 that the detector positions will be referred to as 1, 2, 3 and 4, with 1 being placed most superior out of all detectors and 4 being the most inferior.

3.2 Comparison of Backscatter Differences in Solid Water with Air Cavity and No Air Cavity

The aim of this experiment was to compare the absorbed dose to the anterior rectal wall when there was an air cavity present in solid water and when there was no air cavity, to determine whether there was a difference in backscatter conditions. The

solid water used was CIRS Plastic Water® LR.

3.2.1 MO*Skin*™ Detector Calibration

MO*Skin*™ detectors were calibrated with a 10 Ci ^{192}Ir HDR brachytherapy source in solid water. The threshold voltage was measured at different source–to–detector distances from 10.0 $\pm$ 0.5 mm to 43.0 $\pm$ 0.5 mm and the time recorded to determine voltage/time values. These were compared to dose rates (cGy/hr) that were calculated using the TG–43 formalism. The source strength was taken as 40300 U (where U = cGy.cm^2/hr) for ^{192}Ir with a 0.2 mm Iron (Fe) casing [20]. The average calibration factor was determined to be 2.45 $\pm$ 0.02 mV/cGy. However, if uncertainty in source–to–detector distance is accounted for (i.e. $\pm$0.5 mm); then the uncertainty in calibration factor increases. A larger uncertainty would exist for the shorter source–to–detector distances, especially in the higher dose gradient region.

3.2.2 Percentage Depth Dose Comparison for Air Cavity and No Air Cavity

3.2.2.1 Methodology

Percentage depth dose (PDD) measurements were taken in solid water with the three different conditions of: no air cavity, cylindrical air cavity (21 mm diameter $\times$ 90 mm^3) and cuboid air cavity (20 $\times$ 20 $\times$ 90 mm^3). The two different cavities were utilised to determine if a difference in shape caused a difference in scattering conditions and hence a difference in absorbed dose. The source–to–detector distance was increased from 10 mm to 43 mm, which were arbitrarily chosen. Three voltage readings were aquired over a period of time (V/s) at each of these distances and converted to dose using the calibration factors already determined. The average absorbed dose at each distance was found. The uncertainty was determined by using Student's t–test, which can be used for very small sample sizes (i.e. three measurements) [107] and has been used previously in a rectal dosimetry study using MO*Skin*™ detectors [108]. All results were normalised the to 'no cavity' results.

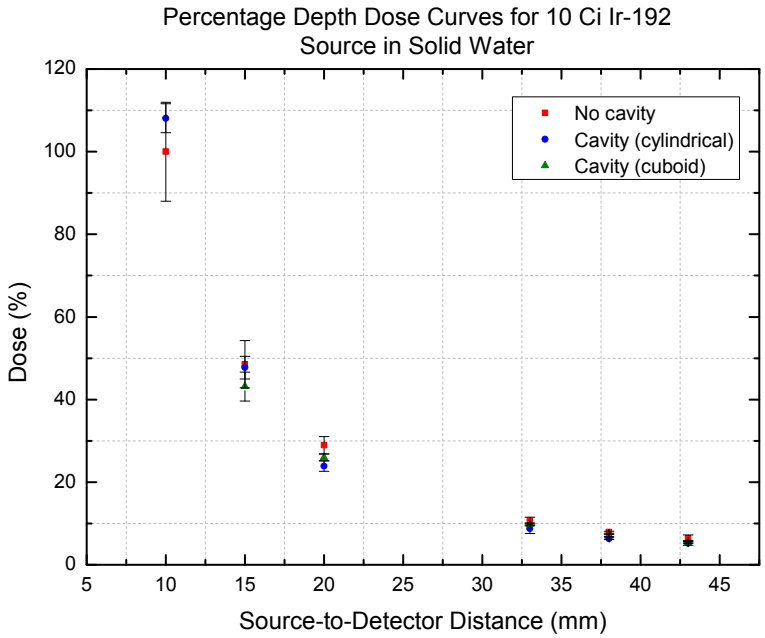

Figure 3.3 Graph of percentage depth dose (PDD) curves in solid water (NB: All measurements normalised to the 'no cavity' measurements).

3.2.2.2 Results

PDD measurements were compared for having no air cavity, a cuboid air cavity and cylindrical air cavity in solid water. The results are shown in Figure 3.3.

The results were normalised to the 'no cavity' measurements. The PDD curves all follow a similar trend, which is expected for these types of curves (i.e. dose rate decreasing with increasing thickness of material between source and detector). Measurements with no cavity were slightly higher than both cavity (cylindrical and cuboid) measurements. This was expected due to the increased backscatter when there was no cavity (i.e. backscatter from the solid water) compared to when there was a cavity (i.e. air). Both cavities produced similar results.

As mentioned in the methodology, the uncertainty in percentage depth dose was determined using Student's t–test. Sample size (N) was equal to 3, hence there was $N-1 = 2$ degrees of freedom (d.f.) and the t–value was 4.303 for a 95%

confidence level. The uncertainty was then also normalised. There was a large uncertainty in percentage dose at 10 mm for no cavity, as this was very close to the source so a small uncertainty in detector placement can mean large uncertainty in dose. Note that there is no data point for the cuboid cavity at 10 mm. This was because the data was taken simultaneously with another experiment, and due to time constraints with the machine, the data that was gathered from this experiment had to be utilised.

3.2.2.3 Discussion

When no air cavity was present, absorbed dose measurements were slightly higher than both cavity measurements of absorbed dose, due to the increased backscatter material. Whether the cavity was cylindrical or cuboid produced negligible difference in results.

3.2.3 Comparison of Backscatter for Air Cavity and No Air Cavity with Change in Angle Between Source and Detector

The aim of this experiment was to compare the absorbed dose to the anterior rectal wall when there was an air cavity present and when there was no air cavity, for different angles (θ) between the horizontal plane at the source and the depression to the detector (Figure 3.4). The absorbed dose was measured at increasing offset distances between the ^{192}Ir source and the MO*Skin*™ detector, hence it was measured as the angle (θ) decreased.

The change in θ results in different scatter conditions between the case of air cavity and no air cavity. The purpose of this experiment was to determine if the difference in dose rate at any of these angles was great enough to warrant creating a hollow Perspex probe, which would then be compared to the solid Perspex probe.

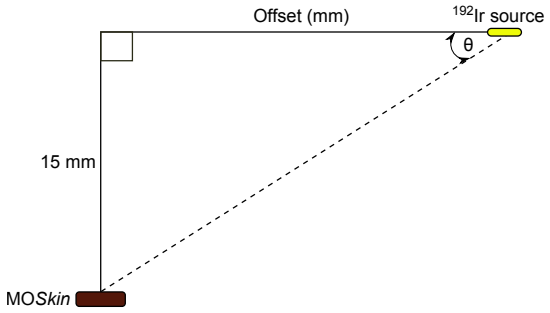

Figure 3.4 Experimental set–up of source relative to MO*Skin*™ detector.

3.2.3.1 Methodology

Solid water slabs of various thicknesses were used to create a phantom with no air cavity. For the cavity measurements, only a cylindrical cavity was used due to the similarity in results found between the cylindrical and cuboid cavities for the PDD measurements. The cylindrical shape was chosen due to the fact that this geometry would be used later on for the probe construction. For the cavity, solid water with a 21 mm diameter cavity was used with the detector taped to the anterior wall of the cavity. The MO*Skin*™ detector was placed at a distance of 15 mm and then 30 mm from the source, for comparison. It was decided that these two set–ups would be completed simultaneously (with one on top of the other) to help minimise set–up errors, which were initially causing problems with this experiment.

For both cavity and no cavity, the source was stepped away (so that θ decreased) from the point just past the tip of the detector (i.e. 3 mm superior to the detector), so that the maximum would not be missed. The source was stopped at arbitrary increments of 3–6 mm where measurements were taken. Measurements of absorbed dose to the anterior rectal wall for the cavity and measurements of absorbed dose to the anterior rectal wall for no cavity were compared.

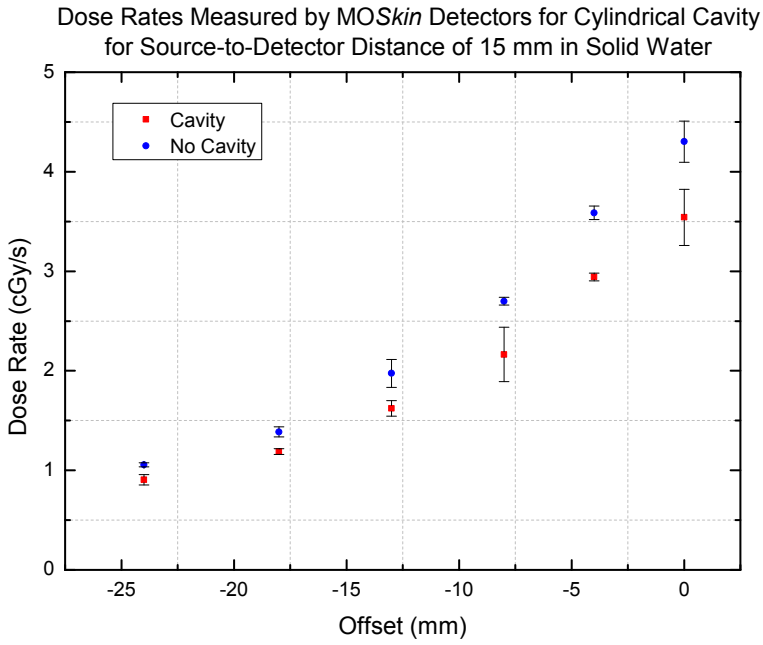

Figure 3.5 Comparison of absorbed dose to anterior rectal wall with air cavity and no air cavity for increasing offset distance at source–to–detector distance of 15 mm.

3.2.3.2 Results

Measurements of absorbed dose to the anterior rectal wall where a cavity was present and where no cavity was present were carried out at different offset distances. This is shown in Figures 3.5 and 3.6, where the offset on the horizontal axis is the distance measured from the position of maximum dose. Figures 3.7 and 3.8 demonstrate the change in dose rate and these were plotted by a MO*Skin*™ detector readout program developed at CMRP.

The uncertainty in dose rate was calculated using a Student's t–test with N = 3, d.f. = 2 and t–value = 4.303 for a 95% confidence level. The calibration factor used was 2.45 $\pm$ 0.02 mV/cGy, as determined previously.

At 15 mm source–to–detector distance, the maximum dose occurred at an offset distance of 0 mm. It was expected that the maximum dose would occur here

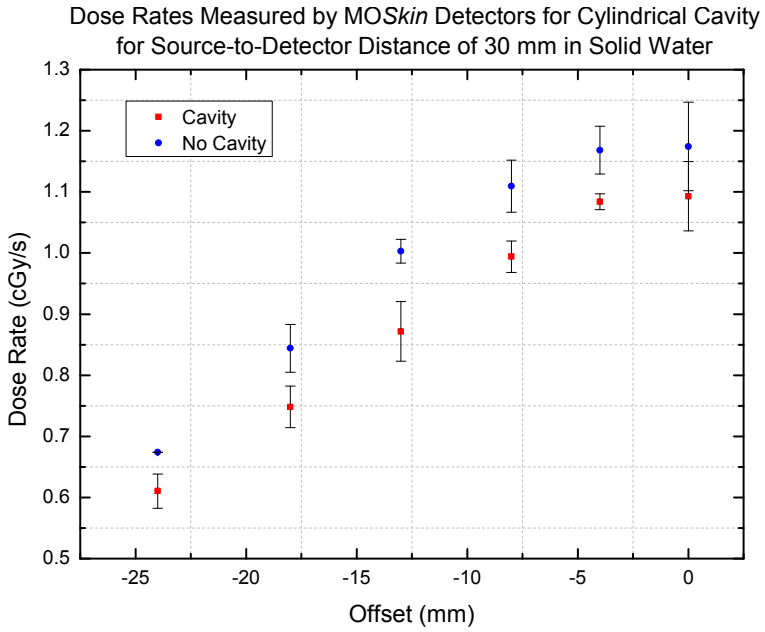

Figure 3.6 Comparison of absorbed dose to anterior rectal wall with air cavity and no air cavity for increasing offset distance at source–to–detector distance of 30 mm.

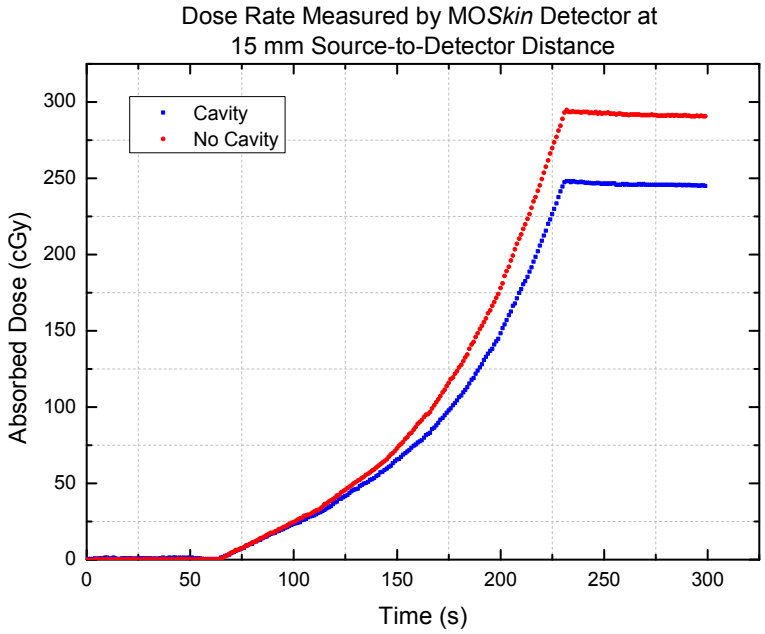

Figure 3.7 Comparison of dose rates using air cavity and no air cavity for increasing offset distance at source–to–detector distance of 15 mm.

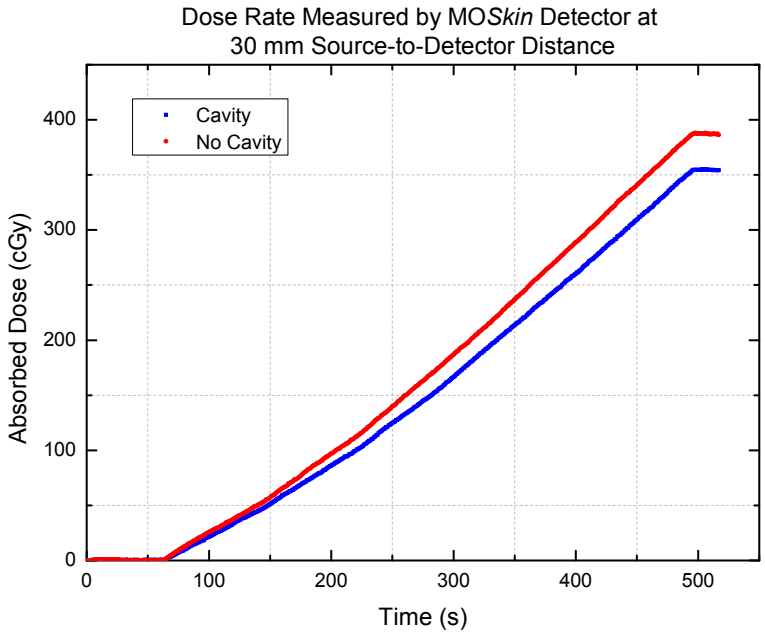

Figure 3.8 Comparison of dose rates using air cavity and no air cavity for increasing offset distance at source–to–detector distance of 30 mm.

as this is the point directly above the sensitive volume of the detector. At 30 mm source–to–detector distance, the position of maximum dose also occurred at 0 mm offset.

For all data points, the no cavity readings were higher than the cavity readings. This was expected due to the higher amount of backscatter introduced by the solid material. At 15 mm source–to–detector distance, as the offset increased, the difference between cavity and no cavity decreased. When there was no offset, the cavity measurement was found to be 17.7% less than the no cavity measurement but at the greatest offset of 24 mm, the difference dropped down to 14.2%. This can be seen in Figure 3.9, along with the results for a 30 mm source–to–detector distance.

At 30 mm source–to–detector distance, the error bars were quite large in comparison to how small the change in dose rate was over the change in offset distance. Cavity measurements demonstrated a range of 6.9–13.1% lower than the no air cavity measurements, however it was difficult to determine a trend with the change in

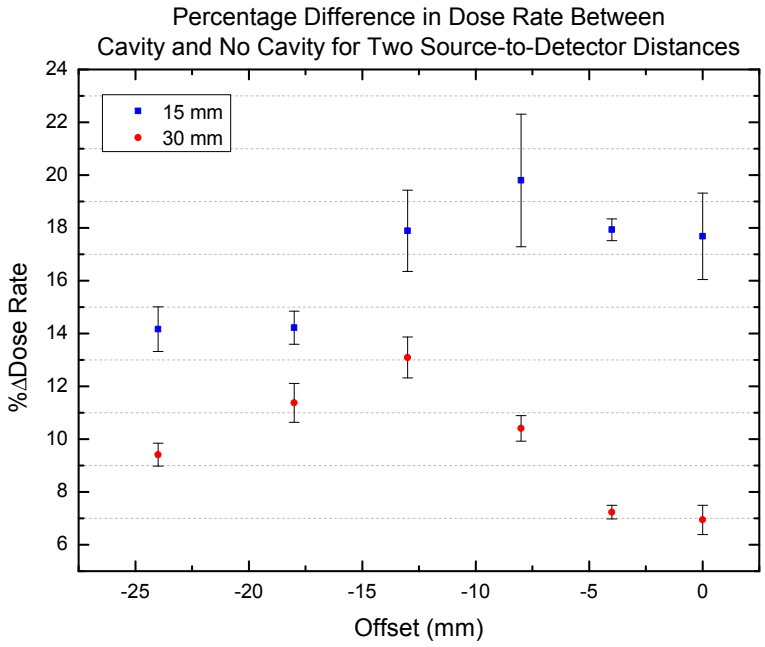

Figure 3.9 Graph of percentage variation in dose rates between air cavity and no air cavity measurements for source–to–detector distances of 15 and 30 mm.

offset distance due to the larger uncertainty than for the 15 mm case. The effect of backscatter was most likely reduced at depth due to the attenuation and scatter of the primary photons before they reached the detector. The source was also not a point source, but a line source. This means that there were less photons being emitted from the two ends of the source compared to the amount emitted from along the length. Hence, when θ was smaller than 90°, less photons were being emitted at this angle to the detector compared to when $\theta = 90°$. The attenuation and scatter also explains the less pronounced decrease in dose rate with offset distance (shallower curve) at 30 mm source–to–detector distance when compared to 15 mm.

3.2.3.3 Discussion

It can be concluded that at shorter source–to–detector distances, there was a greater effect of the difference in backscatter observed between the conditions of cavity and no cavity. As well as this, from the 15 mm source–to–detector distance results, it can be observed that a greater effect of backscatter occurs with a smaller offset dis-

tance. Due to the difference in backscatter between the conditions of cavity and no cavity that were observed in this experiment, it was expected that there would be a difference for the solid and hollow probes as well.

3.3 Gelatine Phantom Measurements with Single MO*Skin*™ Detectors

This experiment looked at the main aim for the brachytherapy part of the project, which was to determine that the arrangement of MO*Skin*™ detectors on a hollow or solid Perspex ultrasound probe replica could provide an acceptable method for taking real–time absorbed dose measurements at the anterior rectal wall.

3.3.1 Methodology

The experimental set–up is shown in Figure 3.10. The phantom was a 15 cm $\times$ 17 cm $\times$ 14 cm Perspex container with a 2.2 cm diameter cylindrical tube attached horizontally inside of it. This tube allows for the insertion of the probe, as shown in the figure, and would be running in the superior–inferior direction if the phantom were a real patient, lying supine. The extra 2 mm of space surrounding the 2 cm diameter probe allowed room for the detectors to be attached and a condom to cover the probe. The phantom also contained a grid of small holes anterior to the tube so that catheters can be inserted.

The phantom was filled with gelatine, which was prepared to the formula of a radiotherapy bolus. The density of the gelatine was measured and found to be 0.976 ± 0.012 g/cm^3. This was 97.6% of the density of water, which demonstrates that this composition of gelatine is an adequate material to use for tissue equivalence.

Normally, for a patient; the ultrasound probe would be inserted into the rectum to provide ultrasound–guided insertion of the catheters into the prostate. Since the phantom was clear and the catheters could be easily observed once inside of the

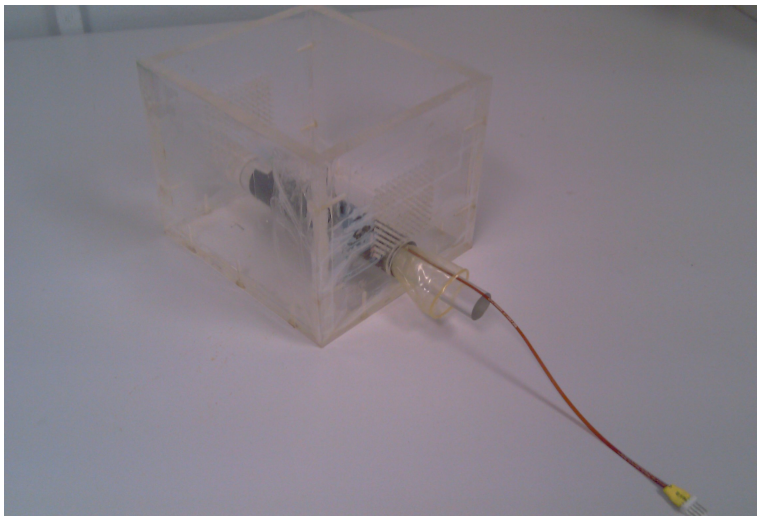

Figure 3.10 Experimental set–up of gelatine phantom and single detector probe.

phantom, this was not needed. Twenty catheters were inserted into the phantom using a common configuration used at SGCCC. The catheters were inserted through what would be the approximate position of the prostate in a patient (the prostate was later drawn onto the plan).

Each of the replica probes (solid and hollow) were also inserted with four MO*Skin*™ detectors attached. Each probe was covered using a condom, as this would be needed for use on a patient for infection control purposes. Detectors were used for the CT scan so that these could be observed on the scan. CT markers were inserted into the catheters as well as being used to locate the approximate position of the prostate on the phantom.

A Philips Brilliance 16 slice Large Bore CT Scanner was used in helical delivery mode to scan the gelatine phantom with the replica probe inside of it. 1 mm reconstructed slices were used and then the scan was repeated with 2 mm slices for comparison. The pitch was 0.567 and the energy was 120 kV. The two datasets were compared and even though 2 mm slices is the standard protocol at SGCCC; it was decided that 1 mm slices would be used for increased accuracy in this experiment.

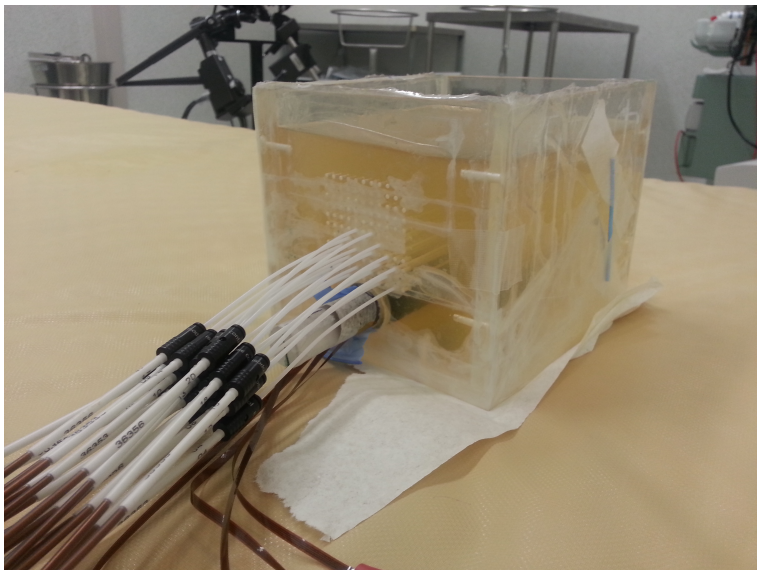

Figure 3.11 Experimental set–up of gelatine phantom with probe, detectors and catheters inserted, ready for treatment delivery.

Treatment planning was completed on an Oncentra Brachy Treatment Planning System, with 18 Gy prescribed in 2 fractions. The plan can be seen in Figure 3.12. A typical prostate shape was contoured on the plan, with the most inferiorly placed detector (detector 4) trailing just inferior to the prostate volume (Figure 3.13). Figure 3.14 shows dose points 1–4 on the plan. There was 100% dose coverage of the prostate volume, with V200 at 9.2% (recommended to be less than 15%) and V150 at 27.3% (recommended to be less than 45%). 2 cc of the rectal volume is recommended to receive less than 70%.

After the plan was completed, the treatment was delivered on a Nucletron HDR unit. The MO*Skin*™ detectors replaced the dummy detectors on the probe, and were then connected to the dosimetry system so that the threshold voltage could be read out in real–time. The change in threshold voltage was recorded and later converted to absorbed dose using the appropriate correction factors. The measured absorbed doses were compared to the doses calculated by the TPS. A comparison of absorbed dose was made for using each of the different replica probe designs. Distance–to–Agreement (DTA) measurements were completed along with the per-

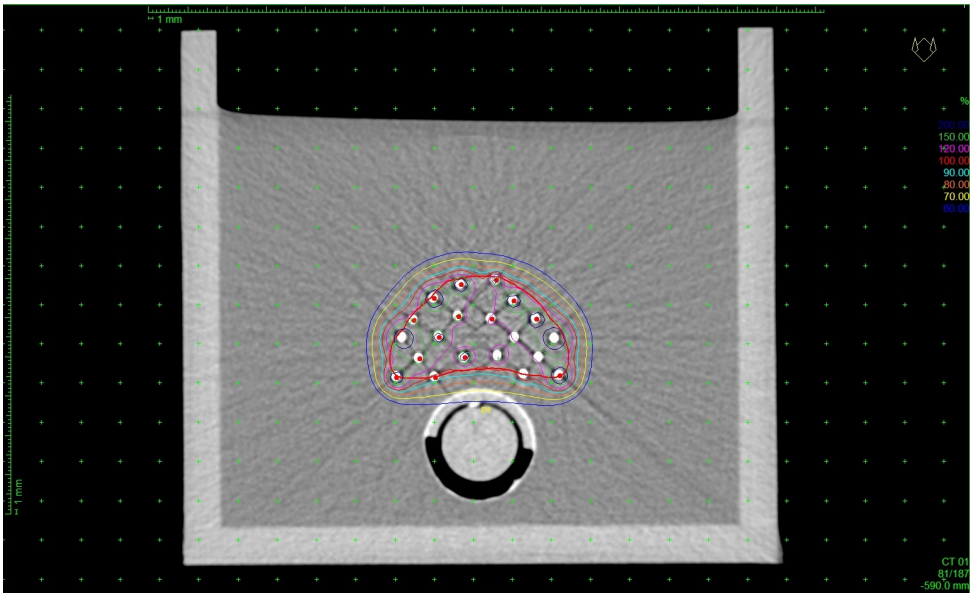

Figure 3.12 Treatment plan on CT scan of gelatine phantom.

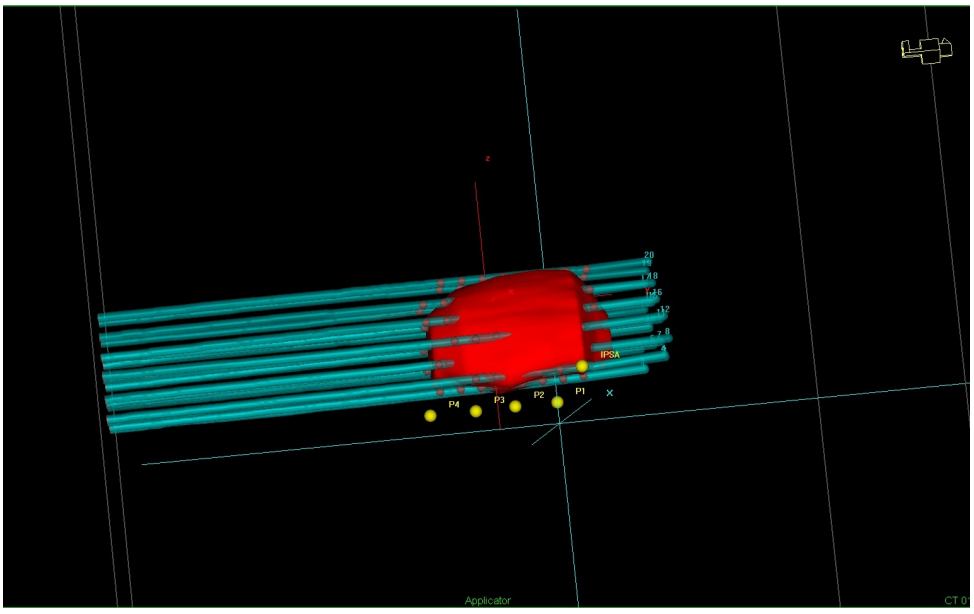

Figure 3.13 Prostate volume contoured on treatment plan, with catheters inserted. Relative position of MO*Skin*™ detectors can be observed.

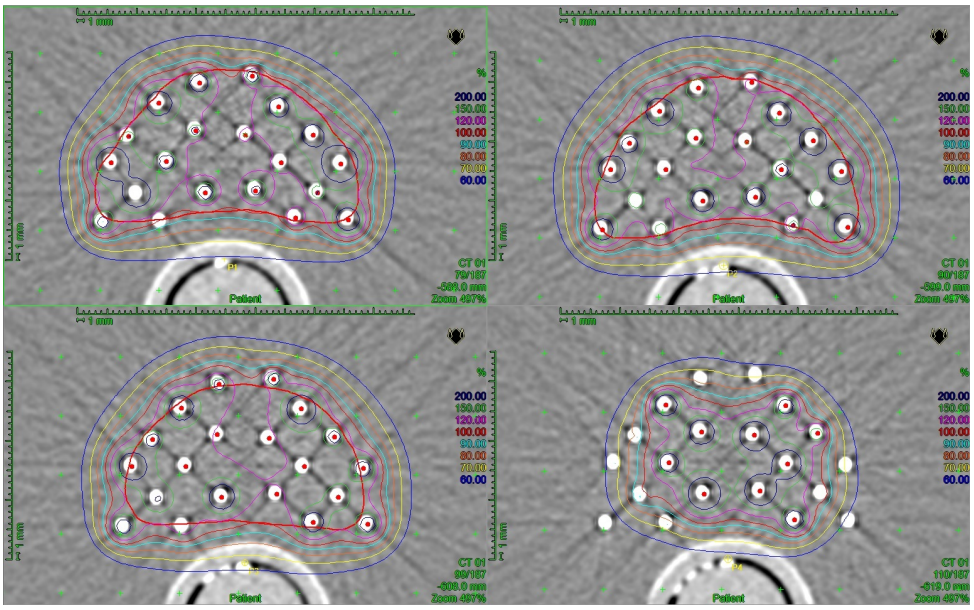

Figure 3.14 Treatment plan demonstrating dose distribution on slices of each of four MO*Skin*™ detectors.

centage difference comparison. DTA is defined as the distance between the location of the point of the measured dose to its corresponding isodose line [109]. Inability of the measured point to not only fall within the acceptable DTA distance, but to fall outside the dose–difference measurement, indicates its failure to have produced a good measurement in a high dose gradient region [106, 109]. For brachytherapy, the DTA tolerance is 2 mm [110]. Petrokokkinos et al. (2011) completed an HDR brachytherapy study using ^{192}I to verify their TPS dose distributions experimentally and found the TPS and measured doses to be in agreement to within 5% dose difference and 2 mm DTA. They found this agreement to be true except for in regions close to the penumbra of the shielded applicator (up to 10% difference) [110].

The DTA value is based on the γ value, which is a method developed to quantify the differences in dose distributions, in terms of both dose and distance. The γ value can be separated into both the DTA and dose difference tests, and is typically utilised to allow the easier analysis of large quantities of data from multidimensional detectors. However, γ analysis is not simply a composite distribution, which gives

Detector	Hollow CF (mV/cGy)	Uncertainty Hollow CF (mV/cGy)	Solid CF (mV/cGy)	Uncertainty Solid CF (mV/cGy)
1	2.29	0.08	2.54	0.02
2	2.47	0.01	2.42	0.09
3	2.47	0.08	2.56	0.09
4	2.48	0.05	2.65	0.11

Table 3.1
Calibration factors (CF) for four MO*Skin*™ detectors on hollow and solid probes used in HDR Brachytherapy measurements.

only a pass or fail response; but a numerical value to allow display/analysis. It does this by scaling the difference between reference and evaluated points as a fraction of the acceptance criteria, with a γ value of less than or equal to one being within the accepted criteria [106, 109]. γ analysis was not utilised for this project as only four point doses needed to be analysed, hence a numerical value to represent the difference in a display was not required.

3.3.2 Results

The treatment plan was completed using the solid probe, since the TPS assumed a water–filled rectum. The same plan was then delivered when having the hollow probe inserted to be able to compare the differences in dose measured when using the two different probes. To begin with, large deviations were observed between measured and planned doses, so it was decided to use individual calibration factors for each detector instead of the averaged factor found previously. Determination of the calibration factor was completed in solid water blocks, with a source–to–detector distance of 15 mm and delivery time of 15 s. The calibration factors are shown in Table 3.1 for the detectors 1–4 on each of the probes.

As can be seen from this table, the calibration factors did vary, so these individual factors were applied. The average error was less that 1.5% of the calibration factors, with the maximum error (in detector 4, solid probe) being less than 3.5%. An example of the change in absorbed dose of each detector over time is seen in Figure 3.15. The increase in dose was stepped, demonstrating the different source positions. The

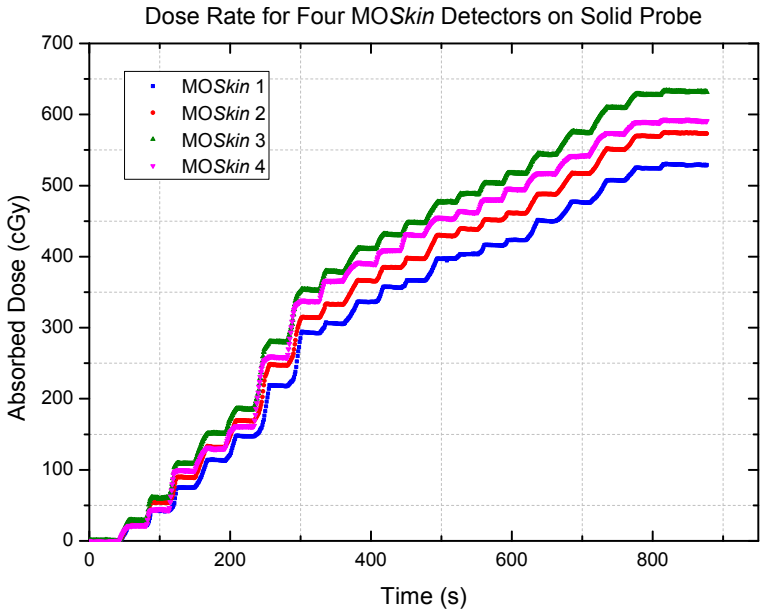

Figure 3.15 Graph of change in absorbed dose measured by each of the MO*Skin*™ detectors over time during treatment delivery to the gelatine phantom.

doses that were measured during the treatment plan delivery, along with the planned doses, are displayed in Figures 3.16 and 3.17 and can be found in Tables A.1 and A.2 in the Appendix.

Both graphs appear to show large error, calculated using Student's t–test. However, the average error was only 4% of the measured doses. Observing the averaged dose values alone, 50% of all detectors were within ±5% of the planned doses, as can be seen in Figure 3.18. Further agreement was demonstrated by DTA measurements, which were completed, and which demonstrated whether any measured dose deviations were within the accepted range and are shown in Table 3.2. It can thus be seen that all DTA values were acceptable, and hence if DTA measurements are accounted for, 100% was observed.

For the hollow probe, the measured values for detectors 2 and 3 were within experimental error of the TPS. Detector 1 measured a result that was outside of error from the expected. Even though it was found to deviate from the TPS by 6.7%, its

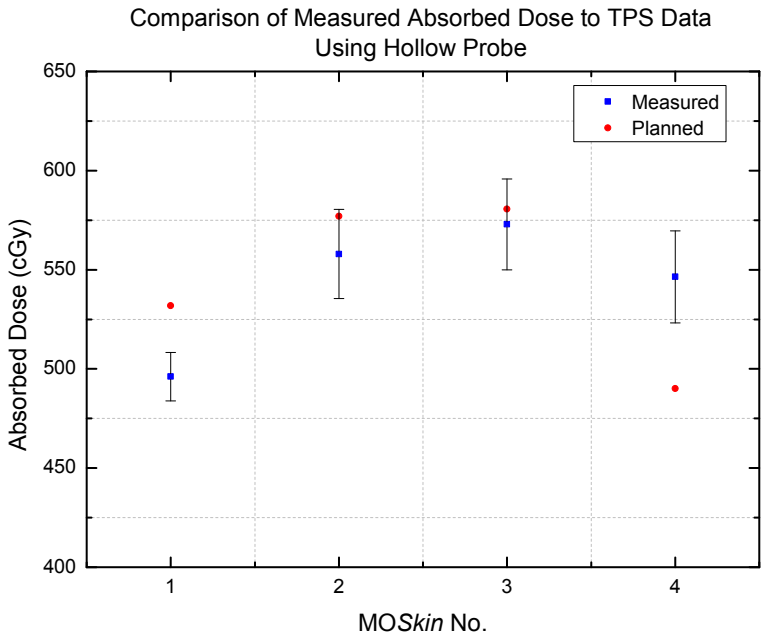

Figure 3.16 Graph of absorbed dose taken from the brachytherapy TPS data in comparison to the dose measured experimentally, using four MO*Skin*™ detectors on hollow probe in HDR Brachytherapy.

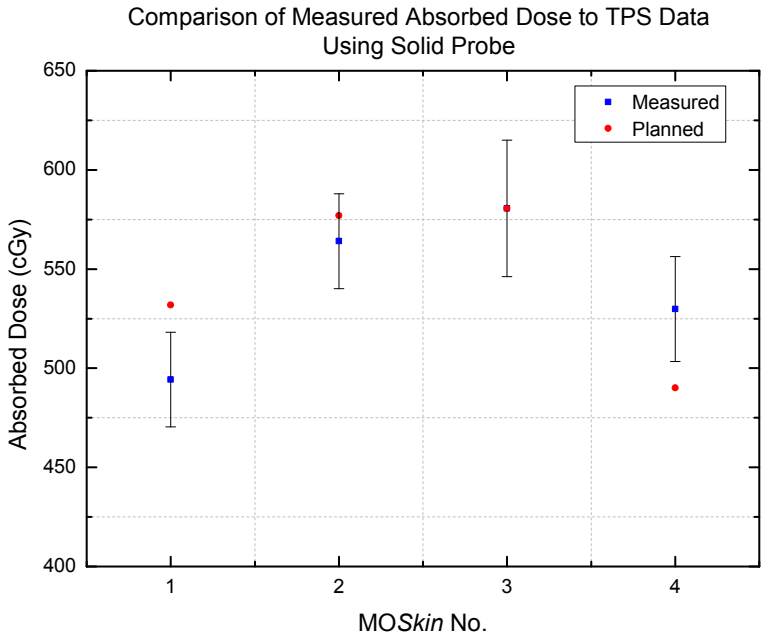

Figure 3.17 Graph of absorbed dose taken from the brachytherapy TPS data in comparison to the dose measured experimentally, using four MO*Skin*™ detectors on solid probe in HDR Brachytherapy.

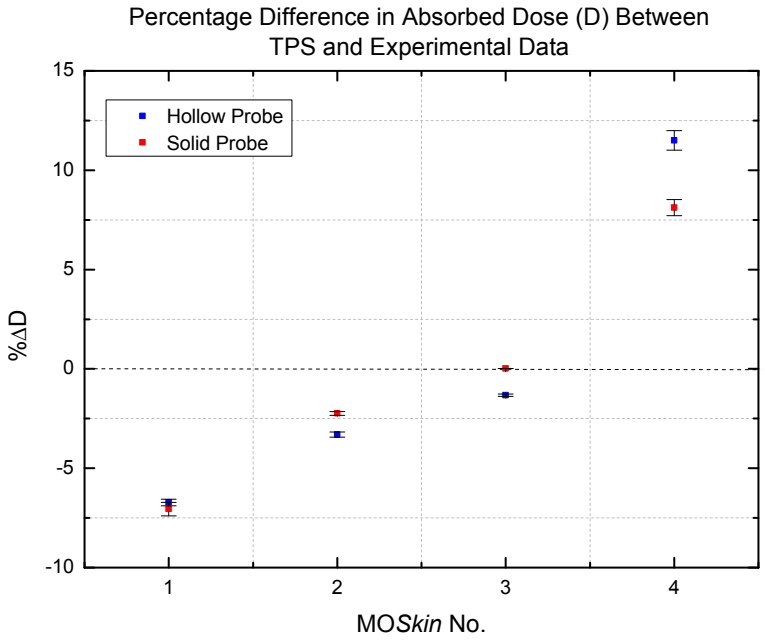

Figure 3.18 Graph of percentage variation of absorbed dose between brachytherapy TPS data and measured dose, using four MO*Skin*™ detectors on solid and hollow Perspex probes.

Probe Type	Detector	DTA (mm)
Hollow	1	1.3
	4	1.2
Solid	1	1.4
	4	0.9

Table 3.2
Table of Distance–to–Agreement (DTA) values for HDR brachytherapy experiment utilising single MO*Skin*™ detectors.

DTA was 1.3 mm, which was within tolerance. The result from detector 4 showed a larger deviation of 11.5% from the expected result, and was outside of the error bounds. However, it also had an acceptable DTA of 1.2 mm.

The solid probe showed similar results, with detector 2 and 3 falling within the error limits. Detectors 1 and 4 fell outside of experimental error, with detector 1 deviating from the expected value by 7.1%, and detector 4 by 8.1%. The results from these two detectors had DTA values that were within tolerance. Detector 1 had a DTA of 1.4 mm and detector 4 had a DTA of 0.9 mm.

At this stage angular dependence was believed to be negligible as the source positions were always within the range of 90–270° of the MO*Skin*™ detectors (at 0°). Angular dependence for MO*Skin*™ detectors used in HDR brachytherapy has previously been investigated [108] and results were found to demonstrate an under–response at the back of the detector (i.e. at 180°) due to the asymmetric construction of these detectors. The Si substrate on the back of the detector caused a larger attenuation. Even though this same study found an over–response at the front of the detector (due to a thin Aluminium contact layer) [108], it was not observed in this experiment for 75% of detectors. Another study found no effect of angular dependence around the central axis of the MO*Skin*™ detector for the range of 0–330°, and also no effect in the azimuthal direction [111]. However, angular dependence was further investigated in the next experiment to determine its effect for this particular experimental set–up. Slight positional uncertainties in the very steep dose gradient region at the anterior rectal wall were also thought to account for the discrepancies.

Energy dependence was also considered. Since the range of distances from the sources to the detectors was large (≈1.5–5 cm), the energy dependence affected the measurements. The measurements with the source at large distances from the detectors would contribute only a small amount to the overall dose, so calibration was performed for the detectors at a small distance (1.5 cm). The energy dependence effects from the source at large distances from the detectors would be minimal due to the small relative dose contributions.

Large variations in dose between CT voxels in regions of steep dose gradients were observed. To demonstrate this, Figure 3.19 includes uncertainty on TPS data points. The ‘error bars’ that can be observed in this figure are not statistical, but instead are an indication of the range of dose between adjacent voxels on the plan dataset. This means that these bars represent the maximum and minimum dose level that was observed over the range of dose voxels that were within the locational

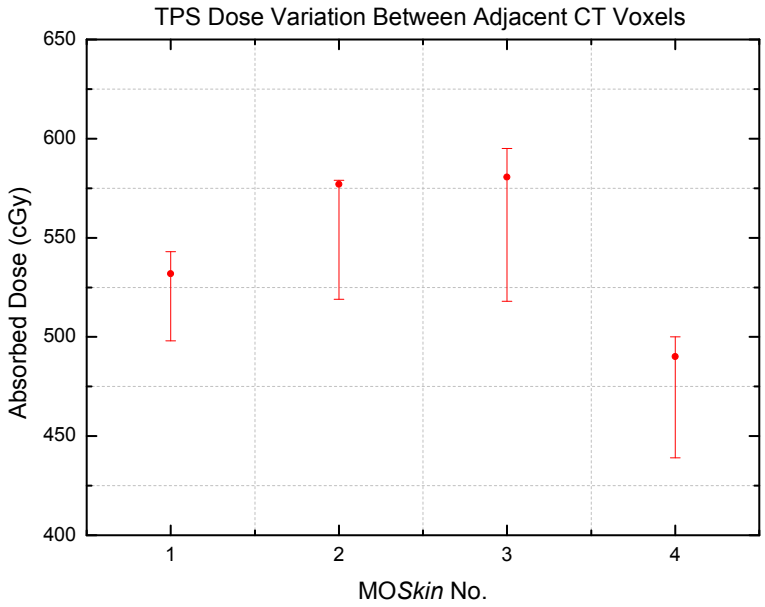

Figure 3.19 Graph demonstrating HDR brachytherapy TPS data uncertainty due to large variations in dose between adjacent CT voxels.

uncertainty of the detector positioning. For example, for the readings taken at one detector position, the data point corresponding to the position of the measured dose was located just on the anterior surface of the detector on the CT image. So this point was used to compare the experimental results with. Even though the image was quite clear, the location of the sensitive volume of the detector was not as clear, therefore readings were taken at five points on the detector (anterior, posterior, left and right edges, and centre) to determine the TPS uncertainty. This was repeated on a slice both superior and inferior to the central slice. The largest deviations (both positive and negative) out of all these points were used to plot the TPS error bars on the corresponding point, to demonstrate the spread of dose around this point.

The 'error bars' that were acquired for the TPS data were quite large and were in the range of 2–63 cGy. This demonstrated a very large difference in dose between adjacent voxels, adding to the uncertainty in measurements. It was therefore important to ensure the TPS dose reading matched the position of the measured dose as accurately as possible. The sub millimeter resolution of the CT scan on the planning system allowed for easy visualisation of the dual detector, which assisted

in reducing this uncertainty. No image artifacts, such as those from the wires, were thought to obstruct the readings from the plan.

The differences observed between solid probe results and hollow probe results were not significant. This may be due to the fact that most source positions were positioned at a distance greater than 15 mm source–to–detector distance so the backscatter differences were not as pronounced than from a shorter source–to–detector distance. This was shown in the previous experiment that compared backscatter for air cavity and no air cavity. Due to the similarity in results, it can be concluded that the solid probe did not increase the dose to the anterior rectal wall, despite the extra backscatter material introduced to the rectum when utilising this probe.

3.3.3 Discussion

Even though only 50% of detectors on both probes demonstrated results to within $\pm 5\%$ of the TPS, all DTA values were within tolerance. The differences were therefore believed to be slight positional errors, although, the discrepancies may also be due to angular dependence, but further investigation was needed. The inability to perform image–guidance to align detectors to their planned position before treatment was a disadvantage. However, geometrically, the probes did provide an improved method of reproducibility for the treatment of the prostate using HDR bracytherapy.

3.4 Gelatine Phantom Measurements with Dual MO*Skin*™ Detectors

The measurements were repeated using dual MO*Skin*™ detectors. The purpose of this experiment was to improve the accuracy of the measurements at the expense of having larger detectors. Dual MO*Skin*™ detectors are a face–to–face arrangement of the detectors, previously reported to be successful in reducing angular dependence by taking the average in response of the detector pair and hence cancelling the asym-

metry of the detector chip [3, 84]. Dual MO*Skin*™ detectors were found previously to have an angular dependence of ±2.5% from all incident beam angles [3].

3.4.1 Dual MO*Skin*™ Detector Calibration

The MO*Skin*™ detectors were calibrated in solid water at a source–to–detector distance of 2.5 cm to reduce the effect of discrepancies at a closer distance. Each detector was calibrated both facing upwards and downwards, so that an average calibration factor was determined for each detector orientation. An average calibration factor was then found between the upwards average and downwards average, as per the requirement for a dual MO*Skin*™ detector calibration.

The average calibration factors were determined to be 2.50 ± 0.06 mV/cGy for the upwards–facing detectors, and 2.14 ± 0.04 mV/cGy for the downwards–facing detectors. An average calibration factor between these two values was therefore determined to be 2.32 ± 0.07 mV/cGy, which was applied to all dual MO*Skin*™ detector measurements for this experiment.

3.4.2 Treatment Delivery

3.4.2.1 Methodology

This experiment was set up as per the previous measurements utilising the single MO*Skin*™ detectors in the gelatine phantom, however, this time dual detectors were attached to the probe. No noticeable differences between the solid and hollow probe measurements were apparent, therefore only one probe, the solid, was utilised for this experiment. The readout unit provided measurements of a maximum of five single detectors, hence, only two dual detectors were possible and were placed at positions 1 and 3 on the probe.

After the insertion of twenty catheters and the solid probe into the phantom, a CT scan was taken of the phantom using 1 mm slices, 0.1 mm image resolution,

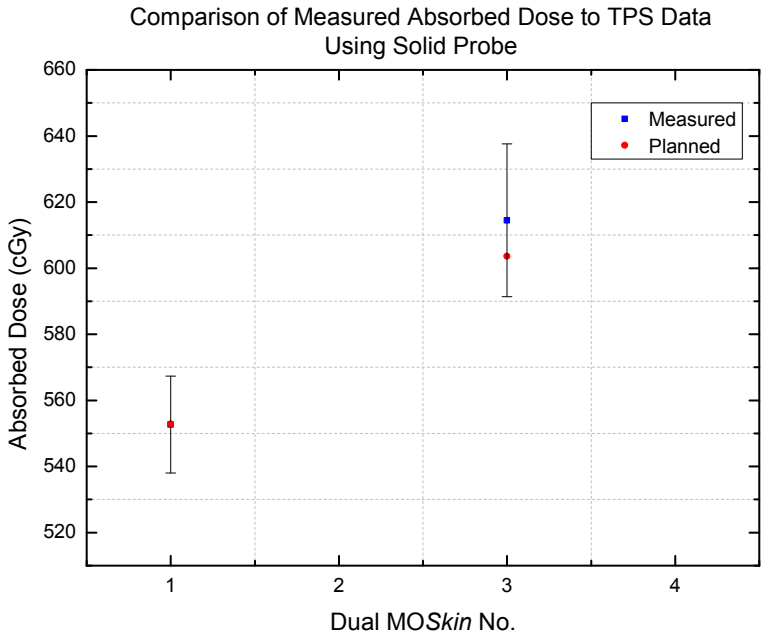

Figure 3.20 Graph of absorbed dose taken from the brachytherapy TPS data in comparison to the dose measured experimentally, using four dual MO*Skin*™ detectors on solid probe in HDR Brachytherapy.

0.567 pitch, at an energy of 120 kV. A treatment plan was created and 18 Gy prescribed in 2 fractions with 100% of the dose covering the prostate volume. The treatment was delivered and dose read out on the dual MO*Skin*™ detectors.

3.4.2.2 Results

The measured values were compared to the TPS data. The results obtained (Figure 3.20) demonstrated very good agreement for the two dual detectors. Table A.3 in Appendix A also displays the results.

For dual detector 1, a discrepancy of less than 1% was observed between measured and TPS results. For dual detector 3, a difference of less than 2% was observed. Both measurements fell within experimental error of the TPS. DTA measurements were not needed as the agreements were very good.

The error bars were still large, attributed to the pressure that the detectors

were under when inside the phantom. The tight fit of the probe inside the phantom due to the extra thickness of the dual detectors caused this variation. However, the average error was approximately 3% of the measurements and very small discrepancies were observed between measured and TPS data.

3.4.2.3 Discussion

These results showed that the differences observed in the single detector experiment could be due to angular dependence, as the dual detectors showed better agreement. Hence, the probe system could be improved by utilising the dual MO*Skin*™ detectors.

3.5 Conclusion

For the single MO*Skin*™ detectors, 50% of detectors measured dose to within ±5% of the expected TPS dose. If DTA measurements were accounted for, then all measurements were within agreement of the TPS, as all DTA values were acceptable. The differences between results produced from utilising the hollow and solid probes were negligible. Measurements using dual MO*Skin*™ detectors demonstrated 100% agreement between measured and TPS doses. DTA measurements were therefore not required, which would be ideal in a clinical situation, where time is a limitation. Hence, the 100% agreement demonstrated by the dual detectors would be beneficial over the single detectors, which required DTA measurements to bring all results within agreement of the TPS doses. The discrepancies observed in the single detector experiment were attributed to angular dependence; however, slight positional deviations in the high dose gradient region can also explain discrepancies.

Chapter 4

Comparison of TomoTherapy® TPS Calculated Dose with MO*Skin*™ Detectors Placed in Phantom on Solid Endorectal Carrier

The next aim of the project was to test if the probe and MO*Skin*™ detectors were acceptable for use during a prostate boost treatment using Helical TomoTherapy®. The probe would assist in immobilisation of the target geometry for improved accuracy in plan delivery, while the MO*Skin*™ detectors mounted on the probe could measure the dose to the rectal wall in real time. The high dose gradient region where the rectum is positioned means positional accuracy is extremely important (Figure 4.1).

4.1 Treatment Planning and Equipment

The TomoTherapy® boost was a hypofractionated schedule of 21.1 Gy in 2 fractions. After further studies have been completed, this boost will be followed by IMRT with a prescription of approximately 46 Gy in 23 fractions. Although this prescription is currently being investigated by preliminary studies, hypofractionated treatment delivery to the prostate has been previously shown to produce favourable

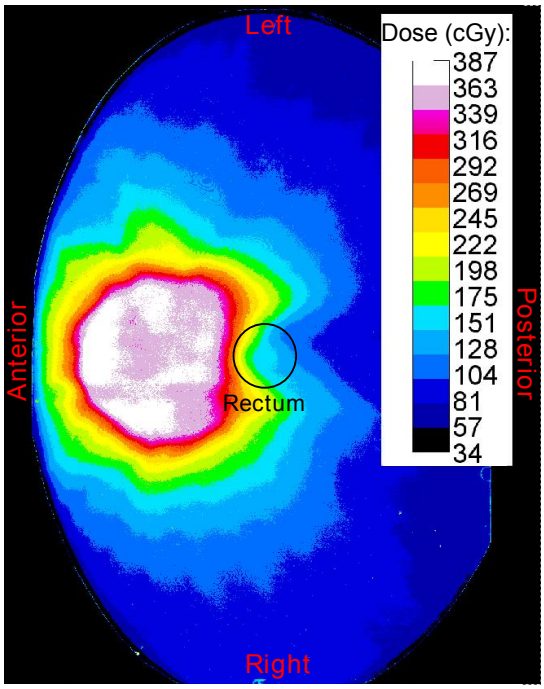

Figure 4.1 Dose map of TomoTherapy® prostate treatment plan.

results [53–55], as discussed in Section 2.3.

Approximately a 10.5 Gy fraction is usually delivered in three parts as the patient passes through the TomoTherapy® unit, with 3.5 Gy delivered per pass. Thus, in theory, the dose can be verified and corrected for after the first pass, before the next part of the fraction is delivered. Again, the hypothesis was that MO*Skin*™ detectors could be deployed to indicate dose to the rectum within $\pm 5\%$.

This method was tested using a TomoTherapy® unit at Liverpool Hospital, New South Wales. The TomoTherapy® Hi–Art® treatment planning system was utilised. An IMRT Head and Torso Freepoint Phantom (CIRS, model 002H9K) was used for these measurements. This phantom is constructed from tissue equivalent, epoxy materials with cylindrical cavities that allow rods to be inserted, for example, rods that can hold an ionisation chamber or rods made of bone equivalent material. The cylindrical cavities can also be rotated to be placed in different positions [112]. It is these cavities into which the probes can be inserted.

The Rectafix® system has been developed to improve positioning and immobilisation in the treatment of the prostate through EBRT, for both proton and photon boosts [7, 8]. The replica probes utilised in this experiment were modelled similarly to the Rectafix® but were also combined with a one dimensional array of MO*Skin*™ detectors. The Rectafix® and replica probes were both composed of Perspex [8]. The mass densities for the Rectafix® and also the probes were 1.09–1.12 g/cm^3. The solid and hollow probes that were designed for this project had a diameter of only 20 mm, however the phantom cavities have a diameter of 25 mm. Therefore Perspex tubing was used to create another layer around the probes so they could fit properly inside the phantom.

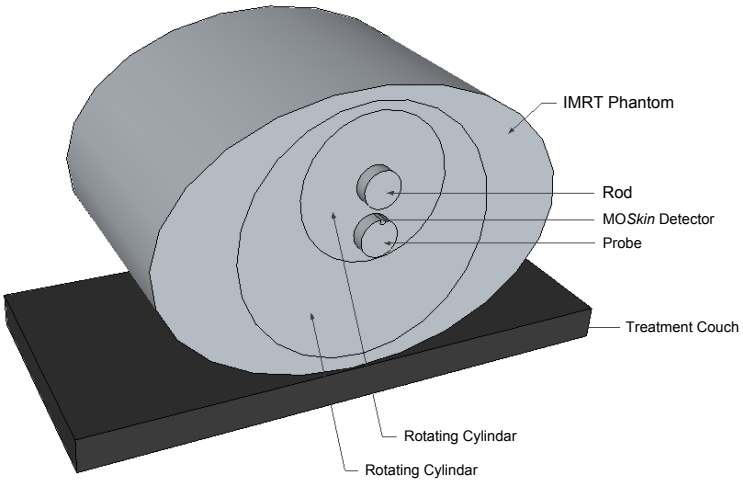

Figure 4.2 Experimental set–up of IMRT phantom with MO*Skin*™ detector on probe.

Megavoltage (MV) CT scans using the TomoTherapy® unit at approximately 3.5 MV [113] were first taken of the phantom with the probes and a single MO*Skin*™ detector inserted. However, on some of the images the MO*Skin*™ detectors were not clearly visualised, so kilovoltage (kV) CT data sets were obtained instead. The planning CT scans were taken using a Siemens Sensation 4 Multi–slice CT Scanner, and these images were aligned with those taken prior to the treatment delivery for image guidance.

Treatment plans were completed on the datasets so that the TPS dose calculated at the positions of the detectors on the scan could be determined and later compared to the measured dose. A patient's treatment plan was used and adapted to the phantom shape so that realistic PTVs and OARs could be overlayed onto the phantom plan. The prescription for a prostate treatment plan using Helical TomoTherapy® at Liverpool hospital is 19 Gy in 2 fractions prescribed to the PTV. To achieve the sharp dose fall–off, an inhomogeneous distribution is acceptable. Typically a prescription is 80–90% of the target maximum dose to ensure the tumour boundary is on the steepest part of the dose gradient. This is achieved by setting the dose prescription to 21.1 Gy, where 90% (i.e. 19 Gy) of the target maximum should cover at least 95% of the PTV.

The aim was to limit the rectal dose to 14–16 Gy, with the maximum occurring in the overlap region between rectum and PTV. Due to this overlap, where necessary, the PTV adjacent to the rectal volume may receive a minimum dose of 16 Gy. Otherwise a total dose of 19 Gy should be delivered to the PTV. The minimum dose to the CTV is 19 Gy and the maximum dose to the urethra is 21 Gy. These objectives were achieved for all plans used in this experiment. On each plan, the co–ordinates of each detector were determined, and the dose read out at these points. These readings were divided into six fractions and compared to the experimental results.

4.2 MO*Skin*™ Angular Dependence

Consideration of angular dependence is important for using MO*Skin*™ detectors in TomoTherapy® due to the helical delivery of dose. MOSFET detectors have demonstrated an angular dependence in the past [6, 85], so this needed to be determined for the current study. However, due to the fact that they cancel out the asymmetric shape of the MOSFET; dual MOSFETs, were found previously to

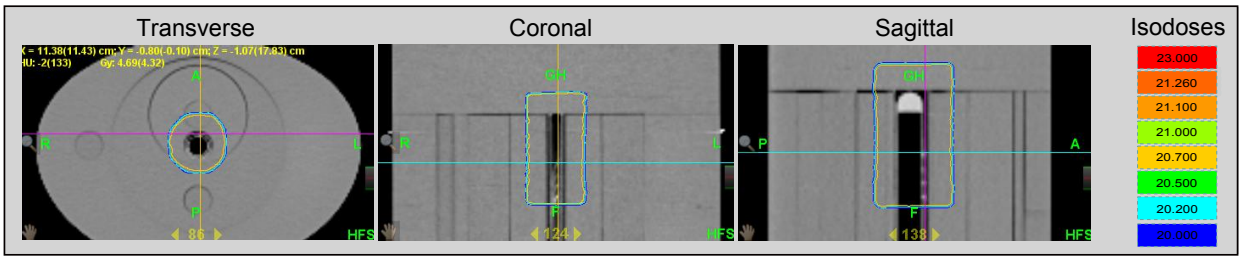

Figure 4.3 Plan of composite uniform distribution for calibration.

have an angular dependence of ±2.5% from all incident beam angles, and hence they can be used for treatments delivered by rotation such as TomoTherapy® [3]. It was hypothesised that a single detector without the composite spatial resolution increase would more precisely indicate the rectal wall interface dose where the dose gradient may change rapidly. The use of single MO*Skin*™ detectors was therefore investigated initially, before investigating dual MO*Skin*™ detectors.

TomoTherapy® is a rotational treatment with different beamlets approaching from different angles of rotation and it is therefore very difficult to take angular dependence into account. A plan with a composite uniform dose distribution was created and delivered helically and then measurements were taken at θ = 0°, 90° and 180° using four MO*Skin*™ detectors to observe any potential effect of angular dependence. It was named a 'composite uniform dose distribution' as it was just a low dose gradient distribution into which the detectors were placed. The differences in readings between all angles were $\leq$2% for 75% of measurements, and $<$5% for 92% of measurements. Hence, the detector calibration was performed by delivering this composite uniform dose distribution so that the absorbed dose on the detector would be from all angles. For the actual experiment, measurements were taken at three different angles to see if there was any effect, as will be outlined in Section 4.3.

4.3 TomoTherapy® Measurements with Single MO*Skin*™ Detectors and IMRT Phantom

4.3.1 MO*Skin*™ Detector Calibration

4.3.1.1 Methodology

The MO*Skin*™ detectors were calibrated using the TomoTherapy® unit (approximately 6 MV [113]) with a 5×40 cm^2 field and a composite uniform dose delivered helically (shown in Figure 4.3). The solid probe was utilised with four MO*Skin*™ detectors in the IMRT phantom. The composite uniform dose allowed the effect of angular dependence to be minimised as the beamlet weights would not be heavily weighted from any angle (except to account for greater lateral thickness of body contour) as there were no avoidance structures or OARs involved. The measured voltage readings by the detectors were compared to the TPS data to determine the calibration factors measured in mV/cGy. The plan in Figure 4.3 demonstrates the composite uniform dose distribution.

The dose measured by the MO*Skin*™ detectors was also verified by a CC13 ionisation chamber in the IMRT phantom. The phantom was scanned with a CC13 ionisation chamber inserted into a solid water equivalent rod. A plan was created and dose was observed to be uniform over the whole rod and chamber. Due to this uniform distribution, readings of absorbed dose from the TPS were taken at the position that the MO*Skin*™ detectors would be positioned on the probe, and then compared to the ionisation chamber reading.

To test whether the actual MO*Skin*™ detectors were capable of measuring the dose that was planned, a single detector was placed in a region of low dose gradient, using one of the prostate treatment plans. The reason for this was to determine whether discrepancies between measured and planned doses were due to the actual detector, or the high dose gradient that the detectors would later be positioned in.

The point chosen for this was the isocentre, which was in the middle of the PTV.

This measurement was also verified by a CC13 ionisation chamber. However, the identical reference point for measurement with both ionisation chamber and MO*Skin*™ could not be matched, due to the dimensions and physical location within the probe. The MO*Skin*™ was at surface of the probe, whilst the ionisation chamber was at the centre. This meant that the dose agreement needed to be reported separately and compared to the TPS dose at two different locations.

4.3.1.2 Results

For calibration, the absorbed doses were determined from a plan with a composite uniform dose distribution. The changes in voltage (ΔV) across four MO*Skin*™ detectors were compared to the corresponding planned dose readings. The readings and calibration factors (CF) for four MO*Skin*™ detectors using the solid probe are displayed in Table 4.1.

As can be observed from the table, the calibration factors were very close in value to each other, which is what was expected in a uniform field. The largest deviation was less than 2%. This dose was verified by the CC13 ionisation chamber, which the MO*Skin*™ detectors were calibrated against. This calibration factor was determined to be 2.4 $\pm$ 0.1 mV/cGy. The errors in the calibration factors were determined by taking into account uncertainty for both the voltage readings and dose measurement from the plan. The error in voltage reading was $\pm$1 mV, as this was the smallest reading that the reader could measure to. The dose per fraction uncertainty was taken to be 0.1 cGy as this was determined to be a reasonable estimate when reading the dose from the plan. An average of all calibration factors from Table 4.1 was taken and found to be 2.382 $\pm$ 0.027 mV/cGy so this was taken to be the calibration for all MO*Skin*™ detectors for this experiment. The uncertainty was calculated using Student's t–test, with N = 4, d.f. = 3, and t–value = 3.182 for a 95% confidence level.

Detector	ΔV (mV)	CF (mV/cGy)	CF Uncertainty (mV/cGy)
1	247.1	2.400	0.004
2	248.2	2.385	0.004
3	250.1	2.359	0.004
4	249.0	2.386	0.004

Table 4.1
Calibration factors for the four MO*Skin*™ detectors used in TomoTherapy® measurements.

The other uncertainty which needed to be accounted for, not only for calibration factors but for the rest of the experiment, was positional accuracy. The indents on the probes assisted in positioning the detectors; however, there would still be some discrepancy from the planned position. The treatment CT scan was aligned with the planning CT scan before the dose was delivered to the detectors, however, there would still be some set–up uncertainty between the two datasets, which needs to be considered.

The other measurement completed was to determine whether the MO*Skin*™ detectors performed well in a region of low dose gradient. Hence a single detector measured the dose in the centre of the PTV. The difference between planned and measured doses, for both MO*Skin*™ detector and CC13 ionisation chamber, was found to be $<1\%$. This demonstrated that possible discrepancies observed in the following experiments were not due to the inability of the MO*Skin*™ detectors to record dose accurately, but rather, the high dose gradient region.

4.3.2 Treatment Delivery

4.3.2.1 Methodology

The absorbed dose measurements were then carried out using MO*Skin*™ detectors on both the solid and hollow probes. The experimental set–up is shown in Figure 4.4. Treatment plans were completed and optimised for each of the probes; first utilising a $2.00 \times 2.00 \times 2.00$ mm^3 dose grid (i.e. 2 mm slice thickness) for calculation and then a $1.37 \times 1.37 \times 2.00$ mm^3 dose grid (i.e. 4 plans in total). The former is the

Figure 4.4 Experimental set–up of IMRT phantom, probe, extra Perspex layer around probe and MO*Skin*™ detectors.

calculation grid used in a normal treatment plan for TomoTherapy® at Liverpool Hospital; the latter is a fine dose grid to see if the results could be improved with its utilisation. The size of the fine dose grid was determined by the size of the field of view (FoV) when scanning the phantom, which was 35 cm^2. This was the smallest FoV possible (and hence the smallest calculation grid possible) to encompass the entire phantom.

The dose prescription was delivered as per the treatment plans. Since the TomoTherapy® TPS does not assume the rectum to be water–filled (unlike the Brachytherapy TPS), it applies inhomogeneity corrections. Therefore there was no need to utilise the same plan for both probes for comparison like in the brachytherapy case. Instead, the plans were optimised for each type of probe, as well as for each dose grid.

Measurements were taken at three different angles by rotating the probe to quantify the effect at different positions on the rectal wall. However, the focus was on the anterior rectal wall, as the overall effect of dose at the other locations was not as significant, given the lower expected doses. Letting $\theta = 0°$ be the most

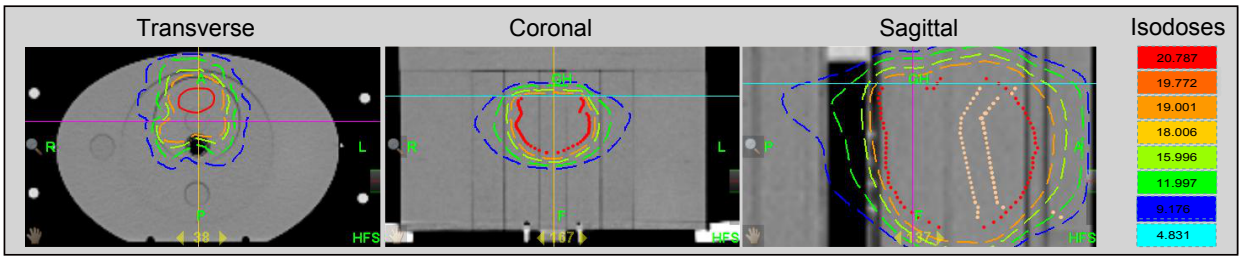

Figure 4.5 Hollow probe plan using 2.00 × 2.00 × 2.00 mm^3 dose grid.

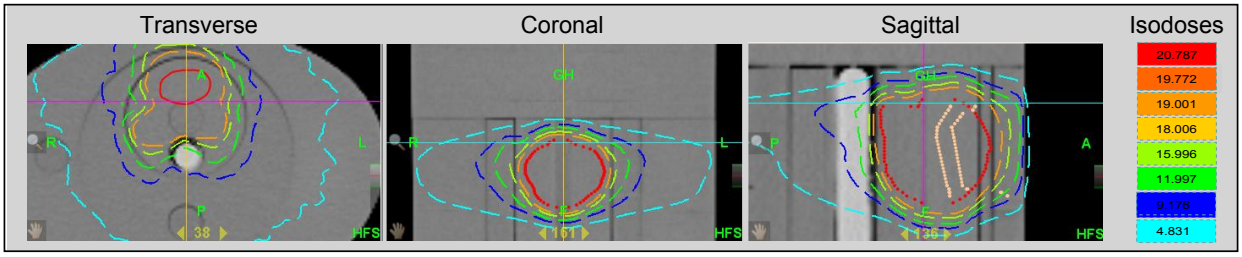

Figure 4.6 Solid probe plan using 2.00 × 2.00 × 2.00 mm^3 dose grid.

anterior point of the rectal wall, the detector readings were acquired by rotating the probe to $\theta = 0°$, 90° and 180°. The measurements were repeated three times and the average taken, and these experimental results were compared to the TPS data. The uncertainty was determined by using Student's t–test.

4.3.2.2 Results

2.00 × 2.00 × 2.00 mm^3 Dose Grid The planned dose prescription was delivered to the phantom and measured by the MO*Skin*™ detectors. Measurements were completed for both the hollow and solid probes with four detectors mounted upon each, and the probes were rotated to $\theta = 0°$, 90° and 180°. The plans can be seen in Figures 4.5 and 4.6.

Figure 4.7 is an example of the change in absorbed dose of each detector over time. It can be seen that the dose rate increases at different times for each detector, depending on the placement of each detector in comparison to the helical delivery of dose.

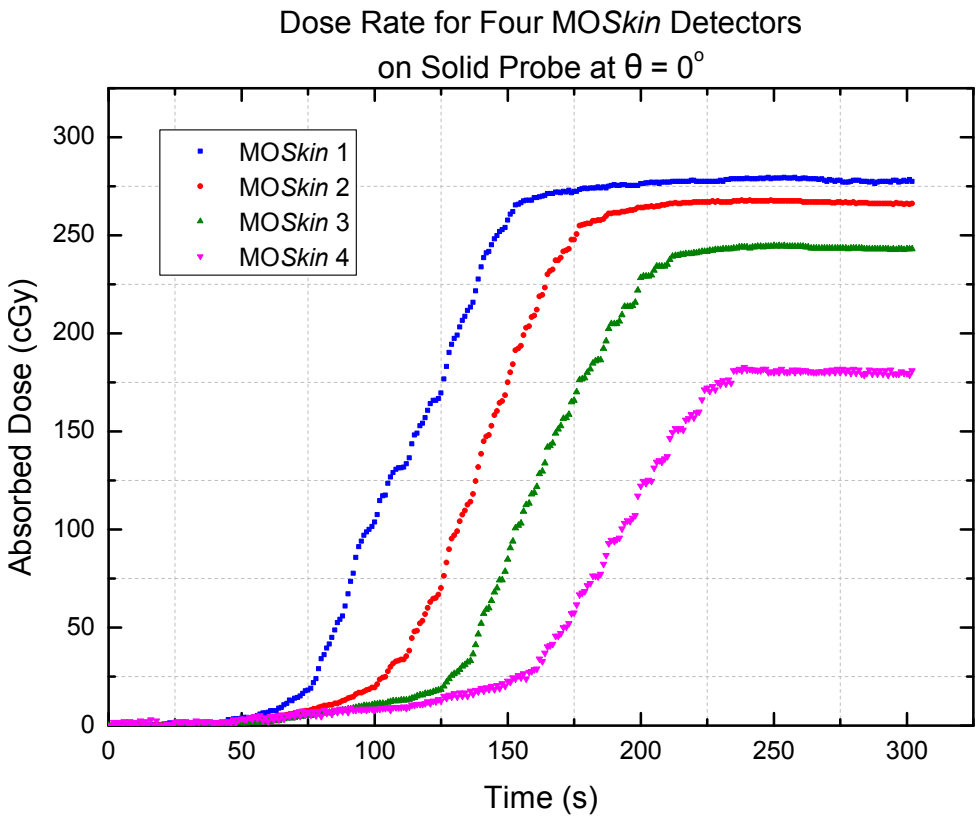

Figure 4.7 Graph of change in absorbed dose measured by each of the MO*Skin*™ detectors over time.

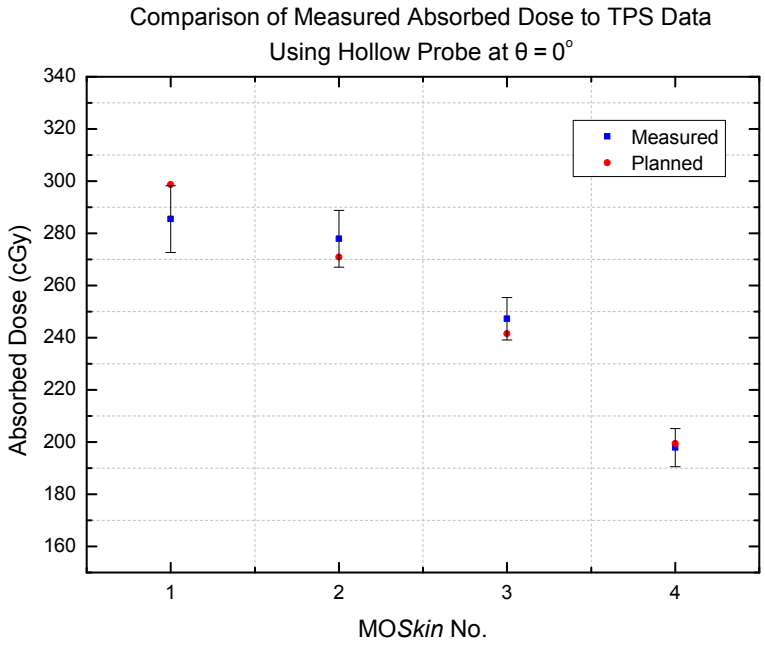

Figure 4.8 Graph of absorbed dose taken from the TPS data in comparison to the dose measured experimentally, using four MO*Skin*™ detectors on the hollow Perspex probe at $\theta = 0°$ for the $2.00 \times 2.00 \times 2.00$ mm^3 dose grid.

The average changes in voltage were then converted to dose (D) per fraction (F) using the calibration factor and are recorded in Tables A.4 to A.9 in Appendix A. The plan data is also included for comparison. The errors in dose measurements were calculated using Student's t–test, with N equal to 3, 2 d.f. and t–value equal to 4.303 for a 95% confidence level. Figures 4.8 to 4.13 demonstrate the discrepancy between the measured dose and the TPS data for the $2.00 \times 2.00 \times 2.00$ mm^3 dose grid. Figures 4.14 to 4.16 show the percentage variation.

The acceptable DTA commonly used for photon beams is $\leq$3 mm [114, 115]. An example of a DTA measurement can be observed in Figure 4.17.

For the $2.00 \times 2.00 \times 2.00$ mm^3 dose grid at $\theta = 0°$, all measurements with the hollow probe fell within the expected $\pm$5%, and all agreed to within experimental error. However, for the solid probe at this angle, all of the measurements were not in agreement with the TPS data (i.e. 10–18% difference) and were well outside error limits. This difference is most likely due to a positional discrepancy; possibly

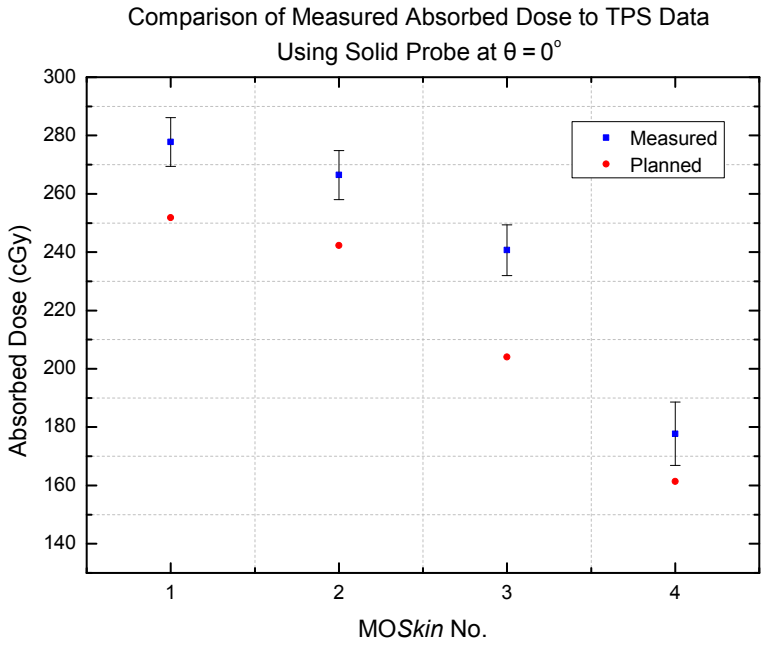

Figure 4.9 Graph of absorbed dose taken from the TPS data in comparison to the dose measured experimentally, using four MO*Skin*™ detectors on the solid Perspex probe at $\theta = 0°$ for the $2.00 \times 2.00 \times 2.00$ mm^3 dose grid.

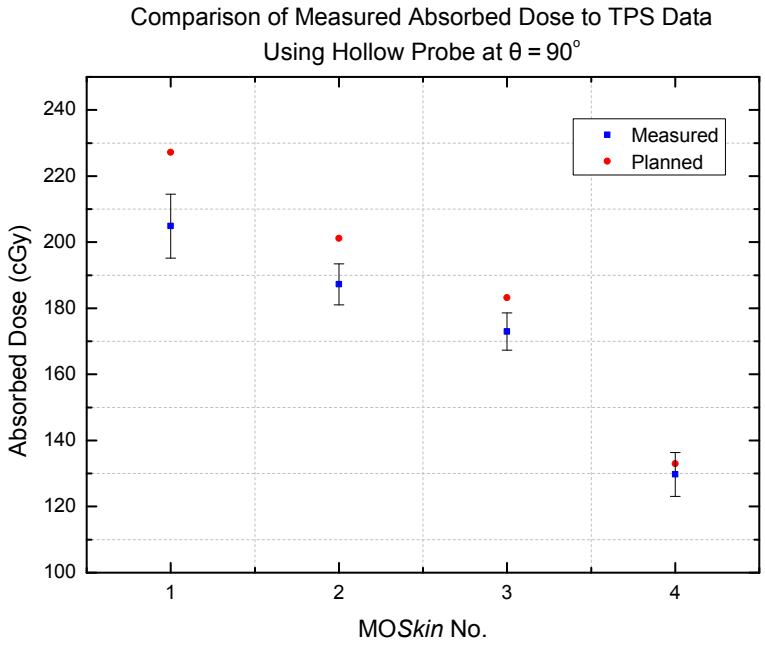

Figure 4.10 Graph of absorbed dose taken from the TPS data in comparison to the dose measured experimentally, using four MO*Skin*™ detectors on the hollow Perspex probe at $\theta = 90°$ for the $2.00 \times 2.00 \times 2.00$ mm^3 dose grid.

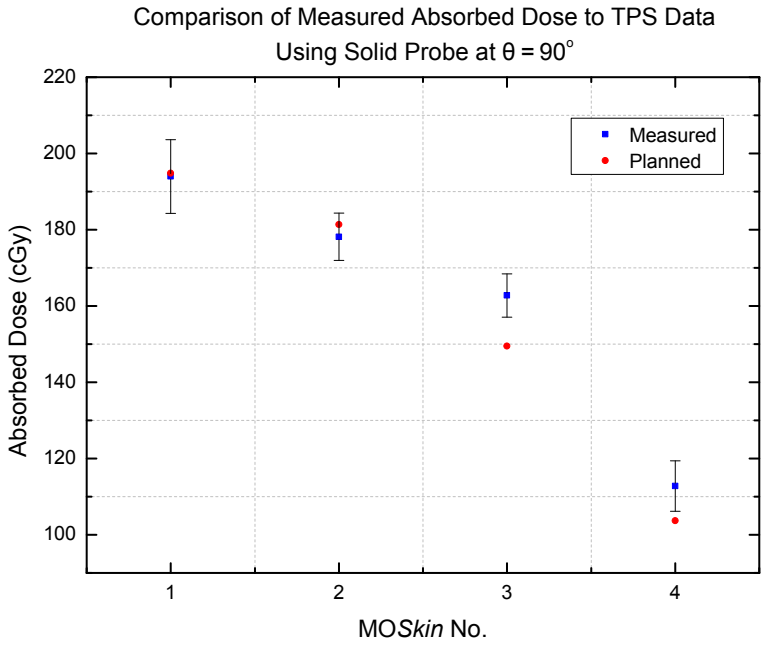

Figure 4.11 Graph of absorbed dose taken from the TPS data in comparison to the dose measured experimentally, using four MO*Skin*™ detectors on the solid Perspex probe at θ = 90° for the 2.00 × 2.00 × 2.00 mm^3 dose grid.

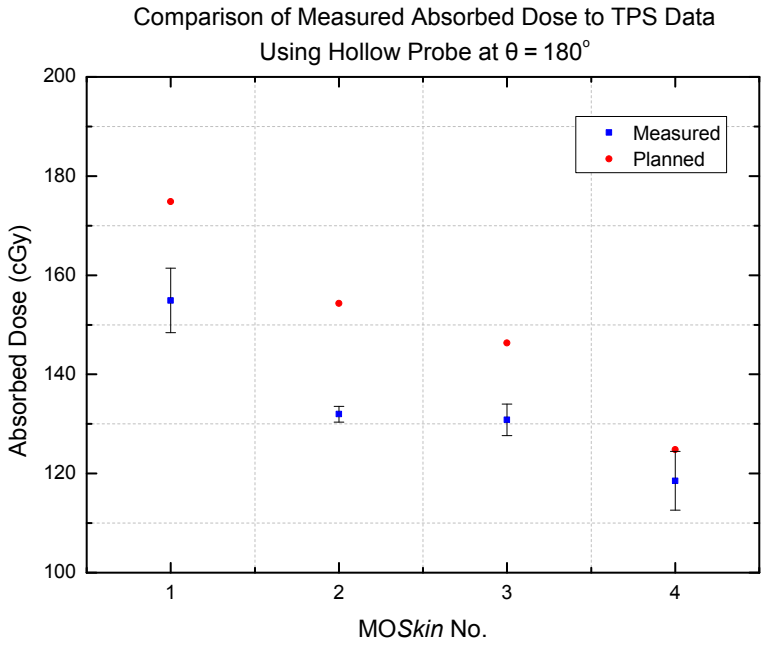

Figure 4.12 Graph of absorbed dose taken from the TPS data in comparison to the dose measured experimentally, using four MO*Skin*™ detectors on the hollow Perspex probe at θ = 180° for the 2.00 × 2.00 × 2.00 mm^3 dose grid.

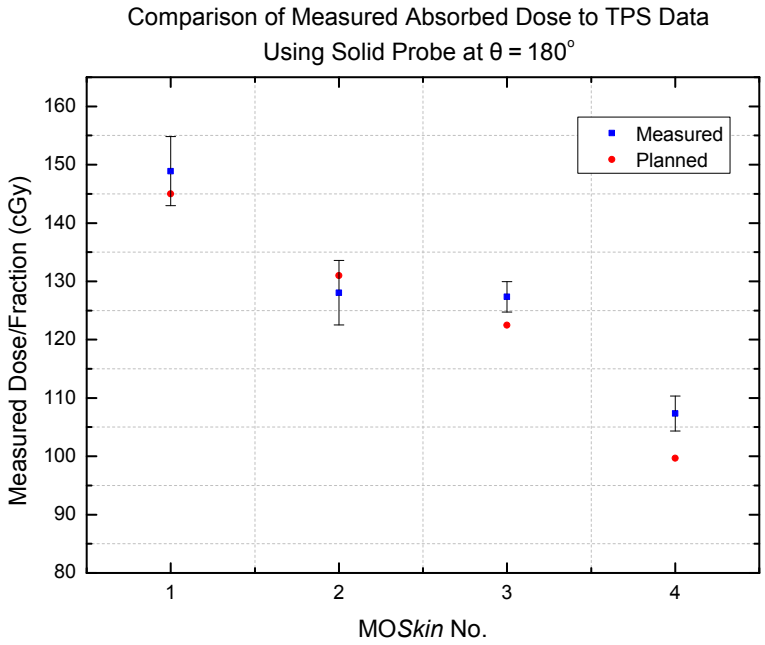

Figure 4.13 Graph of absorbed dose taken from the TPS data in comparison to the dose measured experimentally, using four MO*Skin*™ detectors on the solid Perspex probe at $\theta = 180°$ for the $2.00 \times 2.00 \times 2.00$ mm^3 dose grid.

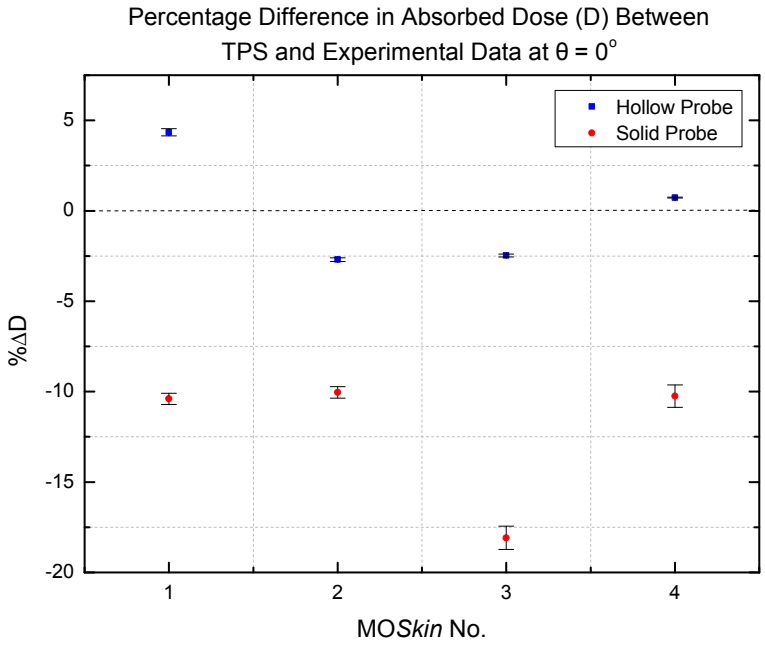

Figure 4.14 Graph of percentage variation of absorbed dose between TPS data and measured dose, using four MO*Skin*™ detectors on solid and hollow Perspex probes at $\theta = 0°$ for the $2.00 \times 2.00 \times 2.00$ mm^3 dose grid.

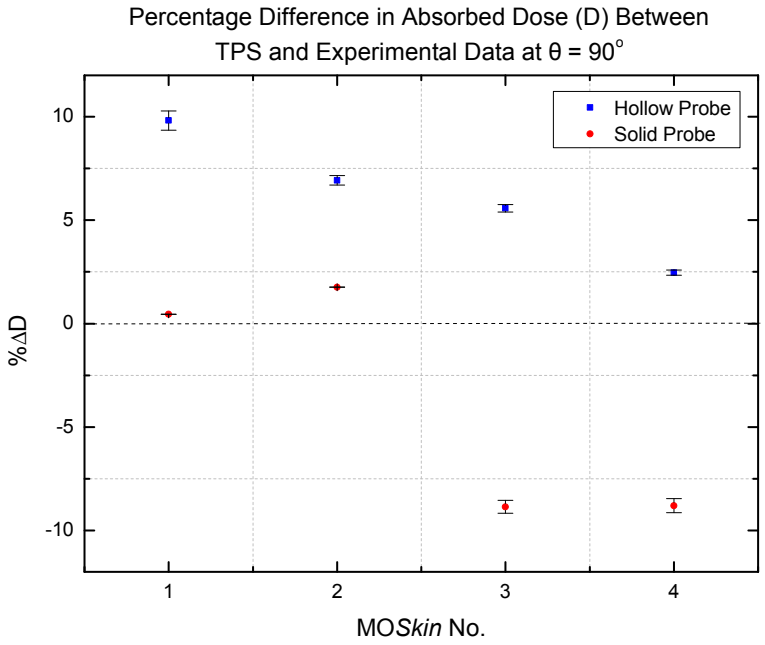

Figure 4.15 Graph of percentage variation of absorbed dose between TPS data and measured dose, using four MO*Skin*™ detectors on solid and hollow Perspex probes at $\theta = 90°$ for the $2.00 \times 2.00 \times 2.00$ mm^3 dose grid.

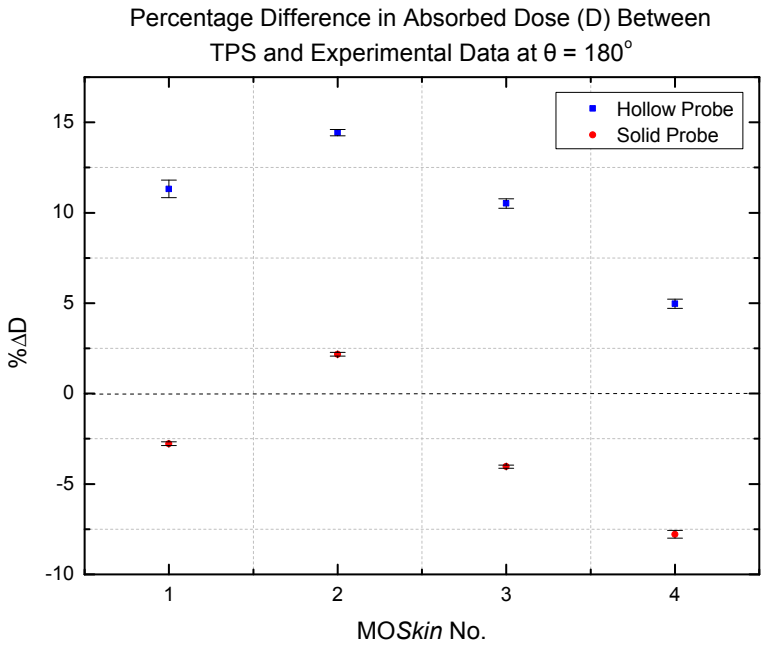

Figure 4.16 Graph of percentage variation of absorbed dose between TPS data and measured dose, using four MO*Skin*™ detectors on solid and hollow Perspex probes at $\theta = 180°$ for the $2.00 \times 2.00 \times 2.00$ mm^3 dose grid.

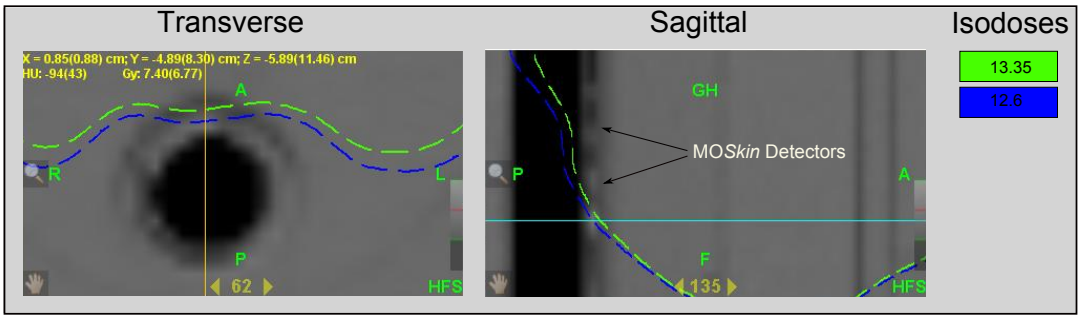

Figure 4.17 A DTA measurement and MO*Skin*™ detectors in high dose gradient region.

a slight rotation of the probe since three out of four detectors show the same percentage discrepancy (approximately 10%). This means that the detectors rotated away from their corresponding isodose line. The DTA values for detectors 1 and 2 were within tolerance at 2.0 mm, however were out of tolerance for detectors 3 and 4 at 3.9 mm.

At θ = 90° using the hollow probe, detector 4 was in agreement with the TPS within error. However the differences of the other three points range from 6.9–9.8%. Of these other points, detector 2 and 3 had an acceptable DTA of 1.9 mm, however detector 1 was outside the acceptable DTA limit at 5.9 mm. Detector 1 and 2 on the solid probe at θ = 90° showed very a good agreement, with both detectors falling within error of the planning data. However, results from detectors 3 and 4 showed approximately a 9% variation from the TPS data. The DTA for detector 3 was 2.7 mm (within tolerance) and for detector 4 was 3.9 mm (outside of tolerance).

Using the hollow probe at θ = 180°, there was not good agreement; with detectors 1–3 varying from TPS by 10.6–14.5%. Only the result from detector 4 was acceptable, which fell inside the error bars. Detector 3 had a DTA of 3.9 mm and detectors 1 and 2 had DTA values of 5.9 mm, which are all outside of the acceptable range. The solid probe demonstrated a better agreement than the hollow probe at this angle. Detectors 1–3 were within 5%, with 1 and 2 agreeing with the TPS to within error. However, detector 4 had a 7.7% deviation from the TPS with a DTA

outside tolerance of 3.9 mm.

Considering the anterior rectal wall alone, altogether 50% of measured doses showed agreement to within $\pm 5\%$ of the TPS doses. However, if the acceptable DTA measurements were taken into account, there was a total of 75% agreement. The results from the other locations (posterior and side walls) are not as significant due to the lower doses as these points.

The size of the dose grid was $2.00 \times 2.00 \times 2.00$ mm^3 and the implication of this was that the position needed for measurement may have been in between two different $2.00 \times 2.00 \times 2.00$ mm^3 voxels on the plan, resulting in two different doses. There was also difficulty in visualising where the inner edge of the hollow probe was on the CT image. This edge was used as a base to measure anteriorly to where the detector was positioned on the probe. The solid probe was much easier to visualise on the scan.

Any deviation that the more inferiorly placed detectors demonstrated may have been due to the slight anterior angling of the rectal volume on the plan compared to the phantom's rectal wall. As mentioned before, a patient's plan was adapted for the phantom plans so that the contours for the critical organs could be used. The contour of the rectum was curved whilst the rectal wall was perfectly straight, as can be observed in Figure 4.18. The detectors were placed on the anterior side of the probe, hence, they may be angled away from their corresponding isodose line.

$1.37 \times 1.37 \times 2.00$ mm^3 Dose Grid To try to improve the accuracy of the dose reading from the TPS, a fine dose grid calculation was performed with the grid reducing from $2.00 \times 2.00 \times 2.00$ mm^3 to $1.37 \times 1.37 \times 2.00$ mm^3. Both solid and hollow probe plans were re–optimised to allow for the best possible plan to be created in each circumstance, which is ultimately what is desired for a patient's treatment plan. Measurements were performed again due to the re–scanning needed.

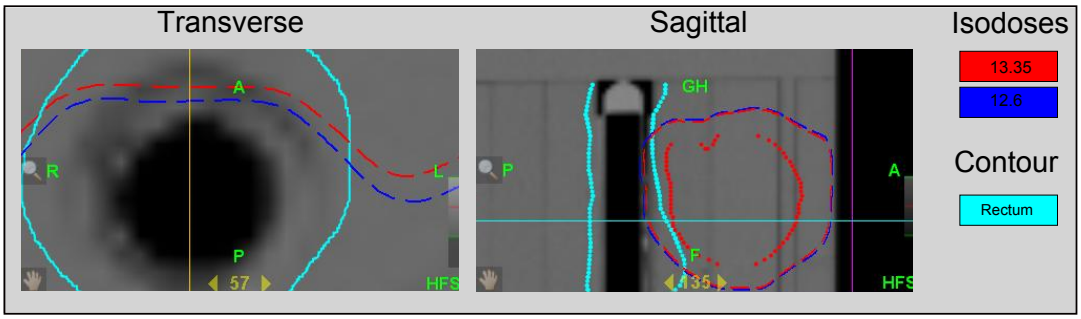

Figure 4.18 Difference in angle between rectum contour and probe.

The results are shown in Tables A.10 to A.15 in the Appendix. Figures 4.19 to 4.24 demonstrate the discrepancy between the measured dose and the TPS data using the fine dose grid calculation and Figures 4.25 to 4.27 show the percentage variation.

At $\theta = 0°$ using the hollow probe, detector 1 agreed with the planning data within error and detector 2 was within 3% of the TPS. Detector 3 and 4 demonstrated a bit more deviation than was expected with 5.5 and 6.0% deviation respectively; however, their DTA values were acceptable at 1.4 mm. The solid probe results showed a great improvement in correlation between TPS and measurement when compared to the previous dose grid measurements, with three detectors agreeing with the TPS within experimental error. Although the uncertainty for detector 1 was quite large, it still only demonstrated a difference of 3.1% from the expected value. Detector 4 showed a variation of 12.3% from the TPS data and its DTA was not acceptable at 4.1 mm.

For $\theta = 90°$ the detectors on the hollow probe measured results within good agreement. All results were within 4% of the expected and detectors 1 and 2 were within error. For the solid probe detectors 1, 2 and 3 agreed within uncertainty to the planned result. Detector 4 showed a large variation of 14.4% and its DTA was 4.1 mm (outside tolerance). Both the solid and hollow probe showed a better agreement

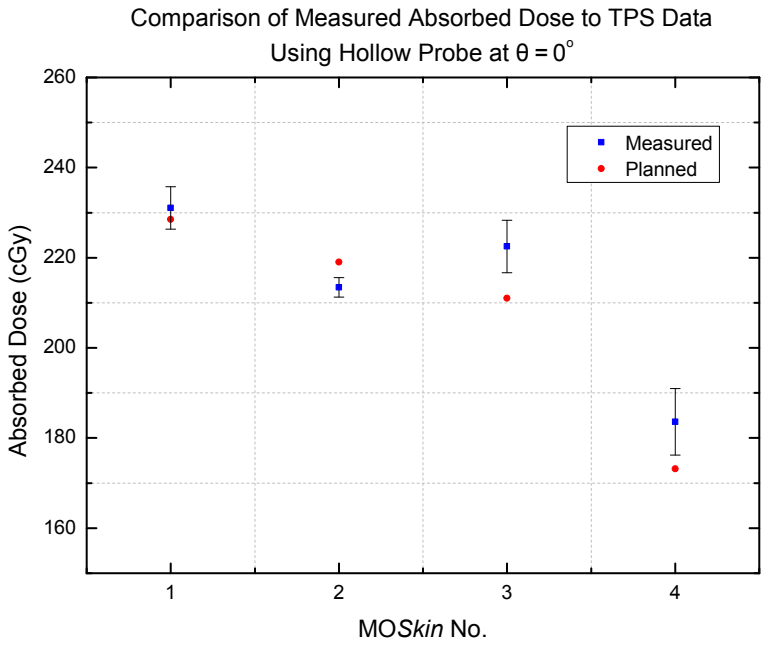

Figure 4.19 Graph of absorbed dose taken from the TPS data in comparison to the dose measured experimentally, using four MO*Skin*™ detectors on the hollow Perspex probe at $\theta = 0°$ for the $1.37 \times 1.37 \times 2.00$ mm^3 dose grid.

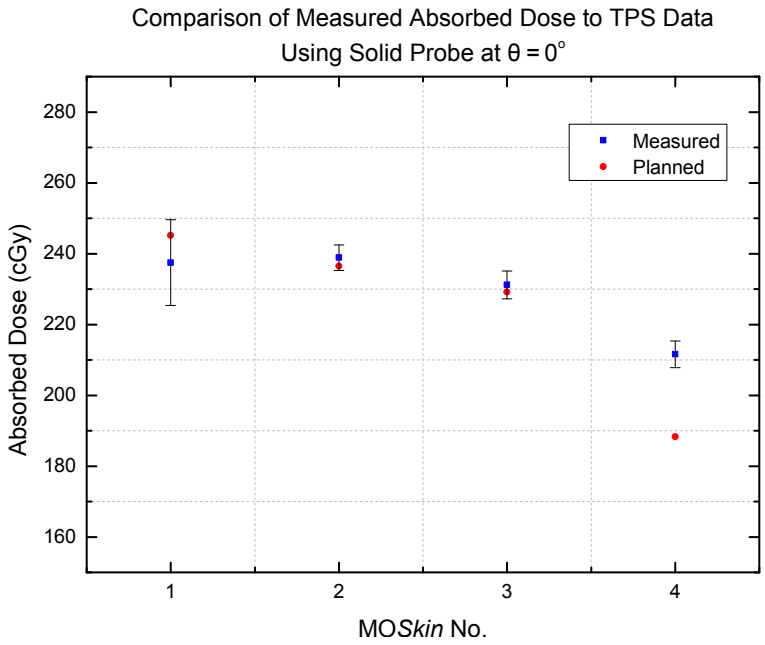

Figure 4.20 Graph of absorbed dose taken from the TPS data in comparison to the dose measured experimentally, using four MO*Skin*™ detectors on the solid Perspex probe at $\theta = 0°$ for the $1.37 \times 1.37 \times 2.00$ mm^3 dose grid.

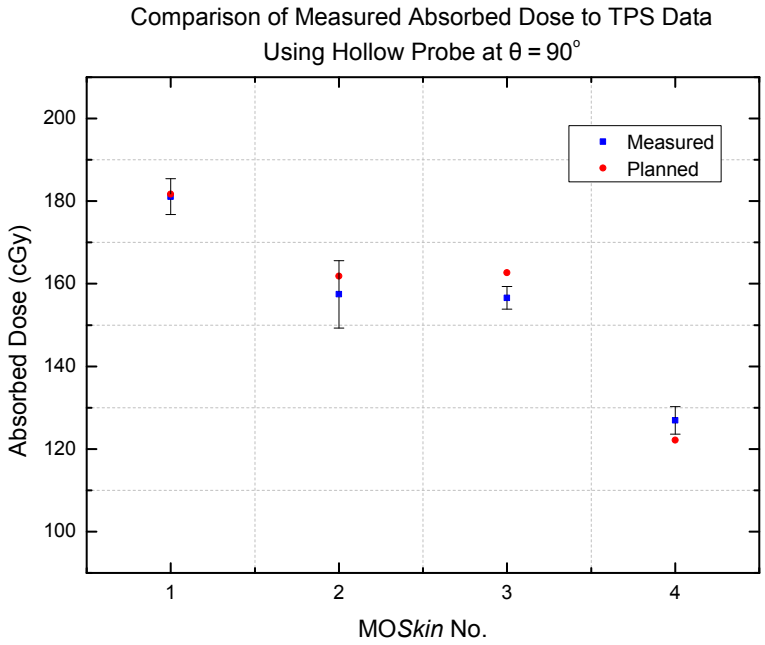

Figure 4.21 Graph of absorbed dose taken from the TPS data in comparison to the dose measured experimentally, using four MO*Skin*™ detectors on the hollow Perspex probe at $\theta = 90°$ for the $1.37 \times 1.37 \times 2.00$ mm^3 dose grid.

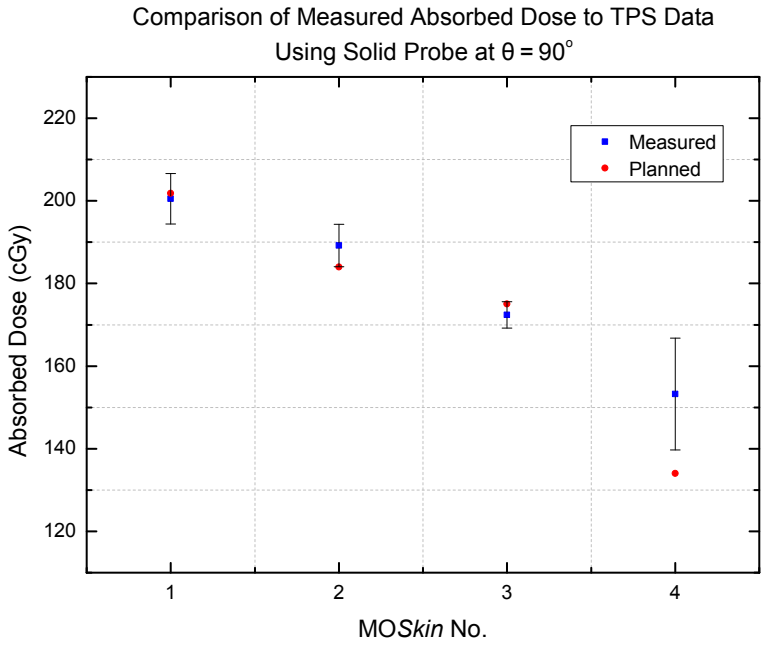

Figure 4.22 Graph of absorbed dose taken from the TPS data in comparison to the dose measured experimentally, using four MO*Skin*™ detectors on the solid Perspex probe at $\theta = 90°$ for the $1.37 \times 1.37 \times 2.00$ mm^3 dose grid.

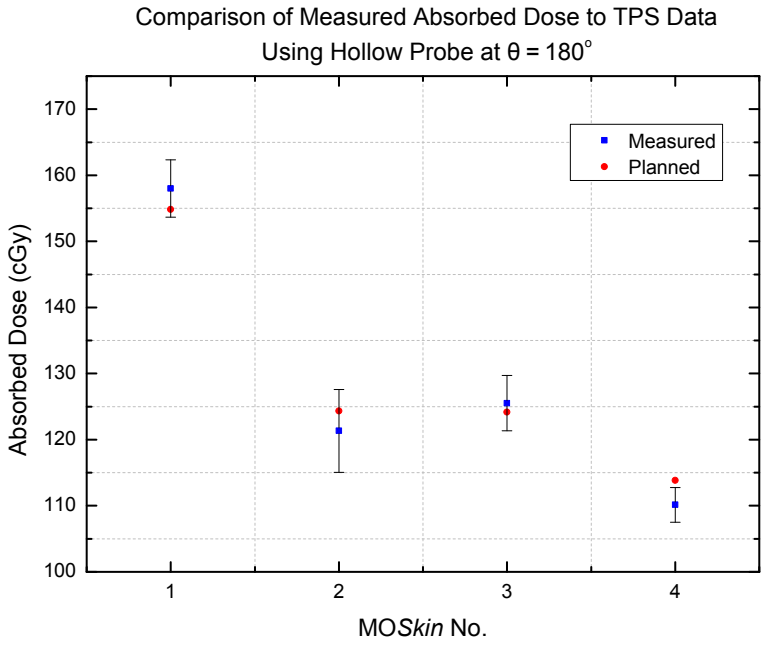

Figure 4.23 Graph of absorbed dose taken from the TPS data in comparison to the dose measured experimentally, using four MO*Skin*™ detectors on the hollow Perspex probe at θ = 180° for the 1.37 × 1.37 × 2.00 mm^3 dose grid.

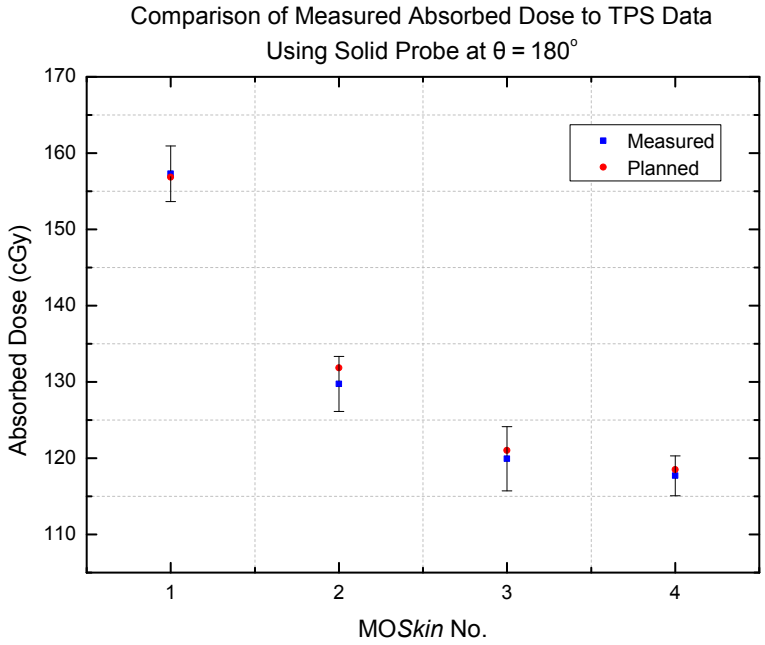

Figure 4.24 Graph of absorbed dose taken from the TPS data in comparison to the dose measured experimentally, using four MO*Skin*™ detectors on the solid Perspex probe at θ = 180° for the 1.37 × 1.37 × 2.00 mm^3 dose grid.

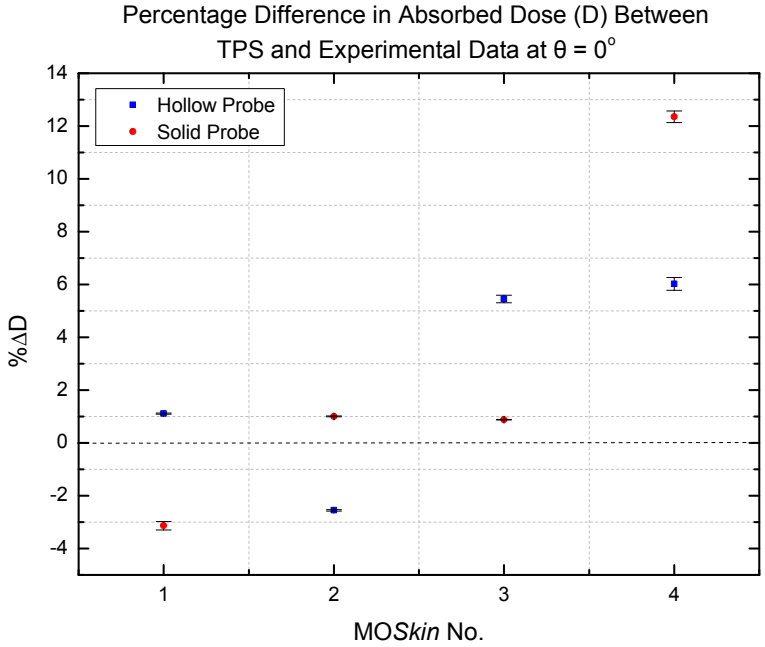

Figure 4.25 Graph of percentage variation of absorbed dose between TPS data and measured dose, using four MO*Skin*™ detectors on solid and hollow Perspex probes at $\theta = 0°$ for the $1.37 \times 1.37 \times 2.00$ mm^3 dose grid.

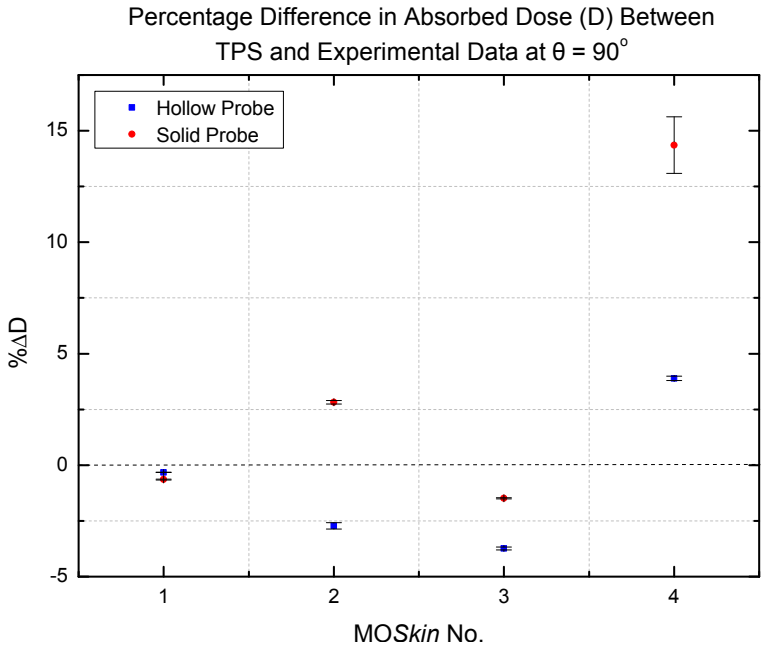

Figure 4.26 Graph of percentage variation of absorbed dose between TPS data and measured dose, using four MO*Skin*™ detectors on solid and hollow Perspex probes at $\theta = 90°$ for the $1.37 \times 1.37 \times 2.00$ mm^3 dose grid.

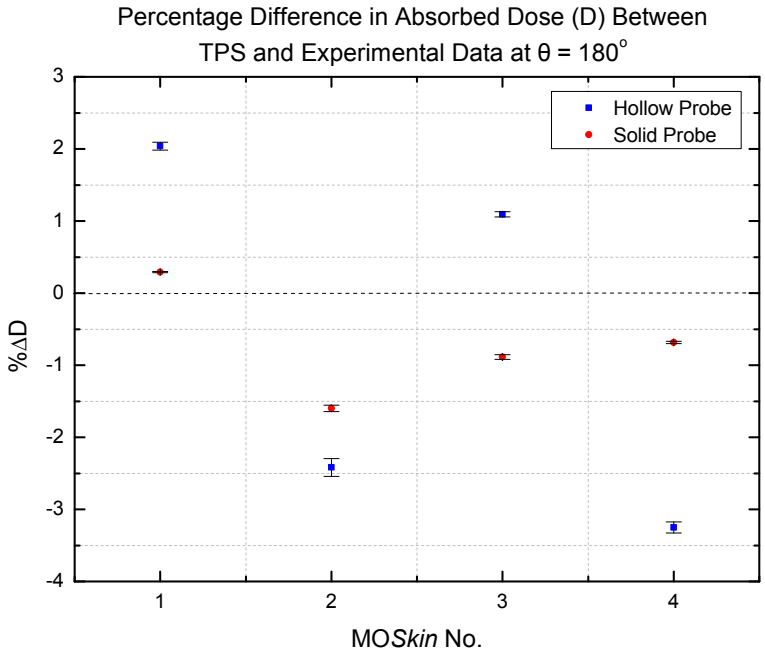

Figure 4.27 Graph of percentage variation of absorbed dose between TPS data and measured dose, using four MO*Skin*™ detectors on solid and hollow Perspex probes at $\theta = 180°$ for the $1.37 \times 1.37 \times 2.00$ mm^3 dose grid.

to the TPS than the previous dose grid.

For $\theta = 180°$, all detectors on the hollow probe demonstrated results within 3.3% of the TPS data, with detectors 1–3 being within error bounds. Again, there was much improvement from the 2 mm^3 dose grid. The detectors on the solid probe showed very good agreement with all results being within the error bounds.

At the anterior rectal wall, considering both solid and hollow probe results, 62.5% of detectors measured dose to within ±5% of the TPS. DTA results that were within tolerance increased agreement to 87.5%, which was an improvement on the normal dose grid.

Considering all measurements at all rectal wall positions, for the fine dose grid, twenty out of twenty–four detectors (83%) measured dose to within ±5% of the TPS calculated dose, compared to eleven out of twenty–four (46%) in the normal

Dose Grid (mm^3)	Probe Type	Angle (θ)	Detector	DTA (mm)
$2.00 \times 2.00 \times 2.00$	Hollow	90°	1	5.9
			2	1.9
			3	1.9
		180°	1	5.9
			2	5.9
			3	3.9
	Solid	0°	1	2.0
			2	2.0
			3	3.9
			4	3.9
		90°	3	2.7
			4	3.9
		180°	4	3.9
$1.37 \times 1.37 \times 2.00$	Hollow	0°	3	1.4
			4	1.4
	Solid	0°	4	4.1
		90°	4	4.1

Table 4.2
Table of Distance–to–Agreement (DTA) values for TomoTherapy® experiment utilising single MO*Skin*™ detectors.

dose grid case. After consideration of DTA values (Table 4.2), further agreement was observed. Two out of four DTA values were within the tolerance of 3 mm for the fine dose grid, meaning out of all twenty–four measurements for this grid, there were only three measurements that did not correlate to the TPS data (87.5% agreement). This was compared to five out of thirteen DTA values for the normal dose grid being acceptable, which meant eight out of all twenty–four measurements for this dose grid did not correlate to the expected (66.7% agreement). Both hollow and solid probes had a similar number in terms of how many measurements had DTA values within the tolerance.

Discrepancies in the hollow probe for either dose grid were believed to be due to the inhomogeneity in the dose distribution resulting from the air cavity. Image artefacts were not thought to affect these readings as there were no large perturbations in CT number around the probe position and no artefacts were visible

by qualitative visualisation of the CT images.

Like the brachytherapy case, TPS 'error bars' were determined as well as experimental error by taking dose measurements from adjacent voxels. Again, these were not statistical error bars but were found by taking the largest deviations from all points and plotting these deviations as the uncertainty in TPS data. For example, for the readings taken at $\theta = 0°$, the TPS data point used to compare the experimental results with, that corresponded to the position of the measured dose was located just on the anterior edge of the probe (i.e. where the detector was actually located) on the CT image. However, this could be difficult to visualise on the scan due to the contrast and resolution of the display, therefore a point anterior to this point was also taken. To account for points that may seem to be in–between two voxels in the left/right direction, points were taken left and right of the point. The superior/inferior direction was also accounted for by taking a point on the slice superior and inferior, in the same anterior/posterior and left/right positions as the main data point on the original slice. Then anterior/posterior and left/right points were taken on these slices, as on the original slice. The largest positive and negative deviations were used demonstrated the large spread of dose around the data point. Figure 4.28 demonstrates this.

The TPS error bars were quite large; varying up to 30 cGy from the planned data points corresponding to the measured data points for this dose grid. By observing these steep dose gradients, it can be seen why such a small change in position can lead to a large change in dose, which may provide an explanation for variation between experimental results and the TPS.

All results depended on the plan used due to the differences in position that the detectors can be placed in the high dose gradient regions. Figure 4.1 demonstrated the approximate position of the rectum in this high dose gradient region. The results demonstrated that even with a fine dose grid, the reliance on positional accuracy in a high dose gradient region still has a significant effect on the results.

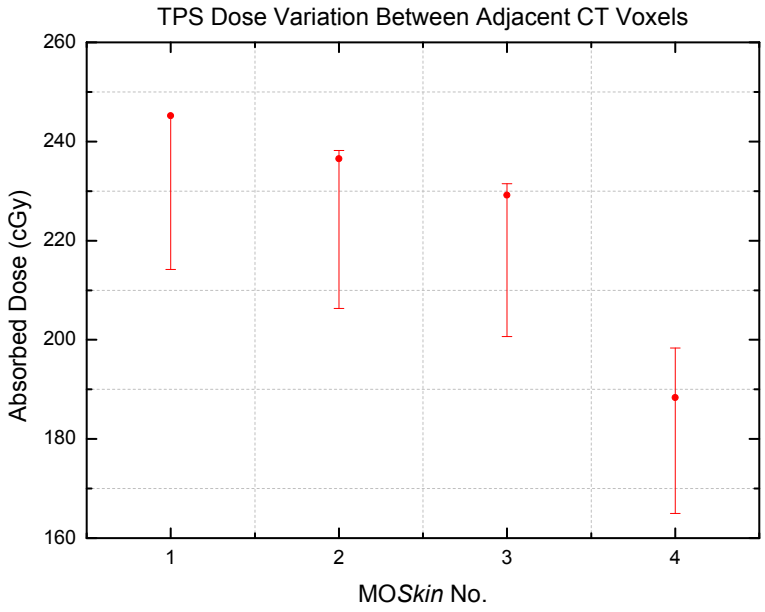

Figure 4.28 Graph demonstrating TomoTherapy® TPS data uncertainty due to large varaitions in dose between adjacent CT voxels.

The difference in dose across a 1.37 × 1.37 × 2.00 mm^3 voxel can still be quite large when compared to the size of the sensitive volume of a MO*Skin*™ detector, with its gate oxide thickness measuring 0.55 μm [97] and the thickness of the entire detector measuring only 0.4 mm [104].

Even though the plans were re–optimised for each probe type, the two plans could still be compared in terms of which plan could deliver a lower dose to the rectum when optimised for its own conditions. For the normal dose grid all measurements of absorbed dose for the solid probe were lower than the hollow probe by a range of 2.7–15.0%. For the fine dose grid the opposite can be observed, with all bar one detector on the solid probe showing a higher dose than those on the hollow probe by a range of 1.3–13.2%. As can be seen here; different plans would result in a different dose distribution. Hence the results demonstrate that the solid probe spared the rectum better in the normal dose grid case and the hollow probe when employing the fine dose grid calculation.

4.3.2.3 Discussion

It can be concluded that the fine dose grid calculation did indeed improve the measurements. The fine dose grid provided a more accurate method for measuring absorbed dose from the TPS than the normal dose grid. Then, looking at the results for the fine dose grid, it was not clear which probe was better as there were a number of factors to consider. The hollow probe was better as it reduced the dose to the rectum. However, as this changed between dose grids, it may indicate that it was not caused by a physical characteristic of the probe, and hence may change between plans.

Another aspect to consider was that the plan using the solid probe allowed the edge of the probe to be more easily visualised on the CT scan, using the resolution available. This aspect therefore also improved accuracy. Both solid and hollow probes performed equally well when using the fine dose grid in terms of deviation from the TPS data. Therefore, if the ease with which the solid probe could be seen on the CT scan is the dominant factor (because spatial positioning of the detector can be more clearly determined on CT), then this probe combined with MO*Skin*™ detectors and the use of a fine dose grid calculation would be more accurate for rectal wall dose measurements in prostate treatment using TomoTherapy®.

Discrepancies were partly attributed to positional uncertainty in the very high dose gradient region at the anterior rectal wall. This could be investigated with fiducial markers to improve image–guidance. Angular dependence should also be investigated by the use of dual MO*Skin*™ detectors.

The fact that the treatment used in this experiment was a TomoTherapy® boost, to be used in conjunction with IMRT, means that the patient may only be required to have the probe inserted for the boost treatment. It is particularly important to verify the dose in the boost due the large fraction sizes (approximately

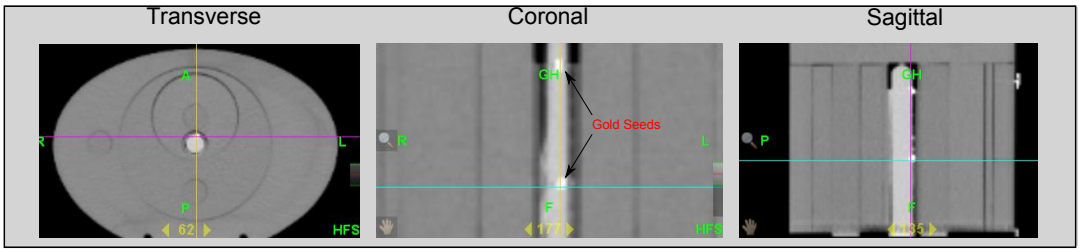

Figure 4.29 CT scan of solid probe with gold seeds imbedded in surface.

10.5 Gy per fraction), when compared to the smaller fraction sizes of the IMRT (approximately 1.8–2 Gy per fraction). The discomfit of the probe would therefore only need to be tolerated for two fractions instead of potentially twenty–three or more, making the treatment easier on the patient.

4.3.3 Measurements with Inclusion of Gold Seed Fiducial Markers

4.3.3.1 Methodology

The method utilised so far for checking probe rotation was to draw markings on the probe that would then be aligned to the room lasers. After treatment the alignment was checked again to ensure the probe had not rotated. To attempt to further improve the detector positional reproducibility, fiducial markers were attached to the probe. Since the solid probe was verified to be the best choice for rectal dose measurements in a TomoTherapy® boost, the gold seeds were added to this probe to determine whether this further improved positional accuracy. Holes were therefore drilled into the solid probe, both 1.5 cm superior and 1.5 cm inferior to the detectors. In these holes, 3 mm long gold seeds were placed, running in the superior/inferior direction, flat to the probe's surface.

At this time a new CT scanner was available and hence a 1 mm slice thickness for the planning CT scan could be utilised. A plan was created, and as previously, the dose read out at the positions of the four detectors. The dose calculation grid used was $1.37 \times 1.37 \times 1.00\,\mathrm{mm}^3$. Another advantage of the fiducial markers was that the

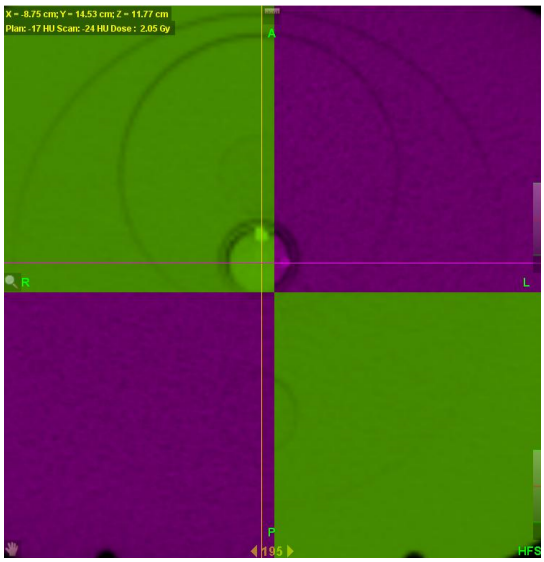

Figure 4.30 Registerd KVCT (green) and MVCT (purple) images with MO*Skin*™ detectors and gold seeds positioned at $\theta = 90°$.

MVCT scans could be used for the pre-treatment scans. These were registered to the KVCT image before treatment (Figures 4.30 and 4.31) and the gold seeds aligned between the two images.

4.3.3.2 Results

The results can be seen in Tables A.16 to A.17 in the Appendix. Figures 4.32 to 4.34 demonstrate the discrepancy between the measured and planned doses. DTA measurements were completed and are displayed in Table 4.3.

For $\theta = 0°$, detector 1 was within $\pm 5\%$ of the planned doses, at 4.6%. For the remaining measurements at this angle, the doses were 8.1–13.9% higher than those of the TPS. However, their DTA measurements were all within the 3 mm tolerance at 2.2 mm, 1.4 mm and 1.4 mm for detectors 2, 3 and 4 respectively.

For $\theta = 90°$, detector 3 varied from the planned data by 2.8%. All other detectors measured doses that were 6.6–10.9% lower than the TPS doses. Detector 2 had a DTA measurement of 2.8 mm, whereas detector 1 and 4 had DTA values of

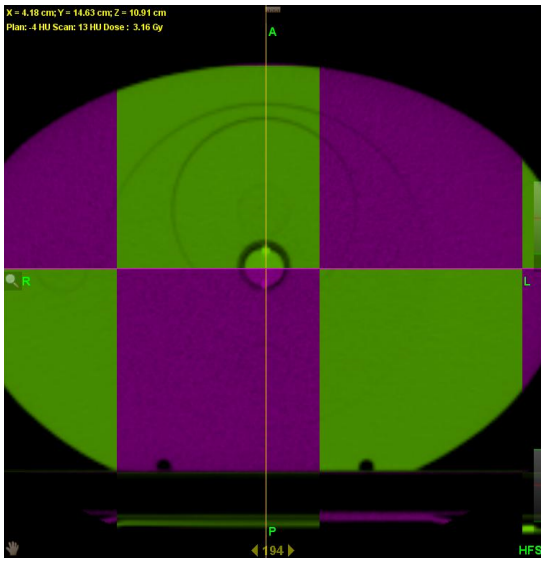

Figure 4.31 Registerd KVCT (green) and MVCT (purple) images with MO*Skin*™ detectors and gold seeds positioned at $\theta = 180°$.

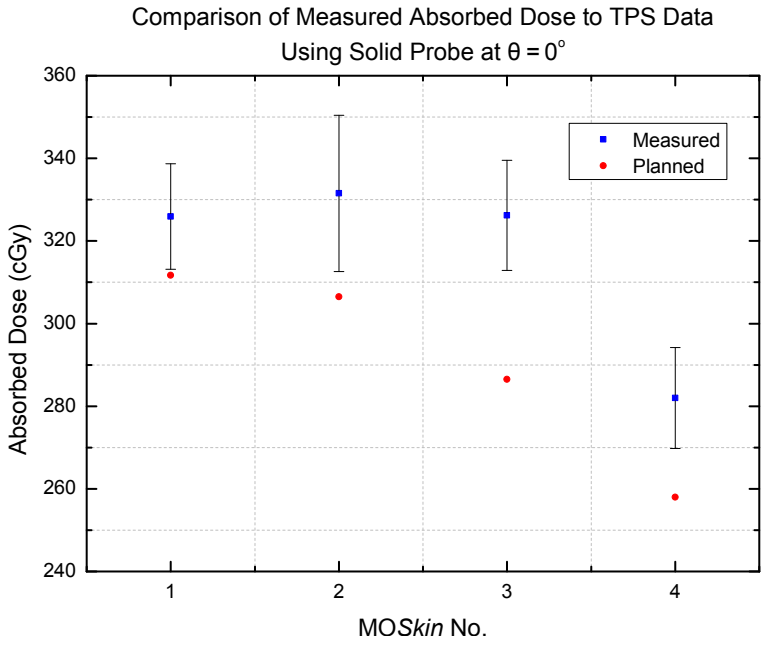

Figure 4.32 Graph of absorbed dose taken from the TPS data in comparison to the dose measured experimentally, using four MO*Skin*™ detectors on the solid Perspex probe at $\theta = 0°$ for the $1.37 \times 1.37 \times 1.00$ mm^3 dose grid. Fiducial markers were attached to the probe.

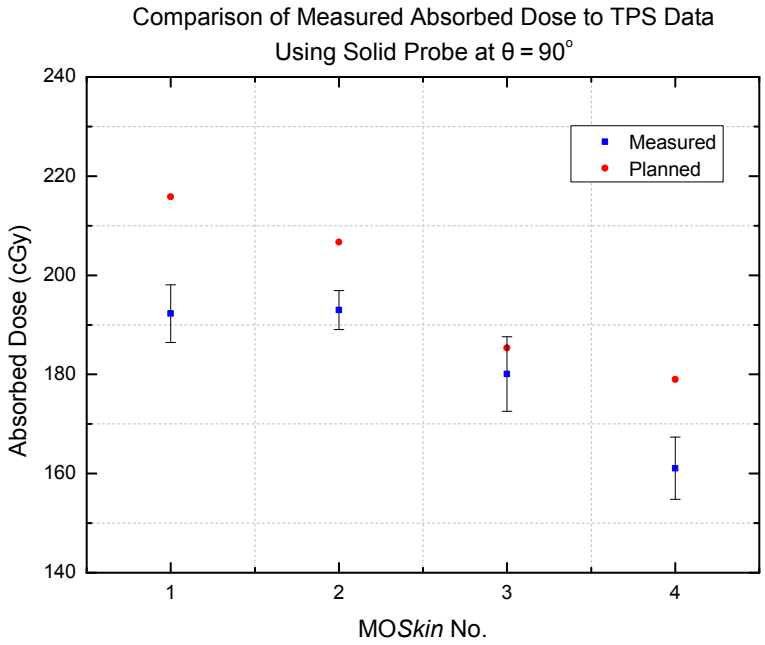

Figure 4.33 Graph of absorbed dose taken from the TPS data in comparison to the dose measured experimentally, using four MO*Skin*™ detectors on the solid Perspex probe at $\theta = 90°$ for the $1.37 \times 1.37 \times 1.00$ mm^3 dose grid. Fiducial markers were attached to the probe.

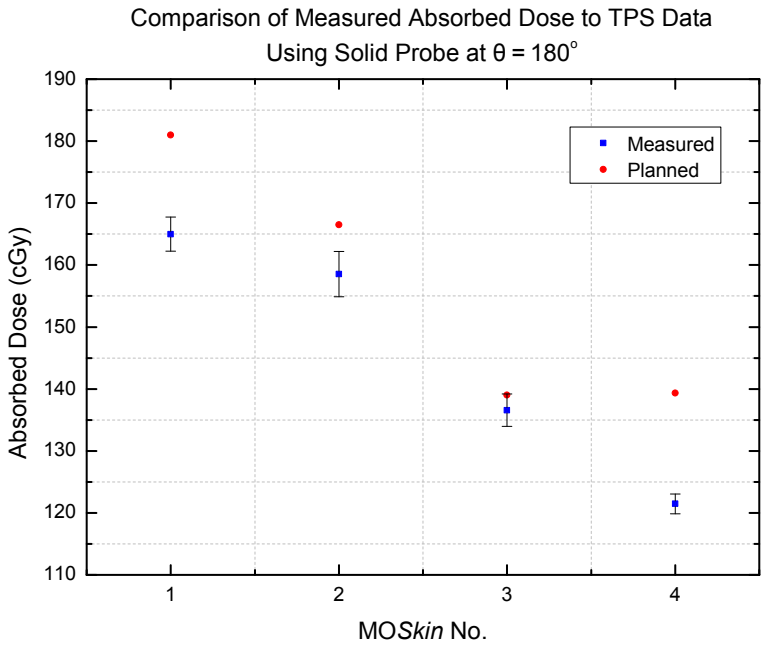

Figure 4.34 Graph of absorbed dose taken from the TPS data in comparison to the dose measured experimentally, using four MO*Skin*™ detectors on the solid Perspex probe at $\theta = 180°$ for the $1.37 \times 1.37 \times 1.00$ mm^3 dose grid. Fiducial markers were attached to the probe.

Angle (θ)	Detector	DTA (mm)
0°	2	2.2
	3	1.4
	4	1.4
90°	1	4.1
	2	2.8
	4	3.6
180°	1	4.1
	4	4.1

Table 4.3
Table of Distance–to–Agreement (DTA) values for TomoTherapy® experiment utilising fiducial markers on probe.

4.1 mm and 3.6 mm respectively.

At θ = 180°, detector 2 measured a dose that differed from the TPS by 4.8% and detector 3 differed by 1.7%. Detectors 1 and 4 differed by 8.8% and 12.8% from the planned doses, respectively, with a DTA measurement of 4.1 mm for both detecttor positions.

For the anterior rectal wall, there was a 25% agreement between measured and planned doses, however all DTA measurements were within tolerance, increasing the agreement to 100% at this location. For total measurements at all rectal wall locations, the results showed that 33.3% of measurements fell within ±5% of the planned doses. However, four out of eight DTA values were within tolerance. This indicates that eight out of twelve (66.7%) measurements in total, for this part of the experiment, corresponded to the planned doses.

It was demonstrated that the fiducial markers did not improve the results. If only considering the anterior rectal wall because of the higher doses at this point, and accounting for DTA measurements that were within tolerance as well; then it could be said that the fiducial markers did improve the agreement between measured and TPS doses (100% agreement). However, from a clinical point of view, having

an immediate agreement during treatment is more beneficial than needing to further analyse results with DTA measurements.

The plan used was a new plan than previously used, and a steeper dose gradient was observed in the area that the detectors were positioned in. These measurements show that this steep dose gradient is problematic when taking point dose measurements. Potentially a plan with a shallower dose gradient may have provided a closer agreement between the detector readings and TPS doses. The larger number of discrepancies observed in this experiment was believed to be due to the fact that image–guidance was completed by aligning the fiducial markers between the treatment CT scan and planning CT scan, rather than by the actual detectors, which had been the previous method used. For correct verification of the position of the detectors themselves, fiducial markers would need to be attached to the actual detectors rather than the probe. However, this would not be possible as the markers would affect the dose measured by the detectors. A more sophisticated probe design could instead assist in improving positional accuracy of the detectors.

4.3.3.3 Discussion

From these results, it can be seen that as the gold seeds did not improve the positional reproducibility of the detectors, the original method of marking the probe in line with the sensitive volumes of the detectors was acceptable. Image–guidance should attempt to match to the detectors to account for slight positional shifts. Hence, for the remaining experiments, fiducial markers will not be utilised.

4.4 TomoTherapy® Measurements with Dual MO*Skin*™ Detectors and IMRT Phantom

The fiducial measurements with single MO*Skin*™ detectors demonstrated that the results thus far have not been satisfactory, therefore further investigation was completed in the TomoTherapy® measurements. To improve the accuracy of measurements at

the expense of having larger detectors, as in the brachytherapy case; the measurements were repeated using dual MO*Skin*™ detectors, the properties of which were previously discussed.

4.4.1 Dual MO*Skin*™ Detector Calibration

4.4.1.1 Methodology

The MO*Skin*™ detectors were calibrated using the TomoTherapy® unit at approximately 6 MV [113] using a static, 5 $\times$ 40 cm^2 field at 85 cm Source–to–Surface Distance (SSD). The detectors were placed at a depth of 1.5 cm of solid water and voltage readings acquired. The readings were compared to CC13 ionisation chamber dose measurements that were also taken at 1.5 cm depth of solid water to determine the calibration factor. Each detector was calibrated facing both upwards and then downwards, so that an average calibration factor was determined for each detector orientation. An average calibration factor was then found between the upwards averaged calibration factor and downwards average calibration factor.

4.4.1.2 Results

The average calibration factors were determined to be 2.57 $\pm$ 0.06 mV/cGy for the upwards–facing detectors, and 2.36 $\pm$ 0.04 mV/cGy for the downwards–facing detectors. An average calibration factor between the upwards and downwards values was therefore determined to be 2.47 $\pm$ 0.07 mV/cGy, which was applied to all dual MO*Skin*™ detector measurements for this experiment.

4.4.2 Treatment Delivery

4.4.2.1 Methodology

The IMRT phantom was again utilised for treatment delivery. The solid probe, having already been determined to be the preferred probe of the two; was utilised for this experiment. Dual MO*Skin*™ detectors were attached to the solid probe. The read–out unit was modified to support five dual MO*Skin*™ detectors. The dose grid used

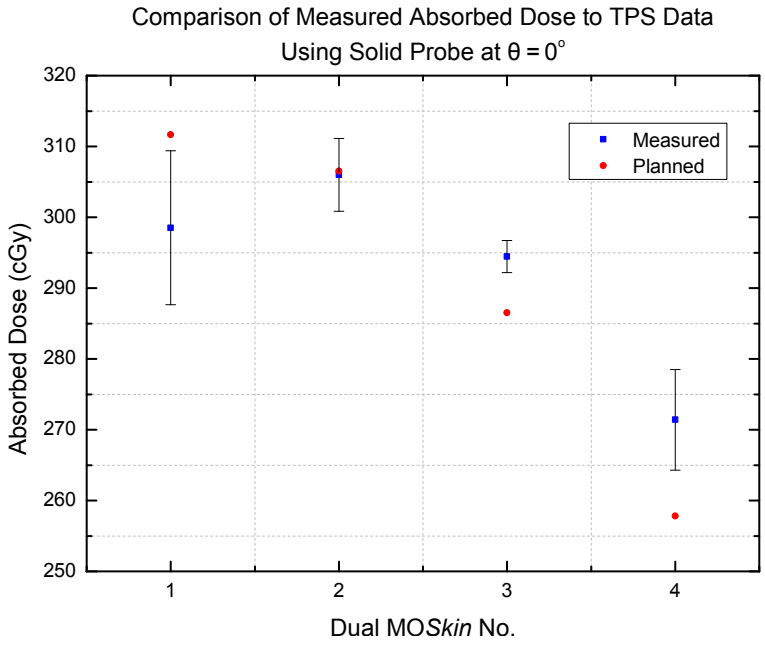

Figure 4.35 Graph of absorbed dose taken from the TPS data in comparison to the dose measured experimentally, using four dual MO*Skin*™ detectors on solid probe at $\theta = 0°$ for the $1.37 \times 1.37 \times 1.00$ mm^3 dose grid.

was the fine dose grid with a scan slice thickness of 1 mm. The probe was rotated to $\theta = 0°$, $90°$ and $180°$, dose measurements taken at these points and compared to the planned doses.

4.4.2.2 Results

The measured doses were compared to the planned doses and are displayed from Figure 4.35 to Figure 4.37 and in Appendix A in Table A.19 to Table A.21. The average error was less than 3% of the measured doses. Dual detector 1 was believed to be slightly unstable, which was demonstrated by its larger error. The detector may have been affected by abrasion.

At $\theta = 0°$, dual detector 1 deviated by 4.2% from the TPS data, which was within tolerance. Dual detectors 2 and 3 also agreed with the TPS, deviating from the planned data by only 0.3% and 2.8% respectively. The result from dual detector 4 differed from the TPS by 5.3%; however, its DTA measurement was 1.3 mm, which

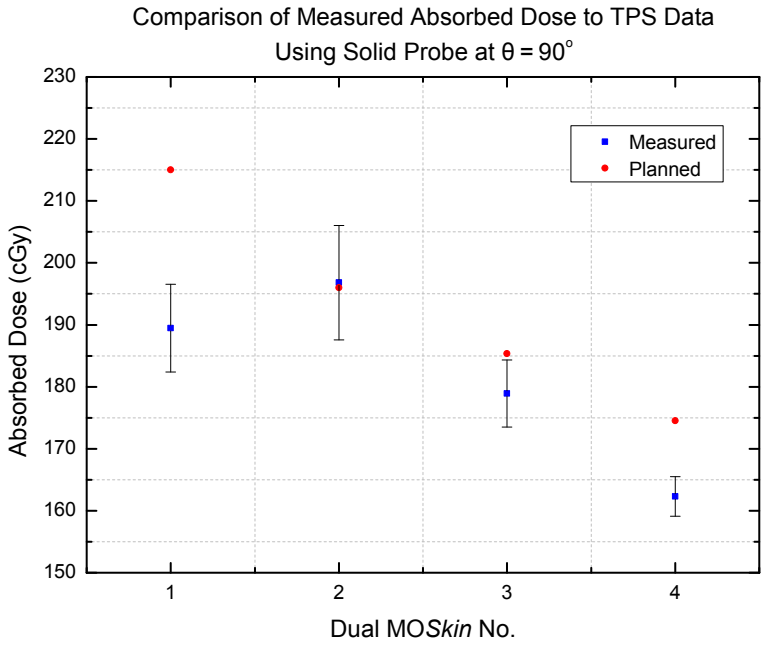

Figure 4.36 Graph of absorbed dose taken from the TPS data in comparison to the dose measured experimentally, using four dual MO*Skin*™ detectors on solid probe at $\theta = 90°$ for the $1.37 \times 1.37 \times 1.00$ mm^3 dose grid.

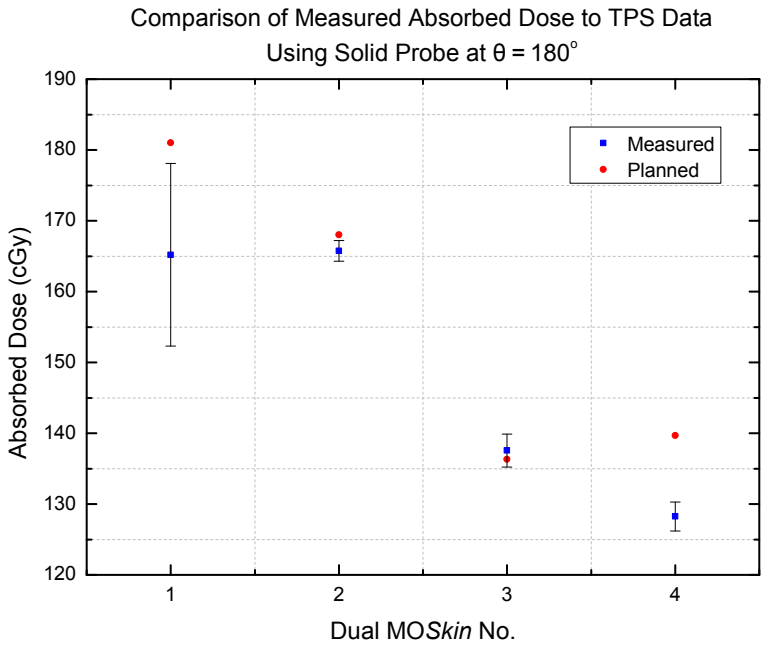

Figure 4.37 Graph of absorbed dose taken from the TPS data in comparison to the dose measured experimentally, using four dual MO*Skin*™ detectors on solid probe at $\theta = 180°$ for the $1.37 \times 1.37 \times 1.00$ mm^3 dose grid.

Angle (θ)	Detector	DTA (mm)
0°	4	1.3
90°	1	4.3
	2	2.8
180°	1	3.9
	4	2.7

Table 4.4
Table of Distance–to–Agreement (DTA) values for TomoTherapy® experiment utilising dual MO*Skin*™ detectors.

was within tolerance.

For θ = 90°, dual detectors 2 and 3 measured results of 0.4% and 3.5% difference from the TPS respectively. However, dual detector 1 varied by 11.9% from the planned doses and dual detector 4 differed by 7.0%. The DTA value for dual detector 1 was 4.3 mm, which was outside of tolerance. However, the DTA measurement for dual detector 4 was within tolerance at 2.8 mm.

For θ = 180°, again, dual detector 2 and 3 showed good agreement of 1.3% and 0.9% respectively. Dual detectors 1 and 4 measured doses of 8.7% and 8.2% variation from the TPS doses. The DTA measurement for dual detector 1 was outside the acceptable limit at 3.9 mm, however, the DTA measurement for dual detector 4 was within tolerance at 2.7 mm.

For the anterior rectal wall, 75% of measurements agreed to within $\pm$5% of the planned dose. However, detector 4 had a very small DTA measurement, and if experimental error is taken into account; its 5.3% deviation can be considered within the $\pm$5% acceptance. Thus 100% agreement was observed at this location.

Considering the anterior rectal wall only, which is of greatest importance, the dual detectors proved to be superior in comparison to the single detectors. Analysing the results from the fine dose grid and solid probes for both single and dual

detectors, the agreement between experimental and planned doses is 75% and 100% respectively.

The average difference between upwards–facing and downwards–facing detectors was less than 1%. This negligible difference supports the method used in the earlier single detector measurements to calibrate the detectors utilising the composite uniform dose distribution. This type of dose distribution allowed an average dose from all angles to be measured by the detectors.

4.4.2.3 Discussion

These results show that the differences observed in the single detector experiment were most likely due to angular dependence. Hence, the dual MO*Skin*™ system would be a good method for measurements of absorbed dose in real time for TomoTherapy® prostate boost treatments, due to the helical nature of TomoTherapy®.

4.5 Conclusion

For the single detector experiment, 75% of measurements for the normal dose grid were within ±5% of the TPS calculated dose at the anterior rectal wall, compared to 87.5% for the fine dose grid, when accounting for DTA measurements. The solid and hollow probes performed equally well when utilising the fine dose grid for measurements at every detector location on the rectal wall. The solid probe was determined to be the better of the two probes for the TomoTherapy® measurements, due to the greater uncertainty in the hollow probe measurements.

25% of results were within ±5% of the TPS at the anterior rectal wall when utilising fiducial markers on the solid probe. However, all DTA values were within tolerance, indicating that image–guidance aligning to the detectors was more beneficial that aligning to separate fiducial markers. Dual MO*Skin*™ detectors

improved the single detector results, with all dual detector measurements falling within ±5% of the planned dose at the anterior rectal wall. Angular dependence therefore can explain the discrepancies in the single detector experiment.

Chapter 5

Conclusion and Future Research

Problems with prostate HDR brachytherapy and helical TomoTherapy®, such as prostate movement and the very steep dose gradient covering the anterior rectal wall, have led to uncertainty in dose to the rectal wall of the patient. Two replica probes were introduced to improve the dosimetry of prostate radiation therapy real–time, specifically for HDR brachytherapy and TomoTherapy®. MO*Skin*™ detectors were chosen for this method due to their superior measurement capabilities of absorbed dose to the anterior rectal wall, such as ability for measurements in high dose gradient areas. This method was found to be successful, although there was still difficulty with positional reproducibility.

Preliminary measurements in phantom were completed for both treatment modalities. For HDR brachytherapy, calibration was completed with calibration factors determined to be in the range of 2.42 ± 0.09 mV/cGy to 2.65 ± 0.11 mV/cGy for the single detectors, and 2.32 ± 0.07 mV/cGy for the dual detectors. Percentage depth dose measurements demonstrated that the solid water with no cavity present resulted in slightly higher doses than both cavity (cylindrical and cuboid) measurements, and both cavities produced similar results. For TomoTherapy®, the differences in dose readings between all angles were $\leq$2% for 75% of measurements, and $<$5% for 92% of measurements when measuring dose in the composite uniform dose distribution. The calibration factor for the single detector experiment, also determined by per-

forming measurements in the composite uniform dose distribution, was found to be 2.4 ± 0.1 mV/cGy. Measurements completed to determine whether the MO*Skin*™ detectors performed well in a low dose gradient region, resulted in $<1\%$ difference between measured doses and the TPS doses. The average calibration factor for the dual detectors was determined to be 2.47 ± 0.07 mV/cGy.

For HDR brachytherapy, utilising single MO*Skin*™ detectors, the hollow and solid probes demonstrated similar results, with 50% of detectors measuring dose to within $\pm 5\%$ of the expected dose from the plan. All DTA measurements were acceptable, meaning slight positional deviations were the most likely cause of the differences in dose, however, angular dependence also seemed an issue. Due to the similarity in results between the probes, it could not be determined which was the superior choice for HDR brachytherapy to the prostate, as the solid probe did not increase dose to the anterior rectal wall. This was despite results from the experiment comparing cavity and no cavity in solid water blocks, demonstrating lower doses measured for having a cavity present of 14.2–17.7% and 6.9–13.1% for 15 mm and 30 mm source–to–detector distance respectively.

Measurements with dual MO*Skin*™ detectors were then completed to investigate whether discrepancies were due to angular dependence. The solid probe was utilised, as there was no discernible difference found between the two probes and the solid probe was the more rigid of the two. 100% agreement was determined between measured and TPS doses to within 2%. Angular dependence could therefore explain the differences observed in the single detector experiment.

For TomoTherapy®, utilising single detectors, two different dose grids were compared: the normal and fine dose grids. For the fine dose grid, 62.5% of detector measurements recorded a dose to within $\pm 5\%$ of the TPS calculated dose at the anterior rectal wall, compared to 50% for the normal dose grid. Taking into account DTA values for these results increased the agreement to 75% and 87.5% for the

normal and fine dose grids respectively. Over all the measurements at every detector location on the rectal wall, the solid and hollow probes performed equally well when utilising the fine dose grid. Due to the number of measured doses agreeing with TPS doses from each probe being equal; the probe determined to be best for TomoTherapy® boost treatments to the prostate was the solid probe, based on the premise that there was more uncertainty when taking measurements using the hollow probe due to it being more difficult to observe the probe's edge on the CT scan.

The main source of uncertainty in this experiment was detector localisation. It was difficult to place the detectors in the correct position, especially in a high dose gradient region. Other sources of error included the MO*Skin*™ detectors themselves, which could sometimes be unstable in their read–out. The detectors could have also been affected by temperature or other physical factors, such as abrasion. The MO*Skin*™ detector reader also has an uncertainty in the read–out.

Fiducial markers did not improve the results, with only 25% of detectors measuring dose to within $\pm 5\%$ of the planned dose at the anterior rectal wall, although all DTA values were within tolerance. This indicated that it was beneficial to perform image–guidance aligning to the detectors, rather than to separate fiducial markers. However, other improvements to this experiment could be made by a more sophisticated probe design. The probes used here were effective, however, they were not optimised for precise positioning of the detectors. For example, the detectors could only be taped down. A more permanent solution could be implemented.

The TomoTherapy® measurements were repeated utilising dual MO*Skin*™ detectors. All detectors measured dose to within $\pm 5\%$ of the TPS at the anterior rectal wall, demonstrating that angular dependence in a helical dose delivery was the reason for previous discrepancies.

Despite very steep dose gradients, the real time measurements of the anterior rectal wall doses were within acceptable limits of the TPS predicted doses. Discrepancies between measured and TPS data were due to difficulties in precisely locating each detector in the TPS dose grid, with large variations in dose between CT voxels present in regions of steep dose gradients. The dual MO*Skin*™ system would be a useful tool for detecting errors, such as patient shifts or incorrect set–up, in real time during HDR brachytherapy and TomoTherapy® of the prostate.

The next step in this study is to validate the measurements with Gaf–chromic film due to some of the larger discrepancies observed. If results are validated appropriately, then clinical trials can begin; utilising the most ideal probe and detector combination for the treatment modalities. For brachytherapy, current procedures at SGCCC would still be carried out, so the addition of the replica probe would not significantly alter the treatment geometry. The only difference would be replacing the ultrasound probe with the replica probe after insertion of the catheters. The added detectors would provide dosimetric benefit. For TomoTherapy® the patient is not normally treated with a probe inserted for standard fractionation. However, the improvement in positional reproducibility and added detectors will provide increased confidence in treatment delivery.

Bibliography

[1] Prostate Cancer Foundation of Australia, "Prostate Cancer Statistics," 2013. [Online]. Available: http://www.prostate.org.au/articleLive/pages/Prostate-Cancer-Statistics.html

[2] M. W. Dunn and M. W. Kazer, "Prostate cancer overview," *Seminars in Oncology Nursing*, vol. 27, no. 4, pp. 241–250, 2011.

[3] N. Hardcastle, D. L. Cutajar, P. E. Metcalfe, M. L. Lerch, V. L. Perevertaylo, W. A. Tomé, and A. B. Rosenfeld, "*In–vivo* real–time rectal wall dosimetry for prostate radiotherapy," *Physics in Medicine and Biology*, vol. 55, pp. 3859–3871, 2010.

[4] I. Kwan, A. Howie, M. Lerch, B. Lee, Y. S. Chin, J. Bucci, V. Perevertaylo, and A. Rosenfeld, "Measurement of rectal dose during HDR brachytherapy using the new MO*Skin* dosimeter," *Journal of Nuclear Science and Technology*, vol. Supplement 5, pp. 481–484, 2008.

[5] E. L. Seymour, S. J. Downes, G. B. Fogarty, M. A. Izard, and P. Metcalfe, "*In–vivo* real–time dosimetric verification in high dose rate prostate brachytherapy," *Medical Physics*, vol. 38, no. 8, pp. 4785–4794, 2011.

[6] A. Haughey, G. Coalter, and K. Mugabe, "Evaluation of linear array MOSFET detectors for *in–vivo* dosimetry to measure rectal dose in HDR brachytherapy," *Australasian Physical & Engineering Sciences in Medicine*, vol. 34, no. 3, pp. 361–366, 2011.

[7] AB Mimator, Mälarvägen 8, SE-756 53 UPPSALA, Sweden.

[8] U. Isacsson, K. Nilsson, S. Asplund, E. Morhed, A. Montelius, and I. Turesson, "A method to separate the rectum from the prostate during proton beam radiotherapy of prostate cancer patients," *Acta Oncologica*, vol. 49, no. 4, pp. 500–505, 2010.

[9] K. Nilsson, A. K. Johansson, A. Montelius, I. Turesson, R. O. Heikkinen, G. Ljung, and U. Isacsson, "Decreasing the dose to the rectal wall by using a rectal rectractor during radiotherapy of prostate cancer: A comparative treatment planning study," *Journal of Radiotherapy*, pp. 1–7, 2014.

[10] S. Johansson, L. Åström, F. Sandin, U. Isacsson, A. Montelius, and I. Turesson, "Hypofractionated proton boost combined with external beam radiotherapy for treatment of localised prostate cancer," *Prostate Cancer*, vol. 2012, pp. 1–14, 2012.

[11] C. M. Washington and D. T. Leaver, *Principles and Practice of Radiation Therapy*. St. Louis: Mosby, 2004.

[12] W. J. Morris, M. Keyes, D. Palma, M. McKenzie, I. Spadinger, A. Agranovich, T. Pickles, M. Liu, W. Kwan, J. Wu, V. Lapointe, E. Berthelet, H. Pai, R. Harrison, W. Kwa, J. Bucci, V. Racz, and R. Woods, "Evaluation of dosimetric parameters and disease response after Iodine–125 transperineal brachytherapy for low– and intermediate–risk prostate cancer," *International Journal of Radiation Oncology*Biology*Physics*, vol. 73, no. 5, pp. 1432–1438, 2009.

[13] M. N. Simmons, R. K. Berglund, and S. Jones, "A practical guide to prostate cancer diagnosis and management," *Cleveland Clinic Journal of Medicine*, vol. 78, no. 5, pp. 321–331, 2011.

[14] A. C. Reese, J. E. Cowan, J. S. Brajtbord, C. R. Harris, P. R. Carroll, and M. R. Cooperberg, "The quantitative Gleason score improves prostate cancer risk assessment," *Cancer*, vol. 118, no. 24, pp. 6046–6054, 2012.

[15] F. T. Hammad, "Radical prostatectomy: Oncological outcomes," *Annals of the New York Academy of Sciences*, vol. 1138, no. 1, pp. 267–277, 2008.

[16] G. L. Lu-Yao, P. C. Albertsen, D. F. Moore, W. Shih, Y. Lin, R. S. DiPaola, and S.-L. Yao, "Survival following primary androgen deprivation therapy among men with localized prostate cancer," *The Journal of the American Medical Association*, vol. 300, no. 2, pp. 173–181, 2008.

[17] P. Metcalfe, T. Kron, and P. Hoban, *The Physics of Radiotherapy X–Rays and Electrons*. Madison, Wisconsin: Medical Physics Publishing, 2007.

[18] M. Whitaker, G. Hruby, A. Lovett, and N. Patanjali, "Prostate hdr brachytherapy catheter displacement between planning and treatment delivery," *Radiotherapy and Oncology*, vol. 101, no. 3, pp. 490–494, 2011.

[19] J. Crook, "The role of brachytherapy in the definitive management of prostate cancer," *Cancer/Radiothérapie*, vol. 15, pp. 230–237, 2011.

[20] R. Nath, L. L. Anderson, G. Luxton, K. A. Weaver, J. F. Williamson, and A. S. Meigooni, "AAPM Report 51: Dosimetry of Interstitial Brachytherapy Sources: Report of AAPM Radiation Therapy Committee Task Group 43," *Medical Physics*, vol. 2, no. 2, pp. 209–234, 1995.

[21] D. J. Brenner, A. A. Martinez, G. K. Edmundson, C. Mitchell, H. D. Thames, and E. P. Armour, "Direct evidence that prostate tumours show high sensitivity to fractionation (low alpha/beta ratio), similar to late–responding normal tissue," *International Journal of Radiation Oncology * Biology * Physics*, vol. 52, no. 1, pp. 6–13, 2002.

[22] M. Okamoto, H. Ishikawa, T. Ebara, H. Kato, T. Tamaki, T. Akimoto, K. Ito, M. Miyakubo, T. Yamamoto, K. Suzuki, T. Takahashi, and T. Nakano, "Rectal bleeding after high–dose–rate brachytherapy combined with hypofractionated external–beam radiotherapy for localized prostate cancer: The relationship between dose–volume histogram parameters and the occurrence rate," *International Journal of Radiation Oncology * Biology * Physics*, pp. 1–7, 2011.

[23] J. M. Michalski, J. A. Purdy, K. Winter, M. R. 3rd, S. Vijayakumar, H. M. Sandler, M. A. R. A. M. Markoe, K. J. Russell, S. Sailer, W. B. Harms, C. A. Perez, R. B. Wilder, G. E. Hanks, and J. D. Cox, "Preliminary report of toxicity following 3D radiation therapy for prostate cancer on 3DOG/RTOG 9406," *International Journal of Radiation Oncology * Biology * Physics*, vol. 46, no. 2, pp. 391–402, 2000.

[24] P. Hoskin, A. Rojas, G. Lowe, L. Bryant, P. Ostler, R. Huges, J. Milner, and H. Chadd, "High–dose–rate brachytherapy alone for localised prostate cancer in patients at moderate or high risk of biochemical recurrence," *International Journal of Radiation Oncology * Biology * Physics*, pp. 1–9, 2011.

[25] St. George Cancer Care Centre, "Public hospital brachytherapy available at prostate cancer institute," 2007.

[26] M. J. Rivard, J. L. M. Venselaar, and L. Beaulieu, "The evolution of brachytherapy treatment planning," *Medical Physics*, vol. 36, no. 6, pp. 2136–2153, 2009.

[27] L. Beaulieu, A. C. Tedgren, J.-F. Carrier, S. D. Davis, F. Mourtada, M. J. Rivard, R. M. Thomson, F. Verhaegen, T. A. Wareing, and J. F. Williamson, "Report of the Task Group 186 on model–based dose calculation methods in brachytherapy beyond the TG–43 formalism: current status and recommendations for clinical implementation," *Medical Physics*, vol. 39, no. 10, pp. 6208–6236, 2012.

[28] M. J. Zelefsky, R. K. Valicenti, M. Hunt, and C. A. Perez, "Chapter 62: Low–Risk Prostate Cancer," in *Perez and Brady's Principles and Practice of Radiation Oncology, 5th ed.*, E. C. Halperin, C. A. Perez, L. W. Brady, D. E. Wazer, C. Freeman, and L. R. Prosnitz, Eds. Philadelphia: Lippincott Williams & Wilkins, 2008, pp. 1439–1482.

[29] K. S. Jothybasu, A. Bahl, V. Subramani, G. K. Rath, D. N. Sharma, and P. K. Julka, "Static versus dynamic intensity–modulated radiotherapy: Profile of

integral dose in carcinoma of the nasopharynx," *Journal of Medical Physics*, vol. 34, no. 2, pp. 66–72, 2009.

[30] C. S. Chui, M. F. Chan, E. Yorke, S. Spirou, and L. C. Clifton, "Delivery of intensity modulated radiotherapy with a conventional multileaf collimator: comparison of dynamic and segmental methods," *Medical Physics*, vol. 28, no. 12, pp. 2441–2449, 2001.

[31] P. Alaei, P. D. Higgins, R. Weaver, and N. Nguyen, "Comparison of dynamic and step–and–shoot intensity-modulated radiation therapy planning and delivery," *Medical Dosimetry*, vol. 29, no. 1, pp. 1–6, 2004.

[32] M. T. Vlachaki, T. N. Teslow, C. Amosson, N. W. Uy, and S. Ahmad, "IMRT versus conventional 3DCRT on prostate and normal tissue dosimetry using an endorectal balloon for prostate immobilization," *Medical Dosimetry*, vol. 30, no. 2, pp. 69–75, 2005.

[33] L. Arbea, L. I. Ramos, R. Martnez-Monge, M. Moreno, and J. Aristu, "Intensity-modulated radiation therapy (IMRT) vs. 3D conformal radiotherapy (3DCRT) in locally advanced rectal cancer (LARC): dosimetric comparison and clinical implications," *Radiation Oncology*, vol. 5, no. 17, pp. 1–9, 2010.

[34] S. M. MacDonald, S. Ahmad, S. Kachris, B. J. Vogds, M. DeRouen, A. E. Gitttleman, K. DeWyngaert, and M. T. Vlachaki, "Intensity modulated radiation therapy versus three–dimensional conformal radiation therapy for the treatment of high grade glioma: a dosimetric comparison," *Journal of Applied Clinical Medical Physics*, vol. 8, no. 2, pp. 47–60, 2007.

[35] S. F. Kry, M. Salehpour, D. S. Followill, M. Stovall, D. A. Kuban, R. A. White, and I. I. Rosen, "The calculated risk of fatal secondary malignancies from intensity modulated radiation therapy," *International Journal of Radiation Oncology * Biology * Physics*, vol. 62, no. 4, pp. 1195–1203, 2005.

[36] J. Michalski, Y. Yan, D. Watkins-Bruner, B. Walter, K. Winter, J. Galvin, J. Bahary, G. Morton, M. Parliament, and H. Sandler, "Preliminary analysis of 3D–CRT vs. IMRT on the high dose arm of the RTOG 0126 prostate cancer trial: toxicity report," *International Journal of Radiation Oncology * Biology * Physics*, vol. 81, no. 2, Supplement, pp. S1–S2, 2011.

[37] T. R. Mackie, T. Holmes, S. Swerdloff, P. Reckwerdt, J. O. Deasy, J. Yang, B. Paliwal, and T. Kinsella, "Tomotherapy: a new concept for the delivery of dynamic conformal radiotherapy," *Medical Physics*, vol. 20, no. 6, pp. 1709–1719, 1993.

[38] C. R. Ramsey, D. Scaperoth, R. Seibert, D. Chase, T. Byrne, and S. Mahan, "Image–guided helical tomoherapy for localized prostate cancer: technique and initial clinical observations," *Journal of Applied Clinical Medical Physics*, vol. 8, no. 3, pp. 37–51, 2007.

[39] K. M. Langen, Y. Zhang, R. D. Andrews, M. E. Hurley, S. L. Meeks, D. O. Poole, T. R. Willoughby, and P. A. Kupelian, "Initial experience with megavoltage (MV) CT guidance for daily prostate alignments," *International Journal of Radiation Oncology * Biology * Physics*, vol. 62, no. 5, pp. 1517–1524, 2005.

[40] S. L. Mahan, C. R. Ramsey, S. S. Scaperoth, D. J. Chase, and T. E. Byrne, "Evaluation of image–guided helical tomotherapy for the re–treatment of spinal metastasis," *International Journal of Radiation Oncology * Biology * Physics*, vol. 63, no. 5, pp. 1576–1583, 2005.

[41] P. A. Kupelian, C. Ramsey, S. L. Meeks, T. R. Willoughby, A. Forbes, T. H. Wagner, and K. M. Langen, "Serial megavoltage CT imaging during external beam radiotherapy for non–small cell lung cancer: observations on tumor regression during treatment," *International Journal of Radiation Oncology * Biology * Physics*, vol. 63, no. 4, pp. 1024–1028, 2005.

[42] M. Mehta, P. Hoban, and T. R. Mackie, "Commissioning and Quality Assurance of RapidArc Radiotherapy Delivery System: In Regard to Ling et al. (Int J Radiat Oncol Biol Phys 2008;72;575–581): Absence of Data Does Not Constitute Proof; The Proof is in Tasting the Pudding," *International Journal of Radiation Oncology * Biology * Physics*, vol. 75, no. 1, pp. 4–6, 2009.

[43] M. A. Hawkins, J. L. Bedford, and D. M. Tait, "Volumetric modulated arc therapy planning for distal oesophageal malignancies," *British Journal of Radiology*, vol. 85, no. 1009, pp. 44–52, 2012.

[44] T. Bortfeld and S. Webb, "Single–arc IMRT?" *Physics in Medicine and Biology*, vol. 54, no. 1, pp. N9–20, 2009.

[45] K. Otto, "Volumetric modulated arc therapy: IMRT in a single gantry arc," *Medical Physics*, vol. 35, no. 1, pp. 310–317, 2008.

[46] Independent Hospital Pricing Authority, "A Review and Costing Study into Radiotherapy Services: Final Report," 2013.

[47] A. Pollack, G. K. Zagars, G. Starkschall, J. A. Antolak, J. J. Lee, E. Huang, A. C. von Eschenbach, D. A. Kuban, and I. Rosen, "Prostate cancer radiation dose response: results of the M. D. Anderson phase III randomized trial," *International Journal of Radiation Oncology * Biology * Physics*, vol. 53, no. 5, pp. 1097–1105, 2002.

[48] A. Pollack, R. A. P. Jr., L. Dong, S. J. Feigenberg, and E. M. Horwitz, "Chapter 22a: Intact Prostate Cancer: Overview," in *Intensity Modulated Radiation Therapy: A Clinical Perspective*, A. J. Mundt and J. C. Roeske, Eds. Hamilton, ON, Canada: BC Decker, 2005, pp. 459–463.

[49] C. L. Tsai, J. K. Wu, H. L. Chao, Y. C. Tsai, and J. C. Cheng, "Treatment and dosimetric advantages between VMAT, IMRT, and helical tomotherapy in prostate cancer," *Medical Dosimetry*, vol. 36, no. 3, pp. 264–271, 2011.

[50] F. Kjaer-Kristoffersen, L. Ohlhues, J. Medin, and S. Korreman, "RapidArc volumetric modulated therapy planning for prostate cancer patients," *Acta Oncologica*, vol. 48, no. 2, pp. 227–232, 2009.

[51] C. R. Ramsey, R. Seibert, S. L. Mahan, D. Desai, and D. Chase, "Out–of–field dosimetry measurements for a helical tomotherapy system," *Journal of Applied Clinical Medical Physics*, vol. 7, no. 3, pp. 1–11, 2006.

[52] C. Cozzarini, C. Fiorino, N. D. Muzio, F. Alongi, S. Broggi, M. Cattaneo, F. Montorsi, P. Rigatti, R. Calandrinob, and F. Fazio, "Signifcant reduction of acute toxicity following pelvic irradiation with Helical Tomotherapy in patients with localised prostate cancer," *Radiotherapy and Oncology*, vol. 84, no. 2, pp. 164–170, 2007.

[53] A. J. Katz, M. Santoro, R. Ashley, F. Diblasio, and M. Witten, "Stereotactic body radiotherapy as boost for organ–confined prostate cancer," *Technology in Cancer Research & Treatment*, vol. 9, no. 6, pp. 575–582, 2010.

[54] S. Jabbari, V. K. Weinberg, T. Kaprealian, I. C. Hsu, L. Ma, C. Chuang, M. Descovich, S. Shiao, K. Shinohara, M. R. 3rd, and A. R. Gottschalk, "Stereotactic body radiotherapy as monotherapy or post–external beam radiotherapy boost for prostate cancer: technique, early toxicity, and PSA response," *International Journal of Radiation Oncology * Biology * Physics*, vol. 82, no. 1, pp. 228–234, 2012.

[55] E. K. Oermann, R. S. Slack, H. N. Hanscom, S. Lei, S. Suy, H. U. Park, J. S. Kim, B. A. Sherer, B. T. Collins, A. N. Satinsky, K. W. Harter, G. P. Batipps, N. L. Constantinople, S. W. Dejter, W. C. Maxted, J. B. Regan, J. J. Pahira, K. G. McGeagh, R. C. Jha, N. A. Dawson, A. Dritschilo, J. H. Lynch, and S. P. Collins, "A pilot study of intensity modulated radiation therapy with hypofractionated stereotactic body radiation therapy (SBRT) boost in the treatment of intermediate– to high–risk prostate cancer," *Technology in Cancer Research & Treatment*, vol. 9, no. 5, pp. 453–462, 2010.

[56] Y. Xie, D. Djajaputra, C. R. King, S. Hossain, L. Ma, and L. Xing, "Intrafractional motion of the prostate during hypofractionated radiotherapy," *International Journal of Radiation Oncology * Biology * Physics*, vol. 72, no. 1, pp. 236–246, 2008.

[57] C. R. King, J. D. Brooks, H. Gill, T. Pawlicki, C. Cotrutz, and J. J. C. Presti, "Stereotactic body radiotherapy for localized prostate cancer: Interim results of a prospective phase II clinical trial," *International Journal of Radiation Oncology * Biology * Physics*, vol. 73, no. 4, pp. 1043–1048, 2009.

[58] M. J. Barry, J. F. J. Fowler, M. P. O'Leary, R. C. B. H. L. Holtgrewe, W. K. Mebust, and A. T. Cockett, "The American Urological Association symptom index for benign prostatic hyperplasia. The Measurement Committee of the American Urological Association," *Journal of Urology*, vol. 148, no. 5, pp. 1549–1557; discussion 1564, 1992.

[59] J. T. Wei, R. L. Dunn, M. S. Litwin, H. M. Sandler, and M. G. Sanda, "Development and validation of the expanded prostate cancer index composite (EPIC) for comprehensive assessment of health–related quality of life in men with prostate cancer," *Urology*, vol. 56, no. 6, pp. 899–905, 2000.

[60] E. Sterpin, F. Salvat, G. Olivera, and S. Vynckier, "Monte Carlo evaluation of the convolution/superposition algorithm of Hi–Art tomotherapy in heterogeneous phantoms and clinical cases," *Medical Physics*, vol. 36, no. 5, pp. 1566–1575, 2009.

[61] N. Dogan, I. Mihaylov, Y. Wu, P. J. Keall, J. V. Siebers, and M. P. Hagan, "Monte Carlo dose verification of prostate patients treated with simultaneous integrated boost intensity modulated radiation therapy," *Radiation Oncology*, vol. 4, no. 18, pp. 1–17, 2009.

[62] P. Francescon, S. Cora, and P. Chiovati, "Dose verification of an IMRT treatment planning system with the BEAM EGS4-based Monte Carlo code," *Medical Physics*, vol. 30, no. 2, pp. 144–157, 2003.

[63] K. M. Langen, W. Lu, T. R. Willoughby, B. Chauhan, S. L. Meeks, P. A. Kupelian, and G. Olivera, "Dosimetric effect of prostate motion during helical tomotherapy," *International Journal of Radiation Oncology * Biology * Physics*, vol. 74, no. 4, pp. 1134–1142, 2009.

[64] K. M. Langen, T. R. Willoughby, S. L. Meeks, A. Santhanam, A. Cunningham, L. Levine, and P. Kupelian, "Observations on real–time prostate gland motion using electromagnetic tracking," *International Journal of Radiation Oncology * Biology * Physics*, vol. 71, no. 4, pp. 1084–1090, 2008.

[65] P. Kupelian, T. Willoughby, A. Mahadevan, T. Djemil, G. Weinstein, S. Jani, C. Enke, T. Solberg, N. Flores, D. Liu, D. Beyer, and L. Levine, "Multi–institutional clinical experience with the Calypso System in localization and continuous, real–time monitoring of the prostate gland during external radiotherapy," *International Journal of Radiation Oncology * Biology * Physics*, vol. 67, no. 4, pp. 1088–1098, 2007.

[66] A. Jain, A. Deguet, I. Iordachita, G. Chintalapani, S. Vikal, J. Blevins, Y. Le, E. Armour, C. Burdette, D. Song, and G. Fichtinger, "Intra–operative 3D guidance and edema detection in prostate brachytherapy using a non–isocentric C–arm," *Medical Image Analysis*, vol. 16, no. 3, pp. 731–743, 2010.

[67] D. S. Park, "Current status of brachytherapy for prostate cancer," *Korean Journal of Urology*, vol. 53, no. 11, pp. 743–749, 2012.

[68] S. Nag, J. Ciezki, R. Cormack, S. Doggett, K. DeWyngaert, G. Edmundson, R. Stock, N. Stone, Y. Yu, and M. Zelefsky, "Intraoperative planning and evaluation of permanent prostate brachytherapy: Report of the American Brachytherapy Society," *International Journal of Radiation Oncology * Biology * Physics*, vol. 51, no. 5, pp. 1422–1430, 2001.

[69] R. R. Patel, N. Orton, W. A. Tomé, R. Chappell, and M. A. Ritter, "Rectal dose sparing with a balloon catheter and ultrasound localization in conformal

radiation therapy for prostate cancer," *Radiotherapy and Oncology*, vol. 67, no. 3, pp. 285–294, 2003.

[70] R. Miralbell, M. Mollà, R. Arnalte, S. C. E. Vargas, D. Linero, S. Waters, P. Nouet, M. Rouzaud, and L. Escudé, "Target repositioning optimization in prostate cancer: is intensity–modulated radiotherapy under stereotactic conditions feasible?" *International Journal of Radiation Oncology * Biology * Physics*, vol. 59, no. 2, pp. 366–371, 2004.

[71] W. R. Noyes, C. C. Hosford, and S. E. Schultz, "Human collagen injections to reduce rectal dose during radiotherapy," *International Journal of Radiation Oncology * Biology * Physics*, vol. 82, no. 5, pp. 1918–1922, 2012.

[72] R. B. Wilder, G. A. Barme, R. F. Gilbert, R. E. Holevas, L. I. Kobashi, R. R. Reed, R. S. Solomon, N. L. Walter, L. Chittenden, A. V. Mesa, J. Agustin, J. Lizarde, J. Macedo, J. Ravera, and K. M. Tokita, "Cross–linked hyaluronan gel reduces the acute rectal toxicity of radiotherapy for prostate cancer," *International Journal of Radiation Oncology * Biology * Physics*, vol. 77, no. 3, pp. 824–830, 2010.

[73] E. Daar, L. King, A. Nisbet, R. B. Thorpe, and D. A. Bradley, "Viscosity changes in hyaluronic acid: Irradiation and rheological studies," *Applied Radiation and Isotopes*, vol. 68, no. 4–5, pp. 746–750, 2010.

[74] R. J. Smeenk, E. N. J. T. van Lin, P. van Kollenburg, G. M. McColl, M. Kunze-Busch, and J. H. A. M. Kaanders, "Endorectal balloon reduces anorectal doses in post–prostatectomy intensity–modulated radiotherapy," *Radiotherapy and Oncology*, vol. 101, no. 3, pp. 465–470, 2011.

[75] American Association of Physicists in Medicine, "AAPM Report No. 87: Diode *In–Vivo* Dosimetry for Patients Receiving External Beam Radiation Therapy. Report of Task Group 62 of the Radiation Therapy Committee," Madison, Wisconsin, Tech. Rep., 2005.

[76] International Commission on Radiation Units and Measurements, "Determination of absorbed dose in a patient irradiated by beams of x or gamma rays in radiotherapy procedures. ICRU Report 24." Bethesda, Tech. Rep., 1976.

[77] Z.-Y. Qi, X.-W. Deng, S.-M. Huang, J. Lu, M. Lerch, D. Cutajar, and A. Rosenfeld, "Verification of the plan dosimetry for high dose rate brachytherapy using metal–oxide–semiconductor field effect transistor detectors," *Medical Physics*, vol. 34, no. 6, pp. 2007–2013, 2007.

[78] M. J. Butson, P. K. N. Yu, T. Cheung, and P. Metcalfe, "Radiochromic film for medical radiation dosimetry," *Materials Science and Engineering*, vol. 41, no. 3, pp. 61–120, 2003.

[79] P. Z. Y. Liu, N. Suchowerska, P. Abolfathi, and D. R. McKenzie, "Real–time scintillation array dosimetry for radiotherapy: The advantages of photomultiplier detectors," *Medical Physics*, vol. 39, no. 4, pp. 1688–1695, 2012.

[80] M. Essers and B. J. Mijnheer, "*In–vivo* dosimetry during external photon beam radiotherapy," *International Journal of Radiation Oncology * Biology * Physics*, vol. 43, no. 2, pp. 245–259, 1999.

[81] A. Gopiraj, R. S. Billimagga, and V. Ramasubramanian, "Performance characteristics and commissioning of MOSFET as an *in–vivo* dosimeter for high energy photon external beam radiation therapy," *Reports of Practical Oncology and Radiotherapy*, vol. 13, no. 3, pp. 114–125, 2008.

[82] M. Rivard, B. Coursey, L. DeWerd, W. Hanson, M. S. Huq, G. Ibbott, M. Mitch, R. Nath, and J. Williamson, "Update of AAPM Task Group No. 43 Report: A revised AAPM protocol for brachytherapy dose calculations," *Medical Physics*, vol. 31, no. 3, pp. 633–674, 2004.

[83] F. H. Attix, *Introduction to Radiological Physics and Radiation Dosimetry*. Weinheim: Wiley–VCH Verlag GmbH, 2004.

[84] A. Rosenfeld, "Semiconductor Detectors in Radiation Medicine: Radiotherapy and Related Applications," in *Radiation Detectors for Medical Applications*, S. Tavernier, A. Gektin, B. Grinyov, and W. W. Moses, Eds. Dordrecht: Springer, 2005, pp. 111–143.

[85] J. Lambert, T. Nakano, S. Law, J. Elsey, D. R. McKenzie, and N. Suchowerska, "*In–vivo* dosimeters for HDR brachytherapy: A comparison of a diamond detector, MOSFET, TLD, and scintillation detector," *Medical Physics*, vol. 34, no. 5, pp. 1759–1765, 2007.

[86] A. B. Rosenfeld, "MOSFET dosimetry on modern radiation oncology modalities," *Radiation Protection Dosimetry*, vol. 101, no. 1–4, pp. 393–398, 2002.

[87] A. S. Saini and T. C. Zhu, "Energy dependence of commercially available diode detectors for in–vivo dosimetry," *Medical Physics*, vol. 34, no. 5, pp. 1704–1711, 2007.

[88] N. Hardcastle, E. Metcalfe, A. B. Rosenfeld, and W. A. Tomé, "Endo–rectal balloon cavity dosimetry in a phantom: Performance under imrt and helical tomotherapy beams," *Radiotherapy and Oncology*, vol. 92, no. 1, pp. 48–56, 2009.

[89] V. Rudat, A. Nour, A. A. Alaradi, A. Mohamed, and S. Altuwaijri, "In vivo surface dose measurement using gafchromic film dosimetry in breast cancer radiotherapy: Comparison of 7–field imrt, tangential imrt and tangential 3d–crt," *Radiation Oncology*, vol. 9, no. 156, pp. 1–9, 2014.

[90] M. Avanzo, A. Rink, A. Dassie, S. Massarut, M. Roncadin, E. Borsatti, and E. Capra, "In vivo dosimetry with radiochromic films in low–voltage intraoperative radiotherapy of the breast," *Medical Physics*, vol. 39, no. 5, pp. 2359–2368, 2012.

[91] M. Ciocca, R. Orecchia, C. Garibaldi, E. Rondi, A. Luini, G. Gatti, M. Intra, P. Veronesi, R. Lazzari, G. Tosi, and U. Veronesi, "In vivo dosimetry using

radiochromic films during intraoperative electron beam radiation therapy in early–stage breast cancer," *Radiotherapy and Oncology*, vol. 69, no. 3, pp. 285–289, 2003.

[92] J. Izewska and G. Rajan, "Chapter 3: Radiation Dosimeters," in *Radiation Oncology Physics: A Handbook for Teachers and Students*, E. Podgorsak, Ed. Vienna: International Atomic Energy Agency, 2005, pp. 71–99.

[93] Y. Cheng and C. Hu, *MOSFET Modeling and BSIM3 User's Guide*. New York: Kluwer Academic Publishers, 2002.

[94] R. Ramani, S. Russell, and P. O'Brien, "Clinical dosimetry using mosfets," *International Journal of Radiation Oncology * Biology * Physics*, vol. 37, no. 4, pp. 959–964, 1997.

[95] J. E. Cygler, A. Saoudi, G. Perry, C. Morash, and C. E, "Feasibility study of using MOSFET detectors for *in–vivo* dosimetry during permanent low–dose–rate prostate implants," *Radiotherapy and Oncology*, vol. 80, pp. 296–301, 2006.

[96] V. O. Zilio, O. P. Joneja, Y. Popowski, A. Rosenfeld, and R. Chawla, "Absolute depth–dose–rate measurements for an Ir-192 HDR brchytherapy source in water using MOSFET detectors," *Medical Physics*, vol. 33, no. 6, pp. 1532–1539, 2006.

[97] I. S. Kwan, D. Wilkinson, D. Cutajar, M. Lerch, A. Rosenfeld, A. Howie, J. Bucci, Y. Chin, and V. L. Perevertaylo, "The effect of rectal heterogeneity on wall dose in high dose rate brachytherapy," *Medical Physics*, vol. 36, no. 1, pp. 224–232, 2009.

[98] T. Cheung, M. J. Butson, and P. K. N. Yu, "Energy dependence corrections to MOSFET dosimetric sensitivity," *Australasian Physical & Engineering Sciences in Medicine*, vol. 32, no. 1, pp. 16–20, 2009.

[99] University of Wollongong, "MO*SKIN*: MOSFET Dosimetry System," 2010. [Online]. Available: http://www.uow.edu.au/research/icr/content/groups/public/@web/@raid/documents/doc/uow082586.pdf

[100] I. S. Kwan, A. B. Rosenfeld, Z. Y. Qi, D. Wilkinson, M. L. F. Lerch, D. L. Cutajar, M. Safavi-Naeni, M. Butson, J. A. Bucci, Y. Chin, and V. L. Perevertaylo, "Skin dosimetry with new MOSFET detectors," *Radiation Measurements*, vol. 43, no. 2–6, pp. 929–932, 2008.

[101] S. Devic, J. Seuntjens, W. Abdel-Rahman, M. Evans, M. Olivares, E. B. Podgorsak, T. Vuong, and C. G. Soares, "Accurate skin dose measurements using radiochromic film in clinical applications," *Medical Physics*, vol. 33, no. 4, pp. 1116–1124, 2006.

[102] International Commission on Radiation Units and Measurements, "ICRP Publication 60, Recommendations of the International Commission on Radiological Protection." Oxford, Tech. Rep., 1991, Pergamon.

[103] ——, "Determination of dose equivalents resulting from external radiation sources. ICRU Report 39." Washington, DC, Tech. Rep., 1985.

[104] A. Hayton, A. Haworth, D. Waterhouse, S. Todd, and J. Pillainayagam, "Lack of backscatter factor measurements in HDR applications with MO*Skin*," *Australasian Physical & Engineering Sciences in Medicine*, vol. 34, no. 4, pp. 545–552, 2011.

[105] I. Kwan, B. Lee, W. J. Yoo, D. Cho, K. Jang, S. Shin, M. Carolan, M. Lerch, V. Perevertaylo, and A. Rosenfeld, "Comparison of the new MO*Skin* detector and fiber optic dosimetry system for radiotherapy," *Journal of Nuclear Science and Technology*, vol. Supplement 5, pp. 518–521, 2008.

[106] D. A. Low, "Evaluation of the gamma dose distribution comparison method," *Medical Physics*, vol. 30, no. 9, pp. 2455–2464, 2003.

[107] J. C. F. de Winter, "Using the Student's t–test with extremely small sample sizes," *Practical Assessment, Research and Evaluation*, vol. 18, no. 10, pp. 1–12, 2001.

[108] N. Hardcastle, "Towards optimal treatment planning and novel dosimetry for cancer patients receiving intensity modulated radiation therapy," PhD thesis, University of Wollongong, 2009.

[109] D. A. Low, W. B. Harms, S. Mutic, and J. A. Purdy, "A technique for the quantitative evaluation of dose distributions," *Medical Physics*, vol. 25, no. 5, pp. 656–661, 1998.

[110] L. Petrokokkinos, K. Zourari, E. Pantelis, A. Moutsatsos, P. Karaiskos, L. Sakelliou, I. S. E. Georgiou, and P. Papagiannis, "Dosimetric accuracy of a deterministic radiation transport based ^{192}I brachytherapy treatment planning system. Part II: Monte Carlo and experimental verification of a multiple source dwell position plan employing a shielded applicator," *Medical Physics*, vol. 38, no. 4, pp. 1981–1992, 2011.

[111] I. S. Kwan, "Characterization of the performance of the new MO*Skin* dosimeter as a quality assurance tool for pulsed dose–rate (PDR) prostate brachytherapy, and the effect of rectal heterogeneity on the dose delivered to the rectal wall," PhD thesis, University of Wollongong, 2009.

[112] Computerized Imaging Reference Systems Inc (CIRS), "IMRT Head & Torso Freepoint Phantom," Online, Norfolk, Virginia, 2011.

[113] R. Jeraj, T. R. Mackie, J. Balog, G. Olivera, D. Pearson, J. Kapatoes, K. Ruchala, and P. Reckwerdt, "Radiation characteristics of helical tomotherapy," *Medical Physics*, vol. 31, no. 2, pp. 396–404, 2004.

[114] J. Venselaara, H. Welleweerdb, and B. Mijnheerc, "Tolerances for the accuracy of photon beam dose calculations of treatment planning systems," *Radiotherapy and Oncology*, vol. 60, no. 2, pp. 191–201, 2001.

[115] International Atomic Energy Agency, "Technical Reports Series No. 430: Commissioning and Quality Assurance of Computerized Planning Systems for Radiation Treatment of Cancer," Vienna, Tech. Rep., 2004.

Appendix A

Tabulated TPS and Measured Data

Detector	Planned D/F (cGy)	Measured D/F (cGy)	Measured D/F Uncertainty (cGy)	% Difference
1	531.83	496.09	12.16	-6.7208
2	577.01	557.96	22.47	-3.3016
3	580.55	572.86	22.97	-1.3239
4	490.07	546.42	23.16	11.499

Table A.1
Comparison between HDR Brachytherapy TPS data and measured dose using four single MO*Skin*^{TM} detectors with the hollow probe.

Detector	Planned D/F (cGy)	Measured D/F (cGy)	Measured D/F Uncertainty (cGy)	% Difference
1	531.83	494.31	23.84	-7.0550
2	577.01	564.07	23.97	-2.2426
3	580.55	580.64	34.42	0.015491
4	490.07	529.84	26.47	8.1144

Table A.2
Comparison between HDR Brachytherapy TPS data and measured dose using four single MO*Skin*^{TM} detectors with the solid probe.

Detector	Planned D/F (cGy)	Measured D/F (cGy)	Measured D/F Uncertainty (cGy)	% Difference
1	552.83	552.68	14.66	-0.027722
3	603.64	614.49	23.15	1.7979

Table A.3
Comparison between HDR Brachytherapy TPS data and measured dose using four dual MO*Skin*™ detectors with the solid probe.

Detector	Planned D/F (cGy)	Measured D/F (cGy)	Measured D/F Uncertainty (cGy)	% Difference
1	298.7	285.5	12.8	4.417
2	270.8	278.0	10.8	-2.616
3	241.5	247.3	8.1	-2.390
4	199.5	197.9	7.3	0.8156

Table A.4
Comparison between TomoTherapy® TPS data and measured dose using four MO*Skin*™ detectors with the hollow probe at $\theta = 0^\circ$ for the $2.00 \times 2.00 \times 2.00$ mm^3 dose grid.

Detector	Planned D/F (cGy)	Measured D/F (cGy)	Measured D/F Uncertainty (cGy)	% Difference
1	251.8	278.0	8.4	-10.30
2	242.3	266.4	8.4	-9.949
3	204.0	240.7	8.7	-17.99
4	161.3	177.7	10.9	-10.16

Table A.5
Comparison between TomoTherapy® TPS data and measured dose using four MO*Skin*™ detectors with the solid probe at $\theta = 0^\circ$ for the $2.00 \times 2.00 \times 2.00$ mm^3 dose grid.

Detector	Planned D/F (cGy)	Measured D/F (cGy)	Measured D/F Uncertainty (cGy)	% Difference
1	227.2	204.9	1.3	9.815
2	201.2	187.2	1.3	6.924
3	183.2	173.0	1.3	5.570
4	133.0	129.7	1.3	2.464

Table A.6
Comparison between TomoTherapy® TPS data and measured dose using four MO*Skin*™ detectors with the hollow probe at $\theta = 90^\circ$ for the $2.00 \times 2.00 \times 2.00$ mm^3 dose grid.

Detector	Planned D/F (cGy)	Measured D/F (cGy)	Measured D/F Uncertainty (cGy)	% Difference
1	194.8	194.0	2.1	0.3673
2	181.3	178.1	0.6	1.678
3	149.5	162.7	5.7	-8.953
4	103.7	112.8	4.3	-8.892

Table A.7
Comparison between TomoTherapy® TPS data and measured dose using four MO*Skin*™ detectors with the solid probe at $\theta = 90^\circ$ for the $2.00 \times 2.00 \times 2.00$ mm^3 dose grid.

Detector	Planned D/F (cGy)	Measured D/F (cGy)	Measured D/F Uncertainty (cGy)	% Difference
1	174.8	154.9	6.5	11.39
2	154.3	132.0	1.6	14.50
3	146.3	130.8	3.2	10.59
4	124.8	118.5	5.9	5.051

Table A.8
Comparison between TomoTherapy® TPS data and measured dose using four MO*Skin*™ detectors with the hollow probe at $\theta = 180^\circ$ for the $2.00 \times 2.00 \times 2.00$ mm^3 dose grid.

Detector	Planned D/F (cGy)	Measured D/F (cGy)	Measured D/F Uncertainty (cGy)	% Difference
1	145.0	148.9	5.9	-2.686
2	131.0	128.0	5.5	2.257
3	122.5	127.3	2.6	-3.954
4	99.7	107.3	3.0	-7.692

Table A.9
Comparison between TomoTherapy® TPS data and measured dose using four MO*Skin*™ detectors with the solid probe at $\theta = 180°$ for the $2.00 \times 2.00 \times 2.00$ mm^3 dose grid.

Detector	Planned D/F (cGy)	Measured D/F (cGy)	Measured D/F Uncertainty (cGy)	% Difference
1	228.5	231.0	4.7	1.111
2	219.0	213.4	2.2	-2.554
3	211.0	222.5	5.8	5.451
4	173.2	183.6	7.4	6.025

Table A.10
Comparison between TomoTherapy® TPS data and measured dose using four MO*Skin*™ detectors with the hollow probe at $\theta = 0°$ for the $1.37 \times 1.37 \times 2.00$ mm^3 dose grid.

Detector	Planned D/F (cGy)	Measured D/F (cGy)	Measured D/F Uncertainty (cGy)	% Difference
1	245.2	237.5	12.1	-3.137
2	236.5	238.9	3.6	1.004
3	229.2	231.2	3.9	0.8778
4	188.3	211.6	3.8	12.35

Table A.11
Comparison between TomoTherapy® TPS data and measured dose using four MO*Skin*™ detectors with the solid probe at $\theta = 0°$ for the $1.37 \times 1.37 \times 2.00$ mm^3 dose grid.

Detector	Planned D/F (cGy)	Measured D/F (cGy)	Measured D/F Uncertainty (cGy)	% Difference
1	181.7	181.1	4.3	-0.3228
2	161.8	157.4	8.1	-2.720
3	162.7	156.6	2.8	-3.735
4	122.2	126.9	3.4	3.894

Table A.12
Comparison between TomoTherapy® TPS data and measured dose using four MO*Skin*™ detectors with the hollow probe at $\theta = 90^\circ$ for the $1.37 \times 1.37 \times 2.00$ mm^3 dose grid.

Detector	Planned D/F (cGy)	Measured D/F (cGy)	Measured D/F Uncertainty (cGy)	% Difference
1	201.8	200.5	6.1	-0.6449
2	184.0	189.2	5.1	2.824
3	175.0	172.4	3.2	-1.483
4	134.0	153.2	13.6	14.35

Table A.13
Comparison between TomoTherapy® TPS data and measured dose using four MO*Skin*™ detectors with the solid probe at $\theta = 90^\circ$ for the $1.37 \times 1.37 \times 2.00$ mm^3 dose grid.

Detector	Planned D/F (cGy)	Measured D/F (cGy)	Measured D/F Uncertainty (cGy)	% Difference
1	154.8	158.0	4.3	2.039
2	124.3	121.3	6.3	-2.418
3	124.2	125.5	4.2	1.094
4	113.8	110.1	2.6	-3.252

Table A.14
Comparison between TomoTherapy® TPS data and measured dose using four MO*Skin*™ detectors with the hollow probe at $\theta = 180^\circ$ for the $1.37 \times 1.37 \times 2.00$ mm^3 dose grid.

Detector	Planned D/F (cGy)	Measured D/F (cGy)	Measured D/F Uncertainty (cGy)	% Difference
1	156.8	157.3	3.7	0.2917
2	131.8	129.7	3.6	-1.601
3	121.0	119.9	4.2	-0.8866
4	118.5	117.7	2.6	-0.6850

Table A.15
Comparison between TomoTherapy® TPS data and measured dose using four MO*Skin*™ detectors with the solid probe at $\theta = 180°$ for the $1.37 \times 1.37 \times 2.00$ mm^3 dose grid.

Detector	Planned D/F (cGy)	Measured D/F (cGy)	Measured D/F Uncertainty (cGy)	% Difference
1	311.7	325.9	12.7	4.572
2	306.5	331.5	18.9	8.161
3	286.5	326.2	13.3	13.86
4	258.0	282.0	12.2	9.293

Table A.16
Comparison between TomoTherapy® TPS data and measured dose using four MO*Skin*™ detectors with the solid probe at $\theta = 0°$ for the $1.37 \times 1.37 \times 1.00$ mm^3 dose grid. Fiducial markers were attached to the probe.

Detector	Planned D/F (cGy)	Measured D/F (cGy)	Measured D/F Uncertainty (cGy)	% Difference
1	215.8	192.3	5.8	-10.91
2	206.7	193.0	3.9	-6.625
3	185.3	180.1	7.5	-2.823
4	179.0	161.1	6.3	-10.02

Table A.17
Comparison between TomoTherapy® TPS data and measured dose using four MO*Skin*™ detectors with the solid probe at $\theta = 90°$ for the $1.37 \times 1.37 \times 1.00$ mm^3 dose grid. Fiducial markers were attached to the probe.

Detector	Planned D/F (cGy)	Measured D/F (cGy)	Measured D/F Uncertainty (cGy)	% Difference
1	181.0	165.0	2.8	-8.847
2	166.5	158.6	3.7	-4.775
3	139.0	136.6	2.6	-1.741
4	139.3	121.5	1.6	-12.82

Table A.18
Comparison between TomoTherapy® TPS data and measured dose using four MO*Skin*™ detectors with the solid probe at $\theta = 180°$ for the $1.37 \times 1.37 \times 1.00$ mm^3 dose grid. Fiducial markers were attached to the probe.

Detector	Planned D/F (cGy)	Measured D/F (cGy)	Measured D/F Uncertainty (cGy)	% Difference
1	311.7	298.5	10.9	-4.222
2	306.5	306.0	5.1	-0.1602
3	286.5	294.5	2.3	2.777
4	257.8	271.4	7.1	5.268

Table A.19
Comparison between TomoTherapy® TPS data and measured dose using four dual MO*Skin*™ detectors with the solid probe at $\theta = 0°$ for the $1.37 \times 1.37 \times 1.00$ mm^3 dose grid.

Detector	Planned D/F (cGy)	Measured D/F (cGy)	Measured D/F Uncertainty (cGy)	% Difference
1	215.0	189.5	7.1	-11.88
2	196.0	196.8	9.2	0.4190
3	185.3	178.9	5.4	-3.462
4	174.5	162.3	3.2	-6.994

Table A.20
Comparison between TomoTherapy TPS data and measured dose using four dual MO*Skin*™ detectors with the solid probe at $\theta = 90°$ for the $1.37 \times 1.37 \times 1.00$ mm^3 dose grid.

Detector	Planned D/F (cGy)	Measured D/F (cGy)	Measured D/F Uncertainty (cGy)	% Difference
1	181.0	165.2	12.9	-8.729
2	168.0	165.7	1.5	-1.345
3	136.3	137.6	2.3	-0.9038
4	139.7	128.2	2.0	-8.180

Table A.21
Comparison between TomoTherapy TPS data and measured dose using four dual MO*Skin*™ detectors with the solid probe at $\theta = 180^{\circ}$ for the $1.37 \times 1.37 \times 1.00$ mm^3 dose grid.